ANALYSIS AND IMPLEMENTATION OF LONG PERIOD FIBER GRATING AND FRESNEL REFLECTION-BASED SENSORS FOR REFRACTIVE INDEX MEASUREMENT OF LIQUIDS

A Thesis Submitted to
the Graduate School of Engineering and Sciences of
İzmir Institute of Technology
in Partial Fulfillment of the Requirements for the Degree of

MASTER OF SCIENCE

in Electronics and Communication Engineering

by
Cansu İDE

June 2017
İZMİR

We approve the thesis of **Cansu İDE**

Examining Committee Members:

Assist. Prof. Dr. Kıvılcım YÜKSEL ALDOĞAN
Department of Electrical and Electronics Engineering, Izmir Institute of Technology

Assoc. Prof. Dr. Serkan ATEŞ
Department of Physics, Izmir Institute of Technology

Assist. Prof. Dr. Osman AKIN
Department of Mechatronics Engineering, İzmir Katip Çelebi University

30 June 2017

Assist. Prof. Dr. Kıvılcım YÜKSEL ALDOĞAN
Supervisor, Department of Electrical and Electronics Engineering
Izmir Institute of Technology

Assoc. Prof. Dr. Enver TATLICIOĞLU
Head of the Department of
Electrical and Electronics Engineering

Prof. Dr. Aysun SOFUOĞLU
Dean of the Graduate School of
Engineering and Sciences

ACKNOWLEDGEMENTS

I would like to thank my supervisor, Asisst. Prof. Dr. Kıvılcım Yüksel Aldoğan, for her support and guidance.

I would like to thank committee members for their contribution.

I am thankful to Çağın Ekici and Murat Toprak for their help in simulation work of my thesis, and Anıl Yılmaz, who helped me in the experiments.

I am also grateful to Oğuz Uncu and Burcu Okuklu for helping us in using the laboratories facilities of Food Engineering Department, Iztech.

I would like to thank ERMAKSAN Opto-Electronic R&D Department for offering the opportunity to benefit from all the cleanrooms and laboratories facilities of our company during my studies. I would like to thank my previous and present working groups (Fabrication, and Fiber Optic Sensor groups) for providing to me a pleasant working environment.

I would also express my thanks to the Electromagnetism & Telecom Department of the University of Mons for LPFGs used in the experimental works.

I would like to thank my parents Fehime and Mustafa İde and my sister Aslı İde Barsbay for their love and support they have given me my whole life.

Lastly, my heartfelt thanks goes to Birkan Çetin, who always supported and motivated me and managed to make me smile even in difficult times.

ABSTRACT

ANALYSIS AND IMPLEMENTATION OF LONG PERIOD FIBER GRATING AND FRESNEL REFLECTION-BASED SENSORS FOR REFRACTIVE INDEX MEASUREMENT OF LIQUIDS

Refractive index (RI) is one of the physical properties of material, such as boiling/ melting point, density, and elasticity. As one of the distinctive features of the material, measurement of the RI is nowadays used in many areas including the food, oil and petroleum industry, biomedical applications, and environmental analysis. In recent years, fiber optic based refractometers become highly popular thanks to the advantages they provide compared to other methods used in the above-mentioned fields.

In this context, two intrinsic fiber optic refractive index sensors were investigated in this thesis: long-period fiber grating (LPFG) based- and Fresnel reflection based- refractometers. The former examines the changes in the resonant wavelength interrogated by an Optical Spectrum Analyzer (OSA) whereas the latter uses SMF tip as sensing point interrogated by an Optical Time-Domain Reflectometer (OTDR) from a distant location.

In the framework of the thesis, we first of all, provided a detailed field-specific literature survey giving an overview of the fiber optic-based refractive index sensors. Then, the operation principles of LPFG were studied including the modelling aspects of this sensing element. For this purpose, transmission spectra of LPFGs to external refractive index changes have been simulated employing the two-layer fiber geometry. Next, the principles of Fresnel reflection-based sensor were investigated.

Finally, experimental work was realized on different concentrations of glucose-water, glycerol-water solutions, and various chemicals. Our experimental results show an excellent agreement with the theory which demonstrated the capability of measuring RI of liquids for both methods investigated in the scope of thesis.

ÖZET

SIVILARDA KIRILMA İNDİSİ ÖLÇÜMÜ AMACIYLA UZUN PERİYOTLU FİBER IZGARA VE FRESNEL YANSIMA-TABANLI SENSÖRLERİN ANALİZ VE UYGULAMASI

Kırılma indisi maddenin kaynama noktası, erime noktası, yoğunluk ve esneklik gibi fiziksel özelliklerinden biridir. Malzemenin ayırt edici bir özelliği olan kırılma indisinin ölçümü gıda, yağ ve petrol endüstrisi, biyomedikal uygulamalar ve çevresel analizler de dahil olmak üzere günümüzde birçok alanda kullanılmaktadır. Son yıllarda, fiber optik tabanlı refraktometreler, yukarıda sözü edilen alanlarda kullanılan diğer yöntemlere kıyasla sağladıkları avantajlar sayesinde oldukça yaygın hale gelmiştir.

Bu bağlamda, tezde uzun periyotlu fiber ızgara (LPFG)- ve Fresnel yansıma-tabanlı refraktometreler olmak üzere iki içsel fiber optik kırılma indisi sensörü incelenmiştir. Birinci yöntem bir Optik Spektrum Analizörü (OSA) tarafından sorgulanan rezonans dalga boyundaki değişiklikleri incelerken, ikinci yöntem uzak bir konumdan bir Optik Zaman-Bölgesi Reflektometresi (OTDR) tarafından sorgulanan tek modlu bir fiber (SMF) ucunu algılama noktası olarak kullanmaktadır.

Tez çerçevesinde, öncelikle, fiber optik tabanlı kırılma indisi sensörlerine genel bir bakış sağlayan ayrıntılı, alana özgü bir literatür araştırması yapılmıştır. Daha sonra, LPFG'nin çalışma prensipleri, bu algılama elemanının modelleme yönleri de dahil olmak üzere sunulmuştur. Bu amaçla, LPFG'lerin iletim tayflarının harici kırılma indisi değişikliklerine olan cevabı iki katmanlı fiber geometrisi kullanılarak simüle edilmiştir. Daha sonra Fresnel yansıma-tabanlı kırılma indisi sensörünün prensipleri çalışılmıştır.

Son olarak, farklı konsantrasyonlarda glikoz-su, gliserin-su çözeltileri ve çeşitli kimyasallarla kırılma indisi ölçümleri gerçekleştirilmiştir. Teori ile mükemmel bir uyum gösteren deneysel sonuçlar bu tez kapsamında araştırılan sensörlerin sıvıların kırılma indisini ölçme yeteneğini başarıyla ortaya koymuştur.

TABLE OF CONTENTS

LIST OF FIGURES

Figure **Page**

LIST OF TABLES

Table **Page**

LIST OF ABBREVIATIONS

LPG/LPFG……..Long period grating/long period fiber grating
FBG……..Fiber Bragg grating
πFBG……..pi-phase-shifted fiber Bragg grating
RI……...Refractive index
SRI…….Surrounding refractive index
PCF……Photonic crystal fiber
SPR……..Surface Plasmon resonance
PPR……..Particle Plasmon resonance
Hi-Bi……...……..High Birefringence
DI……...De-ionized
ATR……...Attenuated total reflection
F-P……Fabry-Perot
Q……Quality factor
MM……...Multi-mode
SM……...Single-mode
SMF……Single-mode fiber
MMF……Multi-mode fiber
MMSI……..Multi-mode step index
DSP……Double-side polished
FLM…….Fiber loop mirror
PMF…….Polarization maintaining fiber
PBGF…….Photonic band-gap fiber
CFBG……..Chirped fiber Bragg grating
TFBG…….....Tilted fiber Bragg grating
MMI……..Multi-mode interference
DCF…….....Dispersion compensation fiber
MZI……..Mach–Zehnder interferometer
NCF……... No-core fiber
ULPG……..Ultra-long-period grating
SMS…….....Single mode-multi mode-single mode
MSM…….Multi mode-single mode-multi mode

NATOF……... Non-adiabatic tapered optical fiber

POF……...Plastic optical fiber

MOF…….Micro-structured optical fiber

FFPI……Fiber Fabry–Perot interferometer

PDL……..Polarization dependent loss

IGS…….Inter-grating space

Mn…….Manganese

CMT……..Coupled-mode theory

HF acid……Hydrofluoric acid

NH4F……..Ammonium fluoride

CHAPTER 1

INTRODUCTION

1.1. Optical Fiber Sensors

Optical fiber sensors have significant advantages over conventional sensor types due to their physical and optical properties. Advantages of fiber optic sensors include their low cost, light weight, immunity to electromagnetic fields, ease of embedding in compact materials, high sensitivity and high bandwidth. Thanks to these advantages, fiber optic sensors have begun to be used in many different areas and the interest shown in fiber optic sensors has been continuously increasing in recent years.

1.2. Classification of Optical Fiber Sensors

Fiber optic sensors can be classified into three categories depending on the sensing location (intrinsic or extrinsic), modulation technique (intensity, wavelength, phase, or polarization) and application type (physical, chemical, biological or bio-chemical sensors). In our work, we focused on two different intrinsic fiber optic sensors. The measured parameter was refractive index. The sensing principle of one of these sensors was based on wavelength modulation (sensing element was long period fiber grating, LPFG), while the other's sensing principle technique was intensity modulation (sensing tip was standard SMF end, calculated parameter was Fresnel-reflection coefficient).

1.2.1. Classification According to Sensing Location

Depending on the sensing location, the fiber sensors are divided into two categories: intrinsic and extrinsic. In an intrinsic fiber sensor, light does not leave the fiber in order to be affected from the physical effects (cf. Figure 1.1 (a)). The optical fiber itself converts the environmental changes into light signal modulation. This modulation of light signal may be in form of intensity, phase, frequency or polarization (Udd, 2011).

Unlike internal sensing, in extrinsic fiber optic sensor, the light leaves the fiber and is blocked to make a measurement or is reflected back into the system. The parameter to be measured influences the light in the external medium. The effected light is carried to the detector by a receiving fiber (cf. Figure 1.1 (b)).

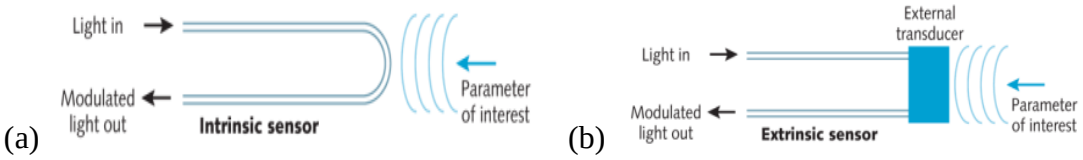

Figure 1.1 (a) Intrinsic and, (b) Extrinsic fiber optic sensor (Source: Mendez, 2011).

1.2.2. Classification Based on Application Type

Optical fiber sensors are used in many different applications to measure different parameters. Physical properties that can be measured by fiber optic sensors are temperature, stress, strain, displacement, pressure, velocity, and acceleration. Chemical sensors are used for pH and refractive index measurement, concentration determination, gas analysis, spectroscopic studies etc. Biological and bio-medical fiber optic sensors are used for measurement of blood flow, blood sugar concentration, glucose content, and detection of bacteria and proteins and so on. Biometric sensors are used to get fingerprint image.

1.2.3. Classification of FOS based on Modulation Techniques

1.2.3.1. Intensity Modulation

Intensity modulated fiber optic sensors can be configured in two main ways: transmission type (shown in Figure 1.2 (a)) and reflection type (shown in Figure 1.2 (b)).

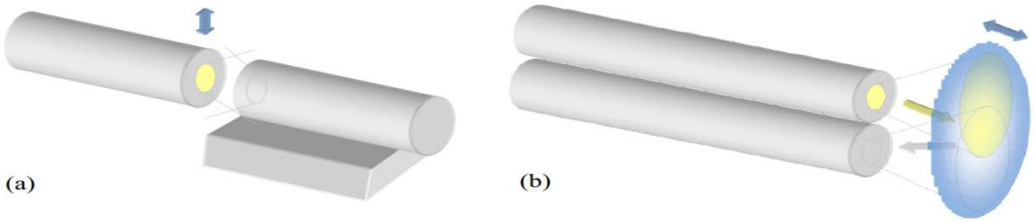

Figure 1.2. Schematic views of intensity modulated fiber optic sensors (a) using straight-forward transmission from one fiber to the other, (b) using a reflective configuration (Source: Jason, 2008).

Transmission type intensity modulated fiber optic sensors generally include a moveable fiber and a fixed fiber. Optical power is transmitted from the moveable fiber and received by the other. A change in position of the moveable fiber will cause a change in the received power. This type can be used as a strain sensor or a distance sensor.

Reflection type intensity-modulated fiber optic sensors include a reflective surface in front of the receiving and transmitting fiber. An axial displacement, vibration; or variation in the reflection characteristic of the external material (due to for example the refractive index change) cause a change in the received power. In some applications, this sensor type may involve only one fiber instead of transmitter and receiver fiber pairs, and transmitting fiber is used also to collect the reflected light (Toshima et. al., 1999). Reflection type intensity modulated fiber optic sensors can be used as distance, pressure or vibration sensors (Brenci et. al. 1988; Conforti et. al. 1989).

1.2.3.2. Phase Modulation

In these type of sensors, when a light beam is passed through interferometer, the light splits into two beams, one being exposed to sensing environment when the other beam is isolated from the sensing environment and used as a reference. External effects modulate the optical phase of the light transmitted through the fiber. This phase change is detected using optical fiber interferometric techniques that convert phase modulation into intensity modulation. Fabry-Perot, Mach-Zender, Michelson and Sagnac are most commonly used interferometers.

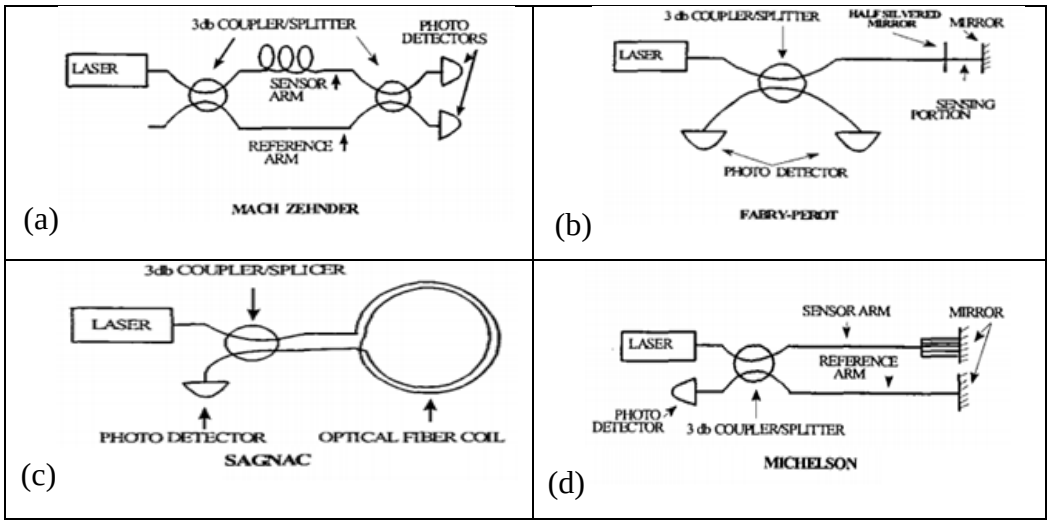

Figure 1.3. Optical fiber interferometric sensors (a) Mach-Zender, (b) Fabry-Perot, (c) Sagnac, (d) Michelson (Source: Mechery, 2000).

1.2.3.3. Polarization Modulation

The working principle of the polarization modulation sensors is based on the polarization change caused by the environmental effects of the light propagated in the optical fiber. Polarimetric sensors are more complex and expensive than intensity, phase and wavelength modulated sensors.

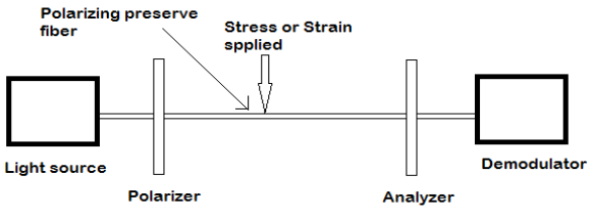

Figure 1.4. Schematic representation of a polarization modulated fibre optic sensor (Source: Ghetia et. al., 2013).

1.2.3.4. Wavelength Modulation

These sensors measure the changes in the relevant parameter depending on the difference in the wavelength. The change in the wavelength relative to the reference (initial) wavelength can be determined by an interrogating unit. Fiber gratings can be given as examples of wavelength-modulated sensors. These sensors can be used to mon-

itor temperature, refractive index, acceleration, humidity, tension or pressure. The details of the fiber gratings are given in the following paragraphs.

1.3. Fiber Gratings

Fiber gratings are simple, intrinsic sensing elements. They are fabricated by creating a region of periodically varying refractive index in the core, the cladding or both along the optical fiber (Vengsarkar et. al., 1996). They have all the advantages attributed to optical fiber sensors. The development of a permanent grating within the fiber core was first made by Hill et al. in 1978 (Canadian Communication Research Center in Ottawa, Canada) (Kawasaki and Hill, 1978; Meltz and Morey, 1989). Since that time, different methods and techniques have been developed to form a periodic change in the refractive index of the core. Phase mask (Hill et. al., 1993), interferometric (Morey et. al., 1994), and point-by-point methods (Malo et al., 1993) are among the most commonly used techniques.

1.4. Classification of Fiber Gratings

The structure of the fiber gratings varies depending on the refractive index change and the length of the grating period. There are different types of fiber gratings and in general, fiber gratings can be divided into two main categories: uniform and non-uniform.

1.4.1. Uniform Gratings

In the fibers with uniform gratings, the modulation depth of the refractive index is constant and the periodicity of the grating is uniform along the axis of the fiber. Depending on the length of the grating spaces and the direction of the change of the refractive index, there are usually three types of uniform gratings: fiber Bragg gratings (FBGs), long-period fiber gratings (LPFGs), and tilted fiber Bragg gratings (TFBGs).

1.4.1.1. Fiber Bragg Gratings (FBG)

The periodicity of the FBG is usually on the order of 100 nm (cf. Figure 1.5 (a)), and the modulation depth of the refractive index is in the range about 10^{-5} and 10^{-3}. FBGs are also called short-period gratings or reflection gratings. Forward-propagation light in the fiber core (fundamental core mode) couples to the backward-propagation core mode at a specific wavelength. This wavelength is called as *Bragg wavelength* and this coupling called as contra-directional coupling. In addition to use as an optical fiber sensor element, FBGs could also be used in optical communications, such as highly wavelength-selective reflection filters, etc.

1.4.1.2. Long Period Fiber Gratings (LPFG, or LPG)

A typical LPFG (or abbreviated as LPG) has a grating period of about hundreds of micrometers, a length of about 1 - 3 cm, and index modulation depth of 10^{-4} or greater (Kersey et. al., 1997). A LPFG with periodical variation of the refractive index, along the direction of fiber core axis is shown in Figure 1.5.(b). LPFG couples light from the fundamental core mode to the other forward-propagation cladding modes at specific wavelengths. These wavelengths are called *resonant wavelengths*. There are multiple cladding modes provided by the fiber (waveguide). Therefore, transmission spectrum of the LPFG consists of a series of discrete attenuation bands near these resonant wavelengths. Detailed working principles of LPFGs are discussed in the next chapter. Due to their low-level back reflection, LPGs are transmission-type devices, not the reflection-type devices as FBGs. LPFGs can be used as sensors. Any variation in external effects (temperature, axial strain and external refractive index, etc.) may cause a wavelength shift in the transmission spectrum compared to the initial spectrum (Brenci et. al., 1988).

1.4.1.3. Tilted Fiber Bragg Gratings (TFBG)

TFBGs have similar period length as the FBGs. As seen in Figure 1.5.(c), the main difference of the TFBGs compared to LPGs and FBGs is that the variation of the refractive index is at an angle to the optical axis of the fiber core.

1.4.2. Non-uniform Gratings

For the fibers with non-uniform gratings; the periodicity of the grating is non-uniform along the axis of the fiber core and the modulation depth of the refractive index does not need to be constant. There are many kinds of non-uniform gratings, such as chirped fiber Bragg gratings, superimposed multiple fiber Bragg gratings, and super-structure fiber Bragg gratings.

1.4.2.1. Chirped Fiber Bragg Gratings (CFBG)

A chirped-fiber grating structure can be formed by varying the grating period, the average refractive index, or both along the length of the grating (cf. Figure 1.5 (d)). The chirped fiber Bragg gratings could be used to measure strain or temperature (Xu M. et. al., 1995; Won et. al., 2004).

1.4.2.2. Superstructure Fiber Bragg Gratings (SFBG)

A superstructure fiber Bragg grating specifies a special FBG consisting of several small FBGs placed very close to each other (see Figure 1.5 (e)). These fiber gratings are also called sampled fiber Bragg grating. Superstructure fiber Bragg grating could be written with a modulated exposure over the length of the gratings (Eggleton et. al., 1994). They can be used as comb filters for signal processing (Zhou D., 2010).

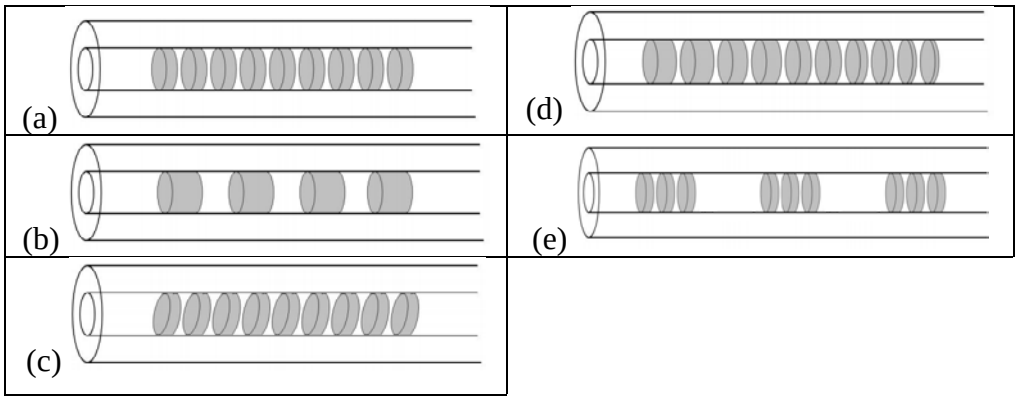

Figure 1.5. Fiber grating types, (a) Fiber Bragg grating (FBG), (b) Long period fiber grating (LPFG), (c) Tilted fiber Bragg grating, (d) Chirped fiber Bragg grating, (e) Superstructure fiber Bragg grating (Source: Zhou D., 2010).

1.4.2.3. Superimposed Multiple Fiber Bragg Gratings

Superimposed multiple fiber Bragg gratings are in the form of several Bragg gratings written at the same location on an optical fiber core (Othonos et. al. 1994). These kinds of gratings are generally used in fiber communications, lasers and sensor systems for multiplexing purposes.

1.5. Refractive Index Measurement

The refractive index of a material is one of the important optical parameters. Propagation of light in a medium experiences a delay compared to the propagation of light in free space (for all practical purposes, air or vacuum). The refractive index is a measure of the ratio of the speed of light in vacuum to that in the medium (such as water, glass, etc.), for a given frequency. It is generally symbolized by the letter n. Refractive index is considered as one of the physical properties of material such as boiling point, melting point and density. It varies from material to material, hence there is a specific refractive index for each material.

The refractive index measurement is frequently used in a variety of fields, such as the chemical industry, food quality and safety analysis, bio-medical applications, environmental imaging systems, petroleum and oil industry and material analysis. Since the refractive index is a critical parameter in many different areas, there is an increasing

interest in recent years in determining the exact value of the refractive index of the materials (Li and Xie, 1996; Liang et. al. 2007).

The refractive indices of the mixtures depend on the amount of the concentrations of the substances forming the mixture. If the percentage of the amount of the substance dissolved in a solution is unknown, it is possible to determine it by finding the value of the refractive index of the solution. For example, determination of the amounts of salt (salinity) or sugar concentration (brix) in different solutions. In addition to determining the concentration (Chen C.-H. et. al, 2013; Roy et. al., 1999; Cherif et. al., 2002; Takeishi et. al., 2008; Garg et. al., 2013), other physical parameters such as density, acidity (Nath, 2010), or pH (Tai et. al., 2010) can also be detected by measuring RI.

By measuring the refractive index of liquid mixtures adulteration could also be found. In recent years, different analytical techniques have been used to detect adulteration. Among them are chromatographic methods (Aparicio et. al. 2000), differential scanning calorimetry, nuclear magnetic resonance spectrometry (Vlahov et. al., 1999), Fourier transform Raman spectroscopy (Davies et. al., 2000; Baeten et. al. 1996 and 2001; Yang and Irudayaraj, 2001) and photopyroelectric detection etc. These conventional techniques have some disadvantages. They are expensive, time consuming, laboratory-based (only possible for samples in laboratory), require analytical skills, and generate hazardous chemical waste. Legal requirements for quality standards in different areas, and increased public awareness have created a need for more reliable, faster, automated, remote and / or portable, multi-measurement-capability refractive index sensors and monitoring systems.

Fiber-based RI sensors provides attractive solutions in this area. Their remote measurement capability, fast response time, small size, geometric flexibility, immunity to electromagnetic interference and electronically passive nature make the fibers available as real-time RI sensors for hazardous conditions such as gas or petrol lines, or for production line at many industrial sector (e.g. pharmaceutical or agriculture factories). Fiber-based RI sensors can have high sensitivity and high resolution, so even small RI index changes of fluids or volatile gases in small volumes can be measured (while 10^{-5} refractive index changes can be detected with conventional methods, fiber based refraction index sensors can be detected 10^{-8} (Caucheteur et al., 2016). Fiber-based RI sensors also allow instantaneous determination of the percentage concentration of adulteration in different samples (i.e. fuels, edible oils) without involving any chemical analysis (Mishra et. al. 2008; Libish et al., 2010 and 2011).

Conventional refractometers (e.g. Abbe) have calibration fluid whose temperature and the temperature of the liquid to be measured should be the same (20°C). If there is a large temperature difference between them, refractive index should be measured after waiting 30 minutes. Unlike conventional refractometers, fiber optic-based refractive index sensors; allow to take measurements without an extra calibration fluid. Temperature and the refractive index can be measured at the same time too, by using hybrid fiber optic RI sensors.

Various fiber-based refractive index sensors have been developed by different research groups. These developed sensors' modulation techniques are intensity, wavelength, phase or polarization. The complete state-of-the-art of these fiber optic RI sensors is given in the following section.

1.6. Overview of Fiber-Based Refractive Index Sensors

For measuring the RI in several liquids, the first optical fiber refractometer is proposed by Cooper, in 1983. This configuration is not an all-fiber refractometer. It combines two technologies (bulk and fiber) and it is very complex. The first all-fiber refractometer is described by Kumar et al., in 1984.

During the last thirty years, several researchers and research groups have published different types of fiber-based refractive index sensors. These sensors include fiber Bragg grating (FBG) structures; long period gratings (LPGs) in a simple fiber structure (Mishra et. al. 2008; Libish et. al., 2010 and 2011; Rego et al., 2006; Singh et. al. 2012; Liu and Qu., 2013; Akki et. al., 2013), or tapered fiber structures (Allsop et. al., 2006; Linesh et. al., 2011; Chen X. et. al., 2004; Tien et. al., 2009), combining the LPFG in series with another LPFG to form a Mach-Zehnder interferometer (Allsop et. al., 2002) or with a fiber that have a mirror coated-end to form a Michelson interferometer (Caldas et. al. 2008; Swart, 2004); photonic crystal fibers (PCF) (Coelho et. al., 2012; Silva et. al., 2011); MSM (multi mode-single mode-multi mode) fiber structures (Villatoro et. al. 2006) or SMS (single mode-multi mode-single mode) fiber structures (Wu et al., 2011; Wang P. et. al., 2011; Xue and Yang, 2012); fiber tapers (Tian Z. et. al., 2008; Wang P. et. al., 2013; Tai et. al, 2010; Zibaii et al., 2011; Monzón-Hernández et. al., 2005); micro-interferometers (Liu et. al., 2012; Coelho et. al., 2011; Silva et. al., 2012; Sun H. et. al., 2012) such as Fabry-Perot fiber sensors (Sun H. et. al., 2013; Wang

T. and M. 2012; Silva et. al., 2008; Gouveia et. al., 2012; Frazão et. al., 2009 (2)), and sensors using surface plasmon resonance (SPR) effects (Caucheteur et. al., 2011; Díaz-Herrera et. al., (2010) and 2010 (2)).

Typically, the SPR fiber sensors use D-fibers, tapered optical fibers (by Diaz-Herrera et al., 2010) or polished fibers (Alvarez-Herrero et. al., 2004; Kim K. et. al., 2007). To induce the surface plasmon mode a thin metal film (i.e. silver, gold, palladium, etc.) should be coated over the fiber surface. Addition to these types, new combined configurations are presented:

- SPR-based FBG presented by Diaz-Herrera et al. in 2010 (2),
- SPR-based TFBG presented by Caucheteur et al. in 2011,
- SPR-based LPFG presented by Schuster et. al., 2012 and Gu et. al. 2015.

The typical resolution of the fiber SPR sensor is about $10^{-3} - 10^{-5}$ refractive index units (RIUs).

Fabry-Pérot interferometers (FPI) have also been widely used as RI sensors. The extrinsic fiber Fabry-Perot interferometric sensors (EFPIs) have many advantages, but it is difficult to multiplex multiple sensors and this leads to a high average cost of single sensor.

For using the FBGs as refractive index sensor, removal of the fiber cladding is required to increase the evanescent field interaction with the surrounding environment. Specialty fibers such as D-shaped (Chen H.-W. et. al., 2007) or H-shaped fibers (Frazão et. al., 2009) should be used or the fiber should be thinned to a diameter of 20 microns or less (cf. Table 5.3. at Chapter-5: “Perspectives and Future Work”). All these methods reduce the mechanical strength and durability of the fiber and increase fabrication complexity and raise the costs. In addition, they suffer from high cross-sensitivity to temperature.

Compared to etched FBG sensors, the LPG fiber based RI sensors, are compact, and do not require the use of specialty fibers, side polishing fibers and/or post processing. They can be used directly to measure the change in the refractive index of the surrounding medium due to the cladding modes based coupling mechanism (Mishra et. al. 2008; Libish et. al., 2010 and 2011; Rego et al., 2006; Singh et. al. 2012; Liu and Qu., 2013; Akki et. al., 2013). However, LPGs are working in transmission mode, therefore the multiplexing of it is not easy. In addition, the relatively long length of the grating limits their application as point sensor devices. The sensitivity of the LPG fiber

based RI sensors, is relatively smaller (~ 700 nm/RIU) as compared to the SPR based sensors (for biosensors the refractive index sensitivity should be typically at the order of 1000 nm/RIU (Garg et. al., 2013). To increase the sensitivity, several techniques have been developed: writing the LPG in etched or tapered fibers, choosing the cladding refractive index of the fiber closer to the refractive index of the surrounding medium, or tuning the resonant wavelength anywhere in the electromagnetic spectrum such as in the highly sensitive region, or thin film coating. All these sensitivity enhancement methods are discussed in Chapter-5.

The first long period grating was described in 1996 by Vengsarkar et al. for band-rejection filters, and in the same year the first refractometric sensor based on long period fiber grating was presented by Bhatia and Vengsarkar (1996), reporting an average resolution of 7.69×10^{-5} RIU in the 1.404 – 1.452 refractive index range.

Similar to LPGs, tilted fiber Bragg gratings (TFBGs) do not require the use of specialty fibers and post processing, as a TFBG can couple the core mode to the back-propagating core mode and back propagating cladding modes whose effective refractive indices are sensitive to surrounding RI (Zhang X. et. al., 2013; Zhou K. et. al. 2006; Huy et. al.2006). Contrary to long period fiber grating based refractometers, they provide temperature-insensitive SRI measurements (Laffont and Ferdinand, 2001; Caucheteur and Mégret, 2005; Guo et. al, 2008), and are much less sensitive to bending effects (Baek et. al., 2002), which make them easy to use in practical applications.

In addition to above-mentioned sensors, *hybrid interferometric* structures (Sun H. et. al., 2013) and *hybrid grating* structures have also been investigated for RI measurement. In 2009, Jesus et al. presented a hybrid configuration to measure RI and temperature using a LPG along with two FBGs. In 2012, Enriquez et al. repeated this configuration with only one FBG. In this sensor, only a small part of the cladding modes could be recoupled due to the narrow bandwidth of FBG, that limits the sensitivity. In general, the requirement for a highly accurate spectrum analyzer limits the applications of hybrid gratings for RI measurement.

CFBGs (chirped fiber Bragg gratings) are presented as RI sensors, too. However, they are core mode based grating sensors like FBGs. Therefore, they are intrinsically immune to outer RI changes. Sun A. et al. proposed in 2012, a simple but highly sensitive scheme employing a hybrid LPG/CFBG for cost-effective RI measurement. Strong reflected cladding modes with a wide wavelength range can be excited and recoupled

into the fiber core with a high efficiency, through the hybrid LPG/CFBG. The resolution of this sensor was reported as $5.6x10^{-6}$.

1.6.1. Comparison of Fiber Optic Based Refractive Index Sensors

This section is devoted to a global analysis about advantages and disadvantages of fiber optic based refractometers compared to each other, which in turn explains the reasons for focusing on long period grating based (wavelength modulated) and Fresnel-reflection based (intensity modulated) fiber optic sensors in this thesis.

Interferometric sensors are limited by some drawbacks. They have high sensitivity but require costly demodulation schemes such as fringe counters. Additionally, at some points of the transfer function curve, these sensors can suffer from directional uncertainty.

Surface Plasmon sensors are attractive refractive index sensors. Although they are highly sensitive to the small changes in the ambient index of refraction, they suffer from polarization sensitivity. For the interaction of the induced Plasmon with the evanescent field of the propagating mode, such sensors require that the cladding of the fiber be polished and place the plasmonic materials on the fiber, making it difficult to fabricate (Klantsataya, et. al., 2017).

Long period fiber gratings can be used directly to measure the change in the refractive index of the external medium. And they may be as sensitive as SPR based refractive index sensors with some sensitivity enhancement methods (for details cf. Chapter-5: “Perspectives and Future Work”). Besides the advantages provided by LPFG-based sensors, there are also a few disadvantages that limit their use. For instance, highly stable fabrication techniques are required for them; especially for sensor applications with increased sensitivity.

Other studied sensor was intensity based. These kinds of sensors have limited sensitivities. They suffer from the requirement of calibration that might be a function of the optical source characteristics and physical deformation along the fiber length, but they are straightforward and low-cost.

The sensors used in this thesis are of intrinsic type, i.e. the sensing region of the fiber is in intimate contact with the liquid medium. However, intrinsic type FO refractometers have two major limitations. First, to measure different liquids’ refractive indi-

ces, the sensing region must be cleaned properly which makes the measurement process time consuming. Secondly, intrinsic type fiber optic sensors cannot be used to measure the refractive index of reactive chemical solutions such as hydrofluoric acid (HF), nitric acid (HNO3) etc. In order to overcome this limitation, Rahman et al. (2011) and Nath (2010) proposed extrinsic type, fiber-based RI index sensor which was based on intensity modulation of the back-reflected light signal due to the change in the refractive index of the liquids. This approach may be useful for measuring refractive indices of active chemical solutions, however compared to intrinsic type fiber-based RI sensors, their resolutions are small ($\sim 10^{-3}$).

Table 1.1 compares the performance of two modulation techniques used in this study. They are listed with emphasis on major advantages and limitations.

Table 1.1. Performance summary of the RI sensing techniques used.

	Intensity-Modulated RI Sensor	**Wavelength-Modulated RI Sensor**
Advantages	• Straightforward and practical measurement system • Requires only intensity spectrum for measurements • No need for complex fabrication techniques • Low fabrication cost, easy to handle • Long life (for extrinsic sensors) • Simple and low-cost multiplexing capabilities • Thanks to multiplexing capability, ease of use as distributed multi-point sensor	• High sensitivity and resolution, (suitable for biochemical analysis, food and chemical industries, etc.) • High dynamic range • Multiplexing capability • Conformity to sensitivity enhancement methods
Limitations	• Comparatively low resolution (Resolution can be improved by using suitable techniques, e.g. tapered fiber RI sensors, but this will reduce the mechanical stability of the fiber and increase the sensitivity to different kinds of environmental changes, such as temperature, humidity, and mechanical stress. This can negatively affect the measurement accuracy of the sensor.) • Easily affected by the power fluctuation from the light source or from the external environments • Possibility of two different RI values giving the same intensity	• High cost fabrication[1] and demodulation techniques • Etching or thinning methods weakens the fiber strength; therefore, they can break easily. FBG or LPG with a thin cladding requires special protective packaging • Complex fabrication methods and theoretical modelling • Comparatively short life (FBG or LPG act as a sensing element, (intrinsic sensing)) • Relatively long length of the gratings limits their applications as point sensors (for LPGs)

[1] In recent years, 3D printers have been proposed as low-cost writing techniques for fiber gratings. This method eliminates the need for an expensive phase mask for each different fiber grating structure in the phase mask method, and the need for expensive components in other techniques (Iezzi et. al., 2016).

Table 1.2. Various fiber optic based refractive index sensors.

Configuration	Modulation Method	Refractive Index Range	Sensitivity	Resolution RI Unit	RI Related Parameter	Ref.
TFBG in thin-core fiber	Spectral shift	1.338 - 1.433	3.6 nm/RIU	-	-	(Peng et. al., 2013)
Hybrid interferometer Fabry-Perot/Michelson	FFT analysis	1.33 - 1.38	-102048.3 /RIU	$8.7x10^{-4}$	Glycerin concentration in water	(Sun H. et. al., 2013)
Taper-based Michelson interferometer	Spectral shift	1.31 - 1.37	-	$5.1x10^{-4}$	Dimethyl sulfoxide concentration in water	(Tian et. al. 2008)
F-P (based on In-fiber ellipsoi-dal cavity (SMF&PCF)	FFT analysis	1.32 - 1.45	5.68/RIU	$1.2x10^{-5}$	Sugar concentration in water	(Wang T. and M. 2012)
F-P (based on graded index multimode fibers)	FFT analysis	1.330 - 1.448	-0.14036/ RIU	-	Saturated syrup con-centration in water	(Liu et.al., 2012)
ATR and PPR Window-type optical fiber	Intensity modulation	1.333 - 1.383	-	$1.8x10^{-4}$ & $5.73x10^{-5}$	Sucrose concentration in DI water	(Chen C.-H. et.al., 2013)
600 μm core diameter plastic-clad-silica (PCS) optical fiber	Intensity modulation	1.436 - 1.461	-	-	Concentration of kero-sene in petrol / diesel	(Roy, 1999)
Tetrathoxysilane coated (on uncladded part) fiber	Intensity modulation	1.41 - 1.45	32 mV/% (in volume)	10^{-3}	Toluene concentration in deionized water	(Cherif et. al., 2002)
Multi mode-single mode-multi mode fiber structure	Intensity modulation	1.430 - 1.460	-	$7x10^{-5}$	-	(Villatoro et. al., 2006)
Silica tube MMI	Spectral shift	1.341 - 1.394	112.1 nm/RIU	-	-	(Coelho et. al., 2011)
TiO_2 film coated side-polished optical fiber	Spectral shift	-	0.46 ± 0.03 nm/% RH	0.2% RH	Relative humidity	(Alvarez-H. et. al., 2004)
Side-polished fiber	Intensity modulation	-	-	-	Oil quality	(Gastón et. al., 2006)

(cont. on next page)

Table 1.2. (cont.)

Configuration	Modulation Method	Refractive Index Range	Sensitivity	Resolution RI Unit	RI Related Parameter	Ref.
Palladium Coated Side-Polished SMF	Intensity modulation	-	0.3 dB/% hydrogen in volume	4% hydrogen in gas mixture	Hydrogen Sensor	(Kim K. et. al., 2007)
FBG/ Fabry-Perot	Fringe Visibility	1.333 - 1.405	0.6 mV/RIU	10^{-3}	Ethylene glycol concentration in water	(Silva et. al., 2008)
Standard SMF	Intensity modulation	-	-	-	Alcohol concentration in gasoline	(Takeishi et. al., 2008)
Displacement sensor (two MMSI fibers and a mirror)	Intensity modulation	1 - 1.52	-	-	-	(Govindan et. al., 2009)
Fabry-Perot (FBG on Hi-Bi Fiber)	Fringe Visibility	1.335 - 1.375	1%/0.01 RIU	10^{-3}	Ethylene glycol concentration in water	(Gouveia et. al., 2012)
FBG in etched H-shaped fiber	Spectral shift	1.333 - 1.390	3.5 nm/RIU	$5x10^{-3}$	-	(Frazão et. al., 2009)
Extrinsic sensor based on beam through tech.	Intensity modulation	1.3284 - 1.3776	23.07 mV/RIU	$2.28x10^{-3}$	Sodium chloride (NaCl) concentration in DI water	(Rahman et. al., 2011)
FPI	Spectral shift	1.331 - 1.335	665.90 nm/RIU	$6x10^{-6}$	Sugar concentration	(Tian et. al., 2011)
Fiber loop mirror (FLM) combined with an etched PMF	Spectral shift	1.35 - 1.47	25.29 nm/RIU	$7.91x10^{-4}$	-	(Wang J. et. al., 2011)
Side-polished all-solid PBGF	Spectral shift	1.31 - 1.43	315 nm/RIU	10^{-5}	-	(Yong et. al., 2012)
Suspended core fiber F-P	FFT analysis	1.330 - 1.424	-11.27/RIU	$2x10^{-4}$	-	(Frazão et. al., 2009 (2))

(cont. on next page)

Table 1.2. (cont.)

Configuration	Modulation Method	Refractive Index Range	Sensitivity	Resolution RI Unit	RI Related Parameter	Ref.
Periodically tapered small core SMF	Spectral shift	1.33 - 1.38	226.6 nm/RIU	$4.41x10^{-5}$	-	(Wang P. et. al., 2011)
PANDA-type Hi-Bi fiber	Intensity modulation	1.33 - 1.41	-35.34dB/ RIU	$2.82x10^{-5}$	Glycerin concentration in water	(Rong et. al., 2013)
50 μm and 150 μm MMI fiber tip	Intensity modulation	1.30 - 1.39	-110 dB/RIU for both	$2.2x10^{-4}$ $3.8x10^{-4}$	-	(Silva et. al., 2012)
MZI-based MMF-DCF-MMF	Spectral shift	1.33 - 1.39	66.32 nm/RIU	-	-	(Sun H. et. al., 2012)
No-core fiber (NCF)-FBG Interferometer	Intensity modulation	1.333 - 1.378	160.23 dB/RIU	0.0014	-	(Li et. al., 2012)
Gold-coated weakly TFBG SPR sensor	PDL modulation	1.31 - 1.38	673 nm/RIU	-	-	(Caucheteur et. al., 2011)
SPR in tapered fiber	Spectral shift	1.332 - 1.338	5000 nm/RIU	-	Ethylene glycol con-centration in water	(Diaz-Herrera et. al., 2010)
Tapered optical fiber tip	Intensity modulation	1.33 - 1.43	8000%/ RIU	$2.5x10^{-5}$	pH values of acetic acid	(Tai et. al., 2010)
SPR-FBG	Intensity modulation	1.333 - 1.340	20%/0.01 RIU	$2x10^{-5}$	-	(Diaz-Herrera et. al., 2010(2))
Non-adiabatic tapered fiber in fiber loop mirror	Spectral shift	1.338 - 1.351	1233nm/ RIU	-	Concentrations of salt solution	(Zibaii et. al., 2011)
Dual FBGs interposed with a MMF taper	Intensity modulation	1.3333 - 1.4206	-91.31 dB/RIU	10^{-5}	-	(Shao et. al., 2007)
Cladded multimode tapered fiber tip with mirrored end	Intensity modulation	1.36 - 1.46	-	$3x10^{-5}$	-	(Monzón-Hernández et. al., 2005)

(cont. on next page)

Table 1.2. (cont.)

Configuration	Modulation Method	Refractive Index Range	Sensitivity	Resolution RI Unit	RI Related Parameter	Ref.
Submicron-thick tapered SMF	Intensity modulation	1.37 - 1.40	-	$\sim 5x10^{-4}$	Glycerol concentration in water	(Polynkin et. al., 2005)
Micro-structured FBG	Intensity modulation	1.364 - 1.420	-	$4x10^{-5}$ & $6x10^{-5}$	-	(Iadicicco et. al. 2005)
V-shaped RI sensor/air-gap sensor	Intensity modulation	1.35 - 1.46	-	$2.5x10^{-4}$	Concentration of sugar in water	(Trudeau et. al., 2006)
Plastic optical fiber	Intensity modulation	1.30 - 1.59	-	$\sim 10^{-3}$	-	(Zubia et. al., 2000)
Large-core air-clad PCF	Spectral shift	1.331 - 1.373	322 nm/RIU	$7.2x10^{-4}$	Ethylene glycol concentration in water	(Coelho et. al. 2012)
Large-core air-clad PCF	Spectral shift	1.3216 - 1.3246	800 nm/RIU (max.)	$3.4x10^{-5}$	-	(Silva et. al., 2011)
Polished SMF	Intensity modulation	1.46 - 1.48	-	10^{-4}	-	(Falco et. al., 1986)
POF with stripped cladding	Intensity modulation	1.440 - 1.446	-	$\sim 10^{-3}$	Detection of oil density	(Takeo et. al., 1982)
TFBG	Spectral shift	1.3 - 1.4	340nm/RIU	$3x10^{-4}$	-	(Zhou K. et. al., 2006)
FBG in a side-polished fiber	Spectral shift	1.33 - 1.45	300nm/RIU	$\sim 10^{-5}$ $\sim 10^{-6}$	Quality control of petrol products	(Schroeder et. al., 2001)
TFBG photowritten in MOF	Spectral shift	1.296 - 1.450	-	$\sim 10^{-5}$	-	(Huy, et. al., 2006)
Etch-eroded fiber Fabry-Pérot interferometer (FFPI)	Spectral shift	1.33324 - 1.33476	71.2nm/ RIU	$1.4x10^{-5}$	Isopropyl alcohol concentration in water	(Liang et. al., 2005)

(cont. on next page)

Table 1.2. (cont.)

Configuration	Modulation Method	Refractive Index Range	Sensitivity	Resolution RI Unit	RI Related Parameter	Ref.
TFBG	Spectral shift	1.25 - 1.44	39 nm/RIU	-	-	(Chan et. al., 2007)
Gold-coated highly TFBG SPR sensor	Spectral shift	1.00028 - 1.4234	204 nm/ RIU	$\sim 10^{-8}$		(Caucheteur et. al., 2016)
Non-intrusive step-index MMF	Intensity modulation	1.33 - 1.50	-	0.002	Propylene glycol concentration in water	(Nath, 2010)

Table 1.3. Various long-period grating fiber based refractive index sensors.

Configuration	Modulation Method	Refractive Index Range	Sensitivity	Resolution RI Unit	RI Related Parameter	Ref.
LPG	Spectral Shift	1.446 - 1.458	0.14 nm/ vol% of kerosene	$3.57x10^{-4}$	Adulteration detection of fuel	(Mishra et. al., 2010)
LPG with IGS	Spectral Shift	1.333 - 1.353	2500 nm/RIU	$\sim 4x10^{-7}$	Concentration of sucrose in distilled water	(Garg et. al., 2013)
Superimposed LPG	Spectral Shift	1.33 - 1.42	~500-1545 nm/RIU	$\sim 10^{-6}$- 10^{-7}	-	(Garg et. al., 2012)
LPG	Spectral Shift	1 - 1.458	-	-	-	(Singh et. al., 2012)
LPG	Amplitude Modulation	-	-	-	Concentration of Mn in distilled water	(Akki et. al., 2013)
ULPG	Spectral Shift	1.412 - 1.454	626 nm/RIU	-	-	(Liu and Qu, 2013)
π-Shifted LPG	Spectral shift & Amplitude modulation	1.333 - 1.4283	- 19 nm/RIU and 146 μW/RIU	$\sim 10^{-3}$	Salinity level of seawater	(Falate et. al., 2006)
LPG in solid-core PBGF	Spectral Shift	$\sim$ 1.50	17.900 nm/RIU	$8.4x10^{-6}$	Temperature dependence of the fluid	(Shi et. al., 2009)
LPG	Spectral Shift	1.450 - 1.459	0.50 nm/ vol% of palm oil	-	Adulteration detection of coconut oil	(Libish et. al., 2010)
LPG	Spectral shift Amplitude modulation	1.450 - 1.454 1.468 - 1.460	0.15 nm/ vol% of paraffin oil 0.06dB/vol% of paraffin oil	$2.66x10^{-4}$ RIU $2.9x10^{-3}$ dB^{-1}	Adulteration detection of coconut oil and sunflower	(Libish et. al., 2011)

(cont. on next page)

Table 1.3. (cont.)

Configuration	Modulation Method	Refractive Index Range	Sensitivity	Resolution RI Unit	RI Related Parameter	Ref.
Hybrid LPG/FBG	Amplitude Modulation	1.335 - 1.375	4%/0.001 RIU	$2x10^{-5}$	Concentration of ethylene glycol in water	(Jesus et. al., 2009)
LPG	Spectral shift	1.3211 - 1.3271	40 nm/RIU	$6x10^{-3}$	Concentration of ethylene glycol in distilled water	(Rego et. al., 2010)
Hybrid LPG/FBG	Wavelength & Amplitude Modulation	1.33 - 1.43	-	-	Concentration of ethylene glycol in water	(Enriquez et. al., 2012)
Periodically Tapered LPG	Spectral Shift	1 - 1.462	280pm/vol%	-	Concentration of ethanol in gasoline	(Linesh et. al., 2011)
LPG based Interferometer	Carrier phase Tracking	1.40 - 1.43	26,700 deg/RIU	$4.6x10^{-5}$	Concentration of ethylene glycol in water	(Caldas et. al., 2008)
Hybrid LPG/CFBG	Amplitude Modulation	1.00 - 1.43	177 μW/RIU	$5.6x10^{-6}$	-	(Sun A. et. al., 2012)
LPG	Spectral Shift	1.4436–1.4489	10,792.45 nm/RIU	-	-	(Li Q.-S. et. al., 2016)

1.7. Overview of the Thesis

The thesis is organized as follows: Chapters 2, 3, and 5 relate to the refractive index sensor based on long period fiber grating (LPFG). In Chapter 2, the theoretical and mathematical basis of mode coupling is described, and the simulation method of LPFG is given. The experimental work and the experimental results related to this sensor are presented in Chapter 3. Chapter 4 deals with the sensor based on the Fresnel-reflection measured by the way of OTDR, which has been studied as an alternative refractive index sensor. This section contains experimental results and a literature review of other Fresnel reflection-based sensors. Chapter 5 (“Perspectives and Future Work”) includes the literature survey of developed methods to increase the sensitivity of the LPFG based sensor. Experimental methods are done with the test fibers to determine the etch rate of silica fiber, for preferred sensitivity enhancement method. These results are also reported in this section. In addition to these chapters, the solutions of the Maxwell equations in the cylindrical coordinates are given in Appendix A, and the characteristic equation under the weakly guiding approximation for hybrid modes in LPFG is given in Appendix B.

CHAPTER 2

MODELLING OF LONG-PERIOD FIBRE GRATINGS

2.1. Introduction

Wave propagation in optical fibers is expressed by solving Maxwell's equations at appropriate boundary conditions (cf. Appendix A). The complexity of finding solutions to the wave propagation equations (characteristic equations) is simplified by using weakly guiding approximation. Therefore, modes can be defined in terms of the linearly polarized modes (cf. Appendix B). In the absence of any perturbation (e.g., bending), these different modes propagate without coupling.

If the waveguide has a periodic phase and / or amplitude perturbation, coupling of specific propagating modes occur (Erdogan, 1997). The most common used method for analyzing these kind of waveguides is the *mode coupling theory*. In this chapter, this theory will be explained. Other techniques are also available but the coupled mode theory is straightforward and can accurately model the optical properties of fiber gratings (Erdogan, 1997).

Fiber gratings, which have a periodic refractive index modulation in the fiber, induce wavelength dependent mode coupling. As mentioned Chapter 1 there are two main fiber gratings; fiber Bragg (or short-period, reflection-type) gratings and long period (or transmission-type) gratings. LPGs are our concern, in this thesis. In FBGs, coupling occurs between counter-propagation modes. Unlike FBGs, in LPGs coupling occurs between co-propagation modes (co-directional coupling) (cf. Figure 2.1). Energy transfer happens between core and cladding modes traveling in the +z direction. In single mode fibers, energy cannot be transferred to another mode within the core. Hence, energy can only be coupled to the cladding modes.

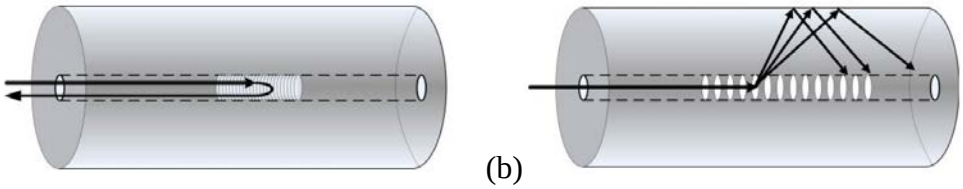

(a) (b)

Figure 2.1. Schematic representation of the light coupling in single mode fibers, (a) contra-directional coupling between forward propagating core mode to backward propagating mode in FBG, (b) co-directional coupling between fundamental core mode and forward propagating cladding modes in LPG (Source: Mou et. al., 2014).

Generally, the index perturbation can be described using the product of three functions (Hochreiner et. al., 2008);

$$\Delta n(r, \phi, z) = \sigma(z)\, S(z)\, P(r, \phi) \tag{2.1}$$

where $\sigma(z)$ represents the constant value of unity. S(z) represents the periodic refractive index changes that make up the grating. $P(r, \phi)$ denotes a function describing the radial and azimuthal homogeneity of the fiber structure. P will be assumed independent of ϕ since azimuthal variation of the refractive index is not considered. In addition, it is assumed that the grating is only written into the core of the fiber, so that P would have a constant value in the core and would be zero elsewhere (Hochreiner et. al., 2008). Using notation of Erdogan (1997), the refractive index profile in the LPG region can be defined as:

$$n(z) = n_{core} + \delta n(z)\left(1 + v(z) cos\left(\frac{2\pi z}{\Lambda(z)} + \phi(z)\right)\right) \tag{2.2}$$

where $\delta n(z)$ is the average (or DC) refractive index modulation, $v(z)$ represents the visibility of the interference fringes ($0 < v < 1$), $\Lambda(z)$ is the periodicity of the refractive index modulation, $\phi(z)$ represents the phase variation (grating chirp) inside the fiber grating. The LPFG used in this study, has a uniform refractive index perturbation, therefore δn, v and Λ are constant and ϕ is null, as shown in Figure 2.2.

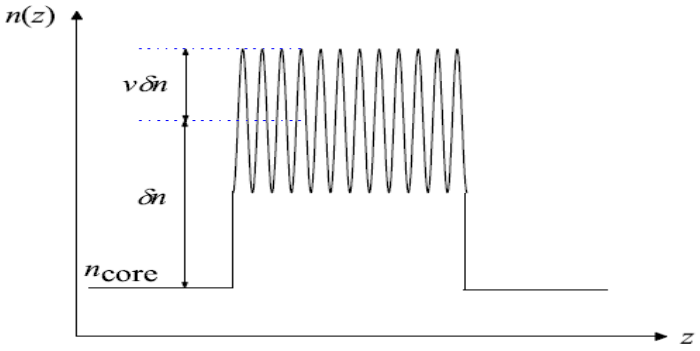

Figure 2.2. Refractive index modulation in uniform fiber gratings (Source: Caucheteur, 2007).

2.2. Coupled-Mode Theory

In this section, we will not provide the derivation of coupled-mode theory (CMT) detailed in many articles and texts (Yariv, 1973; Kogelnik, 1990). We will follow the notation of Kogelnik (1990) and Erdogan (1997).

In an ideal waveguide without grating perturbation, the transverse component of the electric field of the modes can be written as a combination of the ideal modes labeled with j:

$$\overrightarrow{E_t}(x,y,z,t) = \sum_j \left[A_j(z)\exp\left(i\beta_j z\right) + B_j(z)\exp\left(-i\beta_j z\right)\right].\overrightarrow{e_{jt}}(x,y)\exp(-i\omega t) \quad (2.3)$$

where $A_j(z)$ and $B_j(z)$ are slowly varying amplitudes of the j^{th} mode traveling in the $+z$ *(forward)* and $-z$ *(backward)* directions, respectively. The transverse mode fields $\overrightarrow{e_{jt}}(x,y)$ might describe the cladding or radiation LP modes, as given in (Marcuse, 1991). As mentioned before; in an ideal waveguide, modes do not exchange energy, but in the presence of a dielectric perturbation, the modes get coupled. Therefore, the amplitudes $A_j(z)$ and $B_j(z)$ of the j^{th} mode are no longer constant and evolve along the z axis:

$$\frac{dA_j}{dz} = i\sum_k \left\{A_k\left(K_{kj}^t + K_{kj}^z\right)\exp\left[i\left(\beta_k - \beta_j\right)z\right] + B_k\left(K_{kj}^t - K_{kj}^z\right)\exp\left[-i\left(\beta_k + \beta_j\right)z\right]\right\} \quad (2.4)$$

$$\frac{dB_j}{dz} = -i\sum_k \{A_k(K_{kj}^t - K_{kj}^z)\exp[i(\beta_k + \beta_j)z] + B_k(K_{kj}^t + K_{kj}^z)\exp[-i(\beta_k - \beta_j)z]\} \tag{2.5}$$

In these equations, K_{kj}^z is the longitudinal and K_{kj}^t is the transverse (or tangential) coupling coefficient between modes j and k. K_{kj}^z is given by the following expression (Kogelnik, 1990; Erdogan, 1997):

$$K_{kj}^z = \frac{\omega}{4}\iint_{-\infty}^{+\infty} dxdy \frac{\Delta\varepsilon(x,y,z).\varepsilon}{\Delta\varepsilon(x,y,z)+\varepsilon}\overrightarrow{e_{kz}}(x,y).\overrightarrow{e_{jz}}^*(x,y) \tag{2.6}$$

$K_{kj}^t(z)$ is given by the following overlapping integral (Kogelnik, 1990; Vengsarkar et. al., 1996):

$$K_{kj}^t(z) = \frac{\omega}{4}\iint_{-\infty}^{+\infty} dxdy\Delta\varepsilon(x,y,z)\,\overrightarrow{e_{kt}}(x,y).\overrightarrow{e_{jt}}^*(x,y) \tag{2.7}$$

In cylindrical coordinate system, this equation takes the followin form (Kogelnik, 1990; Erdogan, 1997):

$$K_{kj}^t(z) = \frac{\omega}{4}\int_0^{2\pi} d\phi \int_0^{\infty} rdr\Delta\varepsilon(r,z)\,\overrightarrow{e_{kt}}(r,\phi).\overrightarrow{e_{jt}}^*(r,\phi) \tag{2.8}$$

where $\Delta\varepsilon$ is the perturbation of the permittivity, approximately $\Delta\varepsilon \cong 2n_{co}\delta n$ when $\delta n \ll n_{co}$ (Van Brakel, 2004).

Several approximations can be made to simplify the Equations (2.4) and (2.5) for long period fiber gratings:

1. Longitudinal coupling coefficients are neglected because comparing to transverse components, longitudinal components are much smaller ($K_{kj}^z(z) \ll K_{kj}^t(z)$).
2. Comparing to core-cladding couplings, couplings between cladding modes are much weaker, so cladding-cladding couplings are neglected. Only core-core coupling and core-cladding coupling are considered.

3. B components can be neglected; only forward coupling is taken into account.

Consequently, the following formula given in the Equation (2.9) is the general coupled-mode equation. It describes the changes in the co-propagation amplitudes of a mode j resulting from the presence of other modes k near a perturbation (Huang et. al., 2006).

$$\frac{dA_j}{dz} = i\sum_k A_k K_{kj}^t \exp\left[i\left(\beta_k - \beta_j\right)z\right] \tag{2.9}$$

with

$$K_{kj}^t(z) = \frac{\omega}{4}\int_0^{2\pi} d\phi \int_0^{a_{co}} r\Delta\varepsilon(r,z)\left(E_r^k . E_r^{j^*} + E_\phi^k . E_\phi^{j^*}\right)dr \tag{2.10}$$

By using the general coupled-mode equation, the set of differential equations describing mode couplings in single mode long period fiber gratings can be written as the following equations:

$$\frac{dA^{co}}{dz} = iA^{co}K^{co-co} + i\sum_k A_k^{cl} K_k^{cl-co} \exp\left[i\left(\beta_k^{cl} - \beta^{co}\right)z\right] \tag{2.11}$$

$$\sum_k \left\{\frac{dA_k^{cl}}{dz} = iA^{co}K_k^{cl-co} \exp\left[i\left(\beta^{co} - \beta_k^{cl}\right)z\right]\right\} dr \tag{2.12}$$

In a long-period fiber grating written in a single-mode fiber, core mode is always LP_{01} (HE_{11}) mode (cf. Appendix B). In this thesis, the long period grating is assumed to be a circularly symmetric index perturbation, so that the coupling interaction only occurs between HE_{11} and the cladding modes with azimuthal order $\nu = 1$ ($l = 0$). It means; coupling occurs between LP_{01} (or HE_{11}) core mode and the LP_{0m} (or HE_{1m}, $m = 1, 2, 3 \ldots$) cladding modes (Erdogan, 1997 (2)). For this reason, we can now define the k sub-index which is used to specify the cladding modes, as the sub-index $0m$. In addition to the weakly guiding approximation and the other approximations, we assume that the difference in resonant wavelengths is sufficiently high to prevent an overlap, so that each cladding mode coupling can be separately computed (Caucheteur, 2004). Equations (2.11) and (2.12) can thus be simplified by separately considering each clad-

ding mode, and the coupled mode equations for LP_{01} guided mode and LP_{0m} cladding mode ($m = 1, 2, 3 \ldots$) can be expressed as:

$$\frac{dA^{co}}{dz} = iA^{co}K_{01-01}^{co-co} + iA_m^{cl}K_{0m-01}^{cl-co}\exp[i(\beta_m^{cl} - \beta^{co})z] \tag{2.13}$$

$$\frac{dA_m^{cl}}{dz} = iA^{co}K_{0m-01}^{cl-co}\exp[i(\beta^{co} - \beta_m^{cl})z] \tag{2.14}$$

where A^{co} is the amplitude of the fundamental core mode LP_{01} (HE_{11}) and A_m^{cl} is the amplitude of the m^{th} (or k^{th}) cladding mode. K_{01-01}^{co-co} is the self-coupling coefficient of the core mode and K_{0m-01}^{cl-co} is the coupling coefficient between the core mode LP_{01} and the m^{th} (or k^{th}) cladding mode with azimuthal order $\nu = 1$ (or $l = 0$).

In most fiber grating, the induced index change is approximately constant throughout the fiber core and does not exist outside the core. Therefore, we can define the core index, similar to Equation (2.2), but with replacing the $\delta n(z)$ to $\delta n_{eff}(z)$ (Erdogan 1997 and 1997 (2)). To be convenient for calculation we define two new coefficients derived in the Erdogan's paper (1997 (2)):

$$\sigma_{kj}(z) = \frac{\omega n_{co}}{2}\delta n(z)\int_0^{2\pi} d\phi \int_0^{a_{co}} r dr\, \overrightarrow{e_{kt}}(r,\phi).\overrightarrow{e_{jt}}^{*}(r,\phi) \tag{2.15}$$

$$\kappa_{kj}(z) = \frac{v}{2}\sigma_{kj}(z) \tag{2.16}$$

where σ is the "DC" (period-averaged) coupling coefficient and κ is the "AC" coupling coefficient and v is the visibility (Erdogan, 1997). Then the general coupling coefficient can be written (Erdogan, 1997):

$$K_{kj}^{t}(z) = \sigma_{kj}(z) + 2\kappa_{kj}(z)\cos\left(\frac{2\pi}{\Lambda}z\right) \tag{2.17}$$

and the detuning parameter is:

$$\delta_{0m-01}^{cl-co} = \frac{1}{2}\left(\beta^{co} - \beta_m^{cl} - \frac{2\pi}{\Lambda}\right) \tag{2.18}$$

is the detuning parameter for coupling between the fundamental core mode and co-propagation cladding modes.

In long period fiber gratings (also called as transmission gratings) the dominant interaction is the reflection of a mode of amplitude $A_1(z)$ into an identical counterpropagating mode of amplitude $A_2(z)$ ($A_1 = A^{co}$ and $A_2 = A_m^{cl}$ from Equations (2.11) and (2.12)). Equation (2.11) and (2.12) can be simplified by neglecting the rapidly varying z-dependent terms on the right-hand sides of these equations, which is not significantly affecting the amplitudes A_1 and A_2 (keeping only the terms that involve the amplitudes of the particular modes ("synchronous approximation")) (Kogelnik, 1990; Erdogan, 1997). The resulting equations can be written as:

$$\frac{dR}{dz} = i\hat{\sigma}R + i\kappa S \tag{2.19}$$

$$\frac{dS}{dz} = -i\hat{\sigma}S + i\kappa^* R \tag{2.20}$$

where R and S are new amplitudes defined as; $R = A_1 exp[-i\hat{\sigma}z]$ and $S = A_2 exp[i\hat{\sigma}z]$ and $\hat{\sigma}$ is the general DC self-coupling coefficient given by:

$$\hat{\sigma} = \delta + \frac{\sigma_{11} - \sigma_{22}}{2} \tag{2.21}$$

where δ is the detuning factor given in Equation (2.18). And the AC cross-coupling coefficient is $\kappa = \kappa_{12} = \kappa_{21}^*$ as calculated from Equation (2.16).

The boundary condition for this situation is $|S(0)| = 0$, $|R(0)| = 1$. The transmission spectra of the LPFG can be obtained by calculating the transmission (T):

$$T = \frac{R(L)}{R(0)} \tag{2.22}$$

$$T = cos^2\left(\sqrt{\hat{\sigma}^2 + \kappa^2}\, L\right) + \frac{\hat{\sigma}^2}{\hat{\sigma}^2 + \kappa^2} sin^2\left(\sqrt{\hat{\sigma}^2 + \kappa^2}\, L\right) \tag{2.23}$$

2.3. LPFG Simulation Procedures

2.3.1. Introduction to LPFG Transmission Spectrum Modelling

In a LPFG, coupling occurs in the perturbation region, between the core mode and the cladding mode propagating in the same direction (cf. Figure 2.3). A large overlap integral is only possible for modes with similar electric field profiles, and the only cladding modes matching the core-peak distribution of the fundamental mode (i.e. the $LP_{01} (or\ HE_{11})$ are the circularly symmetric (LP_{0m} with m = 1, 2, 3, 4…) modes (James and Tatam, 2003; Erdogan, 1997 (2)). A single-mode fiber's cladding supports several different modes (Lee et. al., 1997). The light coupled to the cladding modes decays due to scattering losses, thus leaving attenuation bands in the transmission spectrum of the fundamental core mode. Therefore, the transmission spectrum of the long period fiber grating has a series of attenuation bands at distinct wavelengths, which satisfy the phase matching condition as (Lee et. al, 1997):

$$\lambda_{res} = \left(n_{eff\_co} - n^{m}_{eff\_cl}\right)\Lambda \tag{2.24}$$

where λ_{res} is the resonant wavelength, n_{eff_co} is the effective refractive index of the core mode, $n^{m}_{eff\_cl}$ is the effective refractive index of the m^{th} cladding mode, and Λ is the grating period.

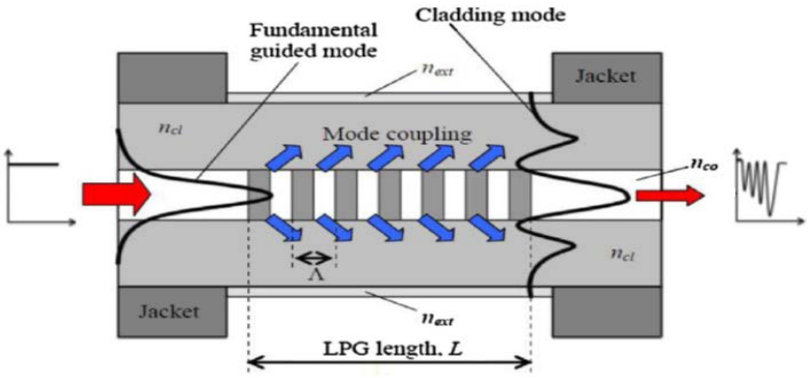

Figure 2.3. Coupling of a fundamental guided core mode to cladding modes in a long-period fiber grating (Source: Hou et. al., 2001).

The modelling of LPG transmission spectra is a complex calculation. There are two approaches for computer modelling: two-layer model (Vengsarkar et. al., 1996), and three-layer model (Erdogan, 1997, 1997 (2)), both methods based on CMT. Vengsarkar (1996), who used two-layer fiber geometry (shown in Figure 2.4 (c)), assumed that the effect of the core is negligible at the cladding ambient interface when determining the cladding effective refractive index. On the other hand, in the three-layer model (shown in Figure 2.4 (a) and (b)), the effect of the core being incorporated when calculating the effective index of the cladding (Erdogan, 1997). In order to avoid complex expressions in the definite mode solutions as derived in Appendix A, both methods use the weakly guided approximation (introduced in Appendix B) to find the effective refractive indices of the provided modes.

In this thesis, the necessary steps to determine the transmission spectrum of the LPFG (used in the experiments) were reproduced by using the two-layer model that presented by Vengsarkar. The simulation codes were re-written based on the theoretical formulation given in references (Vengsarkar et. al. 1996; Erdogan 1997, 1997 (2)), and the MATLAB procedures given in (Van Brakel, 2004).

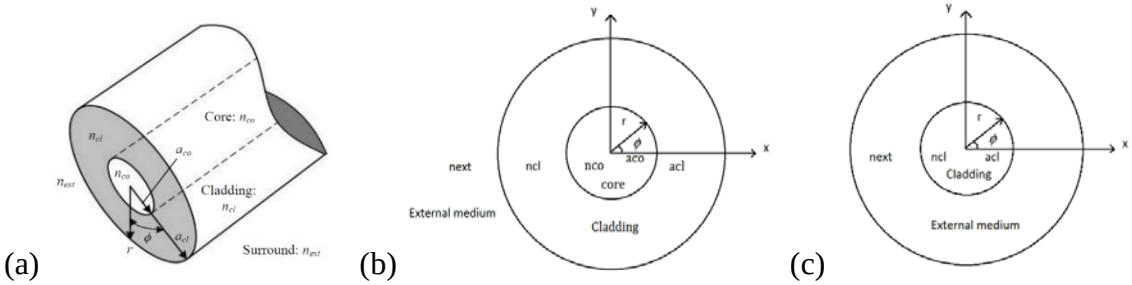

(a) (b) (c)

Figure 2.4. (a) Cross sectional view of an optical fiber, (b) three-layer model and (c) two-layer model cross sectional views of an optical fiber when calculating various cladding modes (Source: Van Brakel, 2004).

The MATLAB codes consist of a series of sub-procedures (for the program flow-chart cf. Figure 2.9). These steps are described in the following sections. In the simplest terms, the simulation procedure steps are as follows:

1. Calculation of the propagation constants of the fundamental and cladding modes,
2. Determining the effective refractive indices of the core and cladding modes,
3. Calculation of the coupling coefficient for coupling between specific modes,
4. Finally, obtaining the complete transmission spectrum by using the coupled-mode theory.

The attenuation peak shape and intensity depend on the electric field profiles of the coupling modes and the value of the coupling coefficient, while the wavelength locations of loss bands (for a fixed grating period) depend on the magnitudes of the effective refractive indices (from the phase-matching condition) (James and Tatam, 2003).

2.3.2. Simulation Procedures of Two-Layer Model for Transmission Spectrum of Individual LPFGs

2.3.2.1. Determining the Effective Refractive Indices of Modes

As mentioned before, in order to determine the resonant wavelengths' values at which mode coupling will take place in the LPFG, the effective refractive index of the fundamental core mode and the effective refractive indices of the cladding modes need to be calculated (James and Tatam, 2003).

a) Effective Refractive Index of core:

In the two-layer model, while the propagation constant of the fundamental core mode is calculated, the fiber geometry is considered as two-layers with a step index refractive index profile. In addition, based on the weakly guided approximation the fundamental core mode can be defined in terms of the LP modes (cf. Appendix B), which can be written with the following dispersion relation (Marcuse et. al., 1979; Cherin et. al., 1983):

$$u_{co}\frac{J_1(u_{co})}{J_0(u_{co})} = w_{co}\frac{K_1(w_{co})}{K_0(w_{co})} \tag{2.25}$$

where J_0 and J_1 are Bessel functions of the first kind, and K_0 and K_1 are the modified Bessel functions of the second kind of order zero and one, respectively. u_{co} and w_{co} are normalized transverse wave numbers (defined in Appendix A). The relation between u_{co} and w_{co} is as follows (Erdogan 1997, 1997 (2)):

$$w_{co}{}^2 = V^2 - u_{co}{}^2 \tag{2.26}$$

V-number is:

$$V = \frac{2\pi a_{co}}{\lambda}\sqrt{n_{co}^2 - n_{cl}^2} \tag{2.27}$$

where n_{co} and n_{cl} are the refractive index of the core and cladding, a_{co} is the radius of the core, and λ is wavelength. Normalized effective index is:

$$b = 1 - \left(\frac{u_{co}^2}{V^2}\right) \approx \frac{n_{eff\_co}^2 - n_{cl}^2}{n_{co}^2 - n_{cl}^2} \tag{2.28}$$

where n_{eff_co} is the effective refractive index of the core. Normalized transverse wave numbers u_{co} and w_{co} can also be written in terms of the fiber's V-number and normalized effective index (Erdogan 1997, 1997 (2)):

$$u_{co} = V\sqrt{1-b} \tag{2.29}$$

$$w_{co} = V\sqrt{b} \tag{2.30}$$

As seen in these expressions, u_{co} and w_{co} depend only on the fiber's physical parameters. To find the core effective refractive index n_{eff_co}, these equations can be used in conjunction with the dispersion relation equation given in (2.25).

After the fiber parameters for the core and cladding materials (radius and refractive indices at a given, -free space- wavelength have been defined as the inputs, V-number is calculated from the Equation (2.27). Then, the eigenvalues that satisfy the dispersion relation are found graphically (using MATLAB): the left- and right-hand sides of the dispersion relation are plotted on the same set of axes, and the intersection point specify the eigenvalue of the dispersion relation and thus also the normalized transverse wave number (u_{co}). In our study, based on the fiber's parameters used, there was only one intersection point (cf. Figure 2.5) (single-mode fiber).

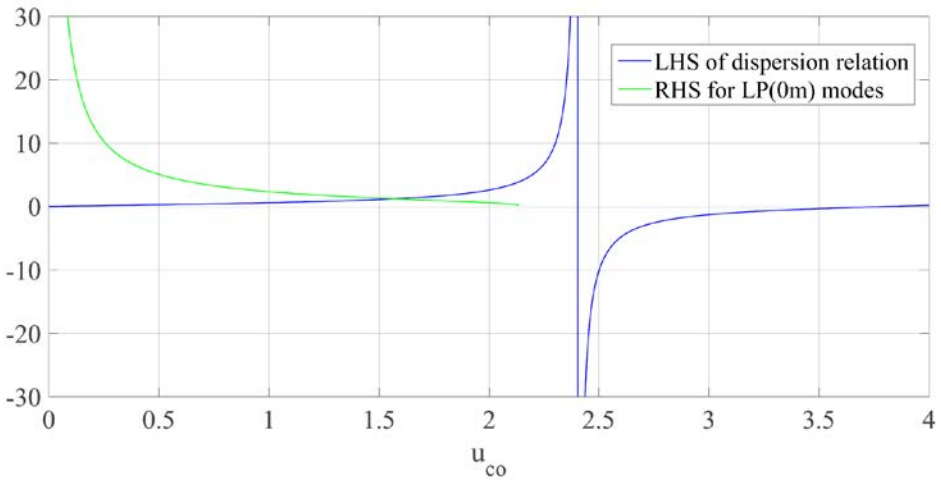

Figure 2.5. Determining transverse wave number (u_{co}) value with graphical method.

The propagation constant of the fundamental core mode can now be calculated from the fiber parameters (n_{co} and a_{co}), determined u_{co}, and the relevant free-space propagation constant (k) for each value of wavelength in the required range (Jones, 1995):

$$\beta_{co} = \sqrt{(kn_{co})^2 - \left(\frac{u_{co}}{a_{co}}\right)^2} = \sqrt{\left(\frac{2\pi}{\lambda}n_{co}\right)^2 - \left(\frac{u_{co}}{a_{co}}\right)^2} \tag{2.31}$$

And finally, the effective refractive index of the core mode is obtained by using the following formula for each wavelength value in the wavelength interval:

$$n_{eff\_co} = \frac{\beta_{co}}{k} = \frac{\beta_{co}\lambda}{2\pi} \tag{2.32}$$

$n_{cl} < n_{neff\_co} < n_{co}$ for the fundamental core mode (Erdogan 1997, 1997 (2)):

b) Effective Refractive Indices of Cladding:

Calculation of various cladding modes effective refractive indices is very similar to the procedure of determining the core effective refractive index. But in this case, the core region is ignored. While the cladding region is assumed as the core region, the uniform external medium is considered as the cladding region (cf. Figure 2.4.c)

(Vengsarkar et. al., 1996). In this way, a simple two-layer waveguide model is defined by using the fiber cladding and external medium. Based on this two-layer assumption, a new V-number is calculated from the equation given in (2.27), but taking in this case, $a_{co} = a_{cl}, n_{co} = n_{cl}$ and $n_{cl} = n_{ext}$: where n_{cl} and a_{cl} are the refractive index and the radius of the cladding, respectively; and n_{ext} is the refractive index of the external medium.

The LP mode dispersion relation in the form of an eigenvalue equation is used once again for finding the each cladding mode propagation constant (Equation (2.25)). Left- and right-hand sides of the dispersion relation are plotted on the same set of axes again, but in this case due to the larger fiber dimensions the graphical representation has different intersection points, and each intersection point specify one of several normalized transverse wave numbers ($u_{cl}^{(m)}$) belonging to a specific cladding mode (cf. Figure 2.6). The number of intersection points also corresponds to the number of cladding modes.

The wave numbers corresponding to the two-layer cladding-ambient geometry are defined as follows (Hou et. al., 2001):

$$u_{cl}^{(m)} = a_{cl}\sqrt{k^2 n_{cl}^2 - \left(\beta_{cl}^{(m)}\right)^2} \tag{2.33}$$

$$w_{cl}^{(m)} = a_{cl}\sqrt{\left(\beta_{cl}^{(m)}\right)^2 - k^2 n_{next}^2} \tag{2.34}$$

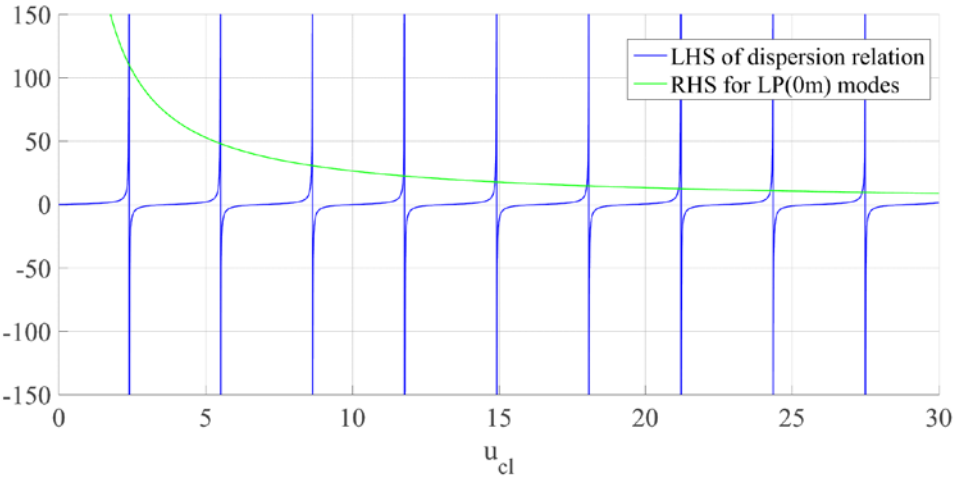

Figure 2.6. Normalized transverse wave numbers ($u_{cl}^{(m)}$).

The propagation constants belonging to the each m-order cladding mode ($\beta_{cl}^{(m)}$) are determined from the fiber's physical parameters (n_{cl}, a_{cl}) , calculated $u_{cl}^{(m)}$ values and the free-space propagation constant at specific wavelengths (k) (Van Brakel, 2004):

$$\beta_{cl}^{(m)} = \sqrt{(kn_{cl})^2 - \left(\frac{u_{cl}^{(m)}}{a_{cl}}\right)^2} = \sqrt{\left(\frac{2\pi}{\lambda}n_{cl}\right)^2 - \left(\frac{u_{cl}^{(m)}}{a_{cl}}\right)^2} \tag{2.35}$$

The cladding effective refractive indices of the m^{th} cladding modes can now be obtained with the following expresssion, for each wavelength value in the required range:

$$n_{eff\_cl}^{(m)} = \frac{\beta_{cl}^{(m)}}{k} = \frac{\beta_{cl}^{(m)}\lambda}{2\pi} \tag{2.36}$$

$n_{ext} < n_{neff\_cl} < n_{co}$ for all the relevant cladding modes (Erdogan, 1997).

2.3.2.2. Determining the Coupling Coefficients

The coupling coefficients for coupling between two co-propagated modes of azimuthal order v and μ can be determined by the formula given in Equation (2.37) (Marcuse in 1991). The azimuthal order $\mu = 0$ for the fundamental core mode and the azimuthal order $v = 1$ for the m^{th} cladding modes.

$$\mathcal{K}_{v=1,\mu=0}^{(cl-co)}(z) = j\sqrt{2}\left[\frac{\gamma\left(\sqrt{\rho}\right)J_\mu(Ka_{co})\,J_v(\sigma a_{co})\sqrt{(n_{co}/n_{cl})-1}}{\pi a_{co}\sqrt{\left|J_{\mu-1}(Ka_{co})\,J_{\mu+1}(Ka_{co})\right|}}\right]$$
$$\div \left|\sigma J_{v-1}(\sigma a_{co})H_v^{(1)}(\rho a_{co}) - \rho J_v(\sigma a_{co})H_{v-1}^{(1)}(\rho a_{co})\right| \tag{2.37}$$

where $H^{(1)}$ is a Hankel function of the first kind, and the other unknowns are as the following expressions (Marcuse, 1991):

$$\sigma = \sqrt{n_{co}^2 k^2 - (\beta_{cl}^{(m)})^2} \tag{2.38}$$

$$\rho = \sqrt{n_{cl}^2 k^2 - (\beta_{cl}^{(m)})^2} \tag{2.39}$$

$$K = \sqrt{n_{co}^2 k^2 - {\beta_{co}}^2} \tag{2.40}$$

$$\gamma = \sqrt{{\beta_{co}}^2 - n_{cl}^2 k^2} \tag{2.41}$$

2.3.2.3. Determining the Detuning Parameter and the Transmission Spectrum

After the coupling coefficients are obtained for the entire wavelength range from Equation (2.37), the detuning parameters are determined from Equation (2.42) for each resonant wavelength in the wavelength interval.

$$\delta = \frac{1}{2}\left(\beta_{co} - \beta_{cl}^{(m)}\right) - \frac{\pi}{\Lambda} = \frac{\pi}{\Lambda\lambda}\left(\Delta n_{eff}\Lambda - \lambda\right) \tag{2.42}$$

where β_{co} and $\beta_{cl}^{(m)}$ are the propagation constant of the core mode and the m^{th}cladding mode, respectively.

Finally, after entering the long period fiber grating parameters to the final step of the MATLAB programme, the entire transmission spectrum of a single long period grating can be simulated from the Equation (2.43) (derived in Section 2.2) (Erdogan, 1997, 1997 (2); Kashyap, 1999).

$$T_{single} = cos^2\left(L\sqrt{\kappa_m^2 + \delta^2}\right) + \delta^2\left[\frac{sin^2\left(L\sqrt{\kappa_m^2 + \delta^2}\right)}{\kappa_m^2 + \delta^2}\right] \tag{2.43}$$

δ is the detuning parameter for co-directional coupling, L is the length of the grating part, and κ_m is (Vengsarkar et. al., 1996; Erdogan, 1997):

$$\kappa_m = \frac{\Delta n}{2n_{co}} \times \mathcal{K}_{v=1,\mu=0}^{(cl-co)}(z) \tag{2.44}$$

Δn; induced core index change

An example theoretical transmission spectrum plot obtained with two-layer model by employing the aforementioned procedure is represented in Figure 2.7.

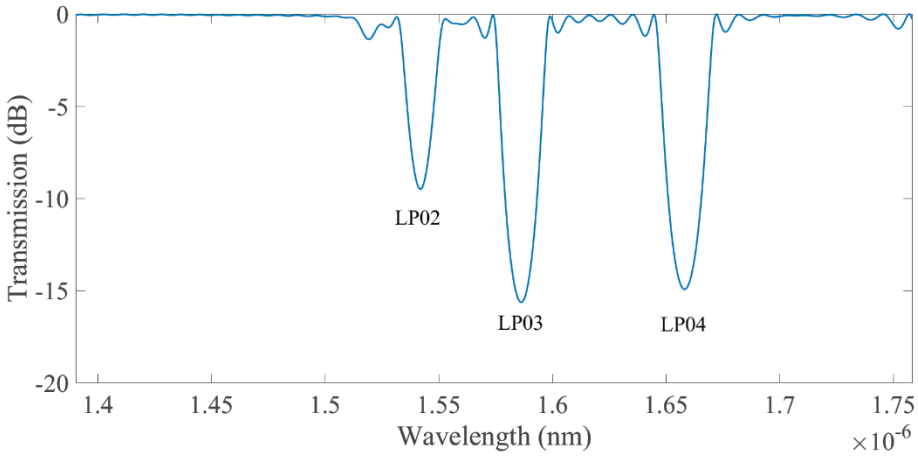

Figure 2.7. Theoretical transmission spectrum of LPFG in air ($n_{ext} = 1$, length of the grating (L) = 30 mm, period (Λ) = 550 μm).

2.3.2.4. Simulation of LPFG as an External Refractive Index Sensor

The sensitivity of LPFGs to refractive index varies depend on the value of the refractive index of the external medium (n_{ext}). It can be divided into three categories (Patrick et. al., 1998):

1) $n_{ext} < n_{cl}$

The events occurring in this range of refractive indices are explained with total internal reflection. A blue-shift (i.e., the resonant wavelengths shift towards smaller wavelengths) is observed at the resonant wavelengths with a decrease in loss band intensity until the refractive index of the external medium is approximately equal to the refractive index of the cladding of the fiber (Van Brakel, 2004). The influence of external refractive index change can be defined by Equation (2.45) (Bhatia, 1999):

$$\frac{d\lambda_0}{dn_{ext}} = \frac{d\lambda_0}{dn^m_{eff\_cl}}\left(\frac{dn^m_{eff\_cl}}{dn_{ext}}\right) \tag{2.45}$$

The second term on the right side of the equation $\left(dn_{eff\_cl}^{m}/dn_{ext}\right)$ is distinct for each cladding mode.

2) $n_{ext} \cong n_{cl}$

When the value of external refractive index approximately equal to the refractive index of the cladding, the cladding layer acts as an infinitely extended medium and does not support discrete cladding modes. In this case, a broadband radiation mode coupling occurs without distinct attenuation bands (Koyamada, 2001). Briefly, when the external RI is equal to the cladding RI, peak resonant bands disappear and the transmission spectrum gets flattened. The region where the refractive index of the external medium is nearly equal to the RI of the cladding, LPG is most sensitive to the external refractive index changes (James and Tatam, 2003; Patrick, 1998). In this RI range, the cladding modes are converted into radiation modes as a result of the lack of total internal reflection, at the cladding boundary. In this case, the dispersion relation given in Equation (2.25) is no longer valid. $\beta_{cl}^{(m)}, u_{cl}^{(m)}\, w_{cl}^{(m)}$ and V-number have complex values, therefore the Bessel functions may have complex part (Adams, 1981).

3) $n_{ext} \geq n_{cl}$

In this case, the cladding modes no longer experience total internal reflection and are referred to as "leaky" modes. The resonance peaks reappear at slightly longer wavelengths than where air is the external medium (i.e. red-shift). In this refractive index range, the spectral shifts in wavelengths are extremely small compared to the case where $n_{ext} < n_{cl}$ (Hou et. al., 2001). As in the case $n_{ext} \cong n_{cl}$, $\beta_{cl}^{(m)}, u_{cl}^{(m)}\, w_{cl}^{(m)}$ and V-number have complex values.

The core mode is not affected by changes in the RI of the external material because it is well confined to the core of the fiber. Therefore, when the RI of the external medium changes, the fundamental mode propagation constant does not change but the cladding propagation constants change. The variation of the first five cladding modes when the refractive index of the external environment changes is shown in Figure 2.8. The variation of cladding mode propagation constants results in change both the ampli-

tude and the position of the resonant dips in the transmission spectrum. In our analysis, we have studied and investigated only the variation of u_{cl}^{4} corresponding to the LP_{04} cladding mode.

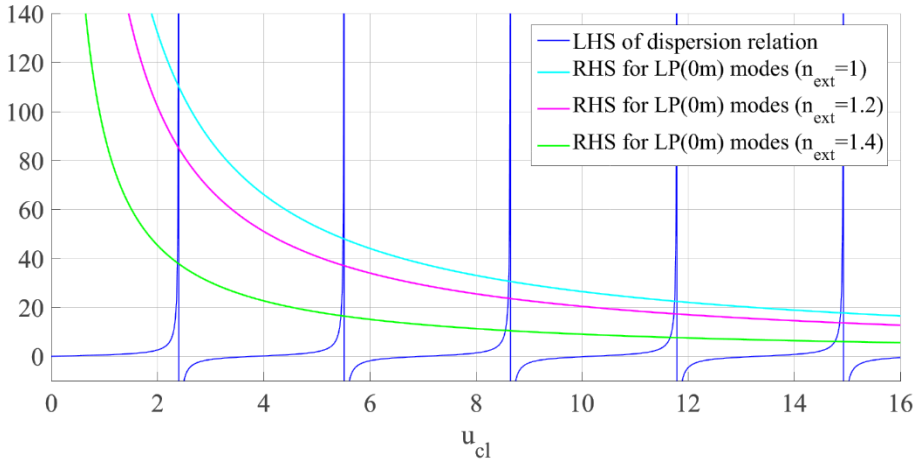

Figure 2.8. Variation of u_{cl}^{X} values for the first five cladding LP modes in different external mediums.

In this thesis, we limited our studies to the first refractive index range which the refractive index of the external medium was smaller than the refractive index of the cladding.

The flow-chart of the simulation used to determine the characteristic spectrum of the LPFG for different external refractive indices which are smaller than the refractive index of the cladding is given in Figure 2.10.

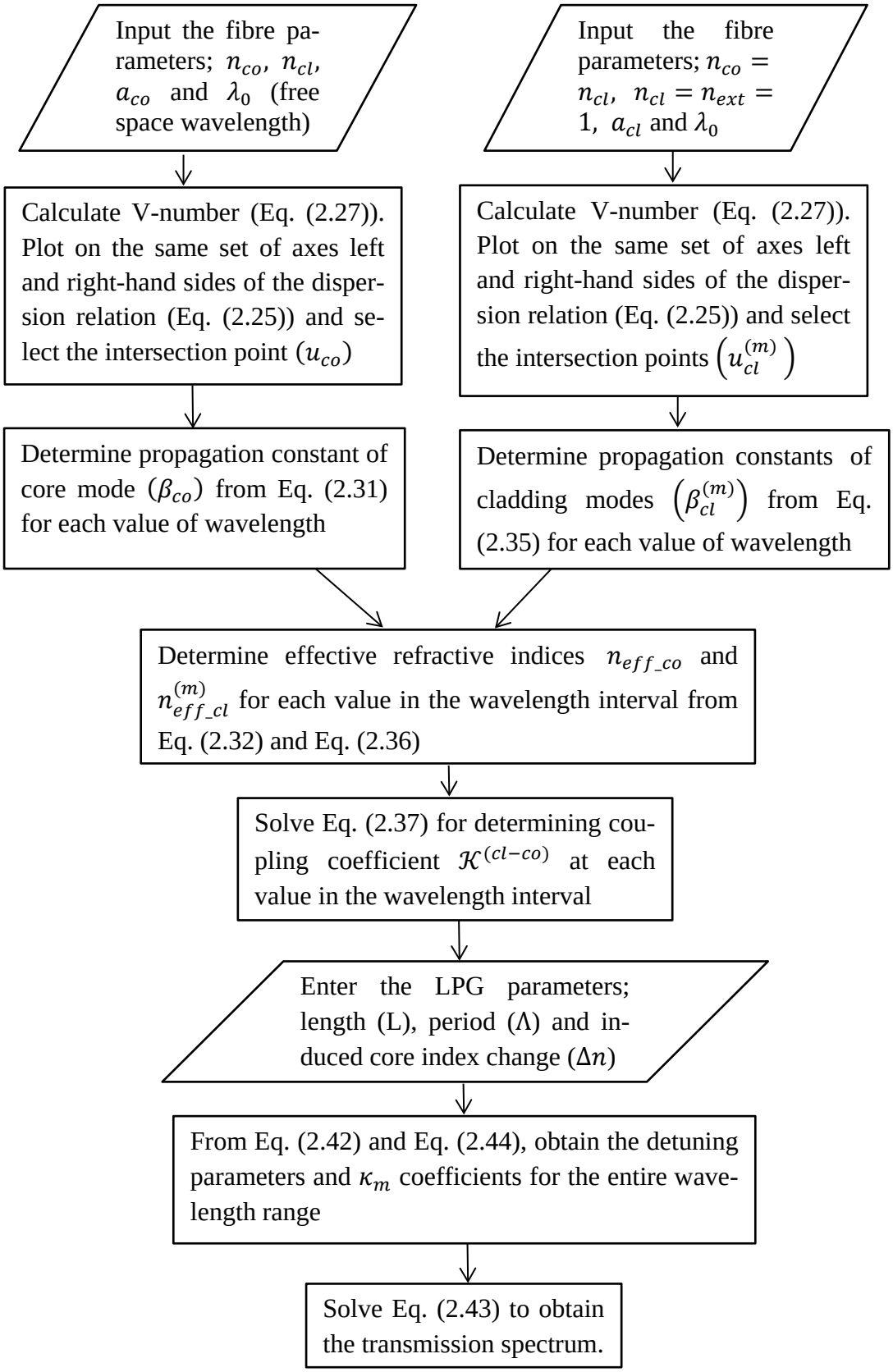

Figure 2.9. Flow-chart of the process used to determine the transmission spectrum of the LPFG in air ($n_{ext} = 1$).

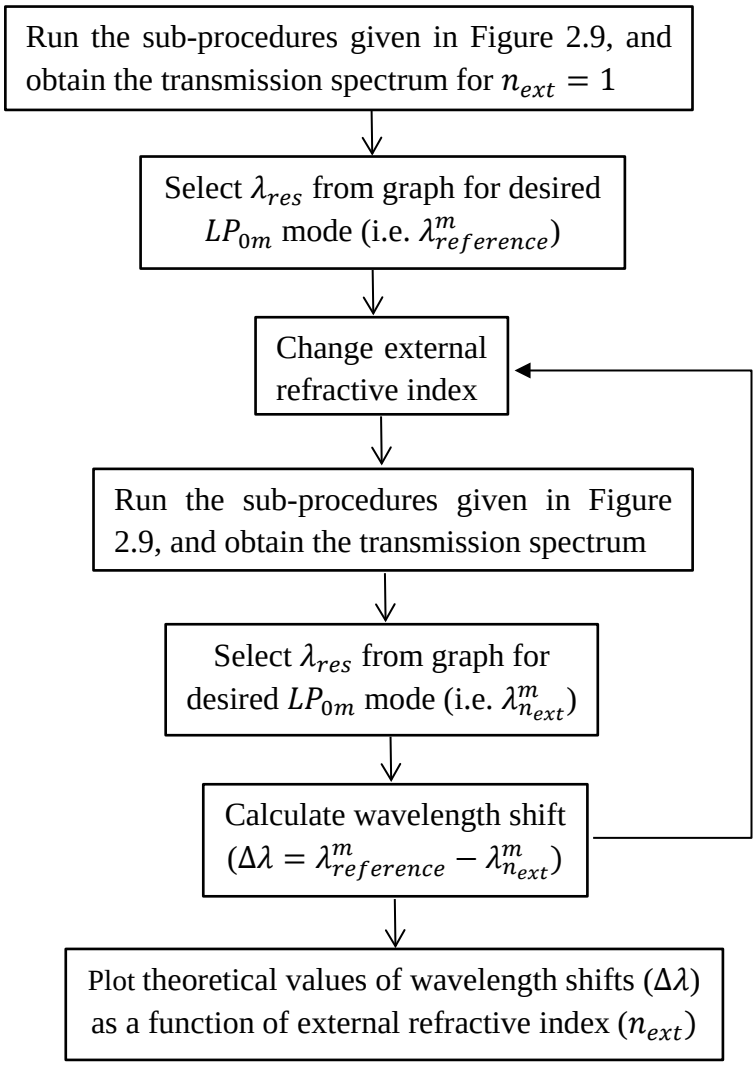

Figure 2.10. Flow-chart of the process used to determine the characteristic spectrum of the LPFG based on the different external refractive indices that are smaller than refractive index of the cladding.

CHAPTER 3

LONG-PERIOD FIBER GRATING-BASED REFRACTIVE INDEX SENSOR

3.1. Experiments

The layout of the experimental refractive index measurement system used to implement long period fiber grating as a sensor head is shown in Figure 3.1. It comprises a broadband light source, and an optical spectrum analyzer (OSA) to observe the transmission spectrum, and a personal computer for data acquisition and analysis.

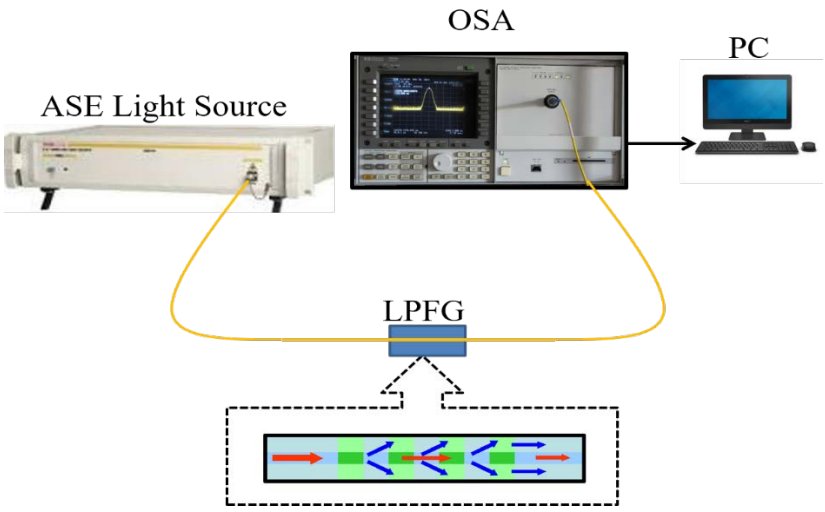

Figure 3.1. Schematic experimental setup.

LPFG was fabricated by University of Mons (UMONS, Belgium) using a conventional single mode fiber (Corning SMF-28) and employing the point-by-point technique. The length of the fabricated grating part is 30 mm, and the grating period is 550 μm.

In the experimental set-up, one end of the fiber containing the LPG part was connected to the ASE light source while the other end connected to the optical spectrum analyzer to interrogate the transmission spectrum. LPFG sensor was fixed from two sides in a position where the transmission bands were clearly observed on the OSA (cf.

Figure 3.2). In this way, effects of strain and bending were avoided. Temperature of the laboratory was also recorded. All the experiments were realized at room temperature (25˚C ± 1˚C).

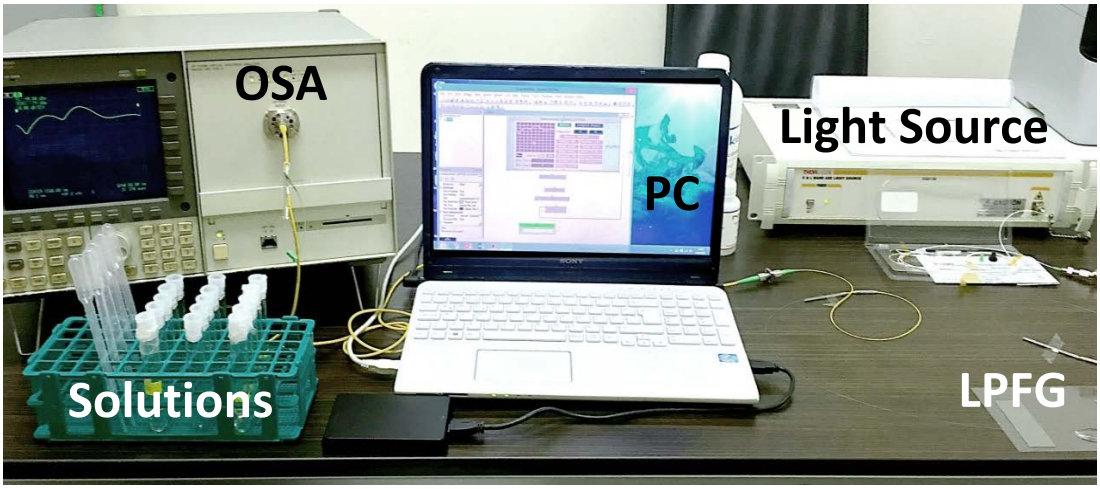

Figure 3.2. Experimental set-up.

Glycerin (also called as glycerine or glycerol) - pure water solutions (prepared with 10% increments from concentration of 10% to 100%) were added dropwise with the help of the dropper on the LPFG sensor part, and the transmission spectrums were recorded for different concentration samples. There was no protective coating on the grating part for sensing the physical changes. Hence, the effective refractive indices of the cladding modes were affected by the changes of the external refractive index. After each measurement with a given glycerin concentration value, sensor part was delicately cleaned with pure water. After removal of excess water, the transmission spectrum of LPFG was observed until it returned to the initial position (typically a few tens of seconds). Then, the same process was repeated with the successive sample having another concentration values. The spectrum of the LPFG in air ($n_{ext} = 1$) was selected as the reference spectrum for all the refractive index measurements. After each measurement, we ensured that the LPFG attenuation dip returns to the initial position (observed on the reference spectrum).

When the measurements were completed, caps of all the test tubes which contained the chemicals were wrapped with parafilm to prevent any changes in the concentration values due to evaporation of water (the refractive index values depend on the percentage of glycerin and water in the samples).

During the time intervals between long-term repeatability measurements, the solutions were kept in a box at a dry place. For the second trial of the experiments (three months after the first trial) whole set of measurements were repeated. The measurement results were consistent with the first experiment set for all the chemicals, except 50% glycerin-pure water solutions which was prepared again.

Experiments of the same type were realized with glucose – pure water solutions. The sugar solutions were prepared with 10% increments from 10% to 50% concentration at the laboratories of Food Engineering Department, IZTECH.

The spectrum traces of the LPFG were acquired and recorded on a PC by using Keysight VEE Pro 9.32 (cf. Figure 3.3). The recorded data were analyzed by using MATLAB program. From the plotted graphics, the resonant wavelengths were determined for each measurement and wavelength shifts ($\Delta\lambda$) compared to the reference resonant wavelength were calculated. The characteristic response curve of the LPFG was determined based on the RI and $\Delta\lambda$ values.

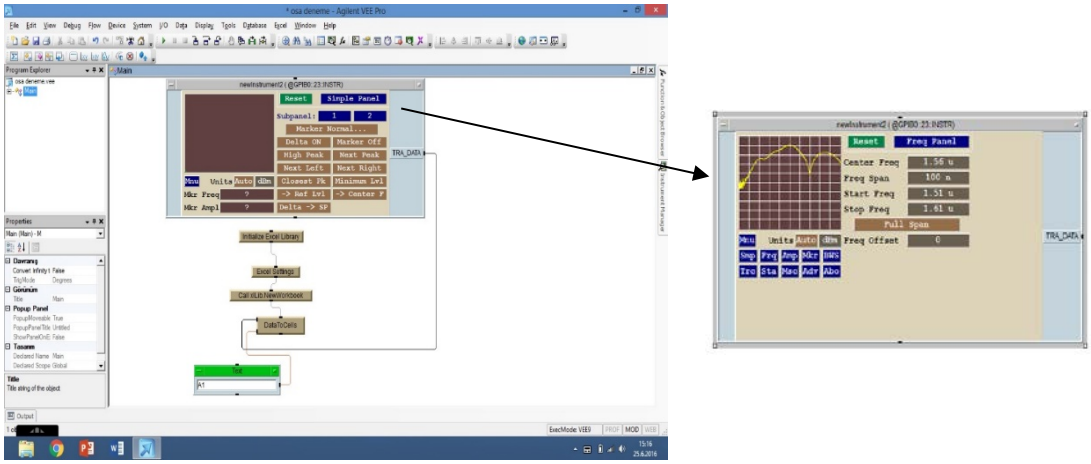

Figure 3.3. Keysight VEE Pro 9.32 interface software screenshots (before and during measurement).

After determining the experimental characteristic response curves (calibration curves) of the LPFG, the unknown refractive index values of the different solutions were determined depending on the wavelength shifts of the resonant wavelengths relative to the reference. For these RI measurements two new glycerine-distilled water solutions prepared at different concentration (65% and 77%) and argan oil were used.

The reference refractive indices of all the solutions were measured with a RE50 (digital Abbe refractometer at ~589.3 nm). The measured values are as shown in Table 3.1:

Table 3.1. Measured refractive index values with a RE50 digital refractometer.

Chemical	**Refractive index**	**Chemical**	**Refractive index**
Distilled water	1,33300	85% Glycerin	1.45462
10% Glycerin	1,34703	86% Glycerin	1,45502
20% Glycerin	1,36587	87% Glycerin	1,45758
30% Glycerin	1,37943	88% Glycerin	1,45969
40% Glycerin	1,39341	90% Glycerin	1.46777
50% Glycerin	1,40163	100% Glycerin	1.47332
60% Glycerin	1,42228	Argan oil	1.39910
65% Glycerin	1.42819	10% Glucose	1.34719
70% Glycerin	1,43612	20% Glucose	1.35972
75% Glycerin	1,44291	30% Glucose	1.37060
77% Glycerin	1.44574	40% Glucose	1.38034
80% Glycerin	1,45441	50% Glucose	1.38677

3.2. Experimental Results

The measured transmission spectrums of LPFG for different concentrations of glycerin-distilled water (Set-1 and Set-2) and sucrose-distilled water solutions are plotted on Figure 3.4, 3.5, and 3.6.

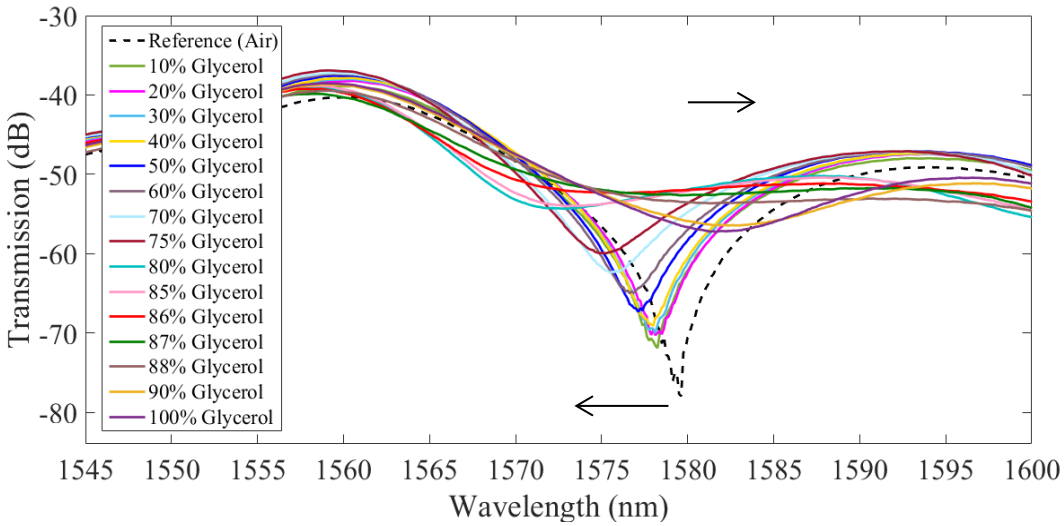

Figure 3.4. Changes in the transmission spectrum of the LPFG for glycerol-distilled water solutions at different concentrations (results for experiment Set-1).

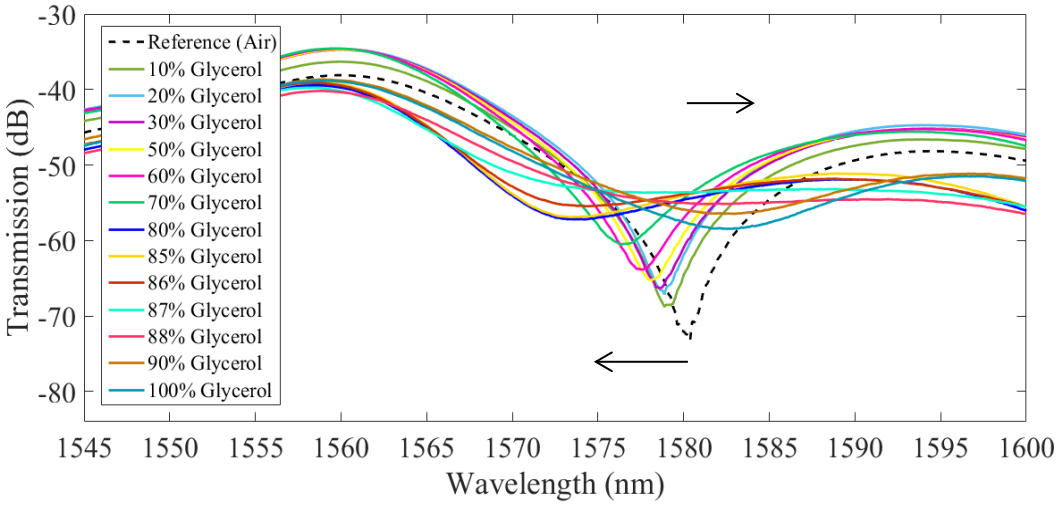

Figure 3.5. Changes in the transmission spectrum of the LPFG for glycerol-distilled water solutions at different concentrations (results for experiment Set-2).

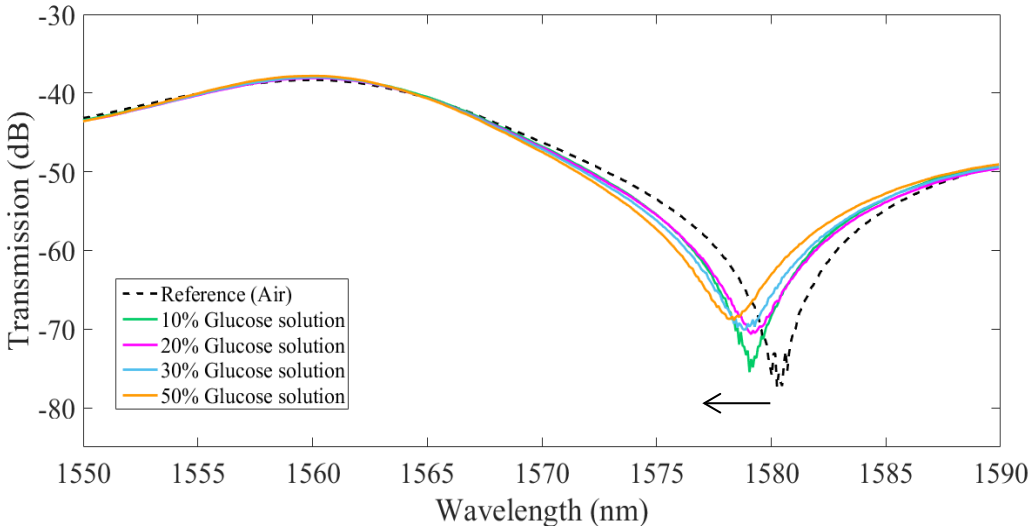

Figure 3.6. Changes in the transmission spectrum of the LPFG for glucose-distilled water solutions at different concentrations.

3.2.1. Enhancement of Signal to Noise Ratio

"*Smoothing operation*" was applied to measured spectrum to reduce the noise level of the measurements (cf. Figure 3.7).

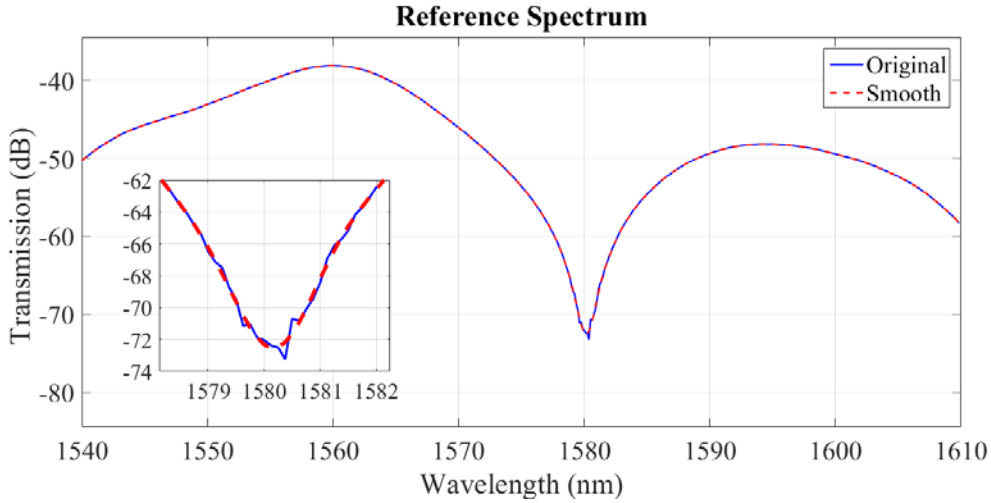

Figure 3.7. Comparison of the original and the smoothed signal. Inset: zoom on the attenuation dip.

Once the smoothing process was applied to the measured spectra, the derivatives of the signals were taken and the coordinates of the points passing through zero were determined, in order to find the dip points of the spectra corresponding to the resonant wavelength values (cf. Figure 3.9).

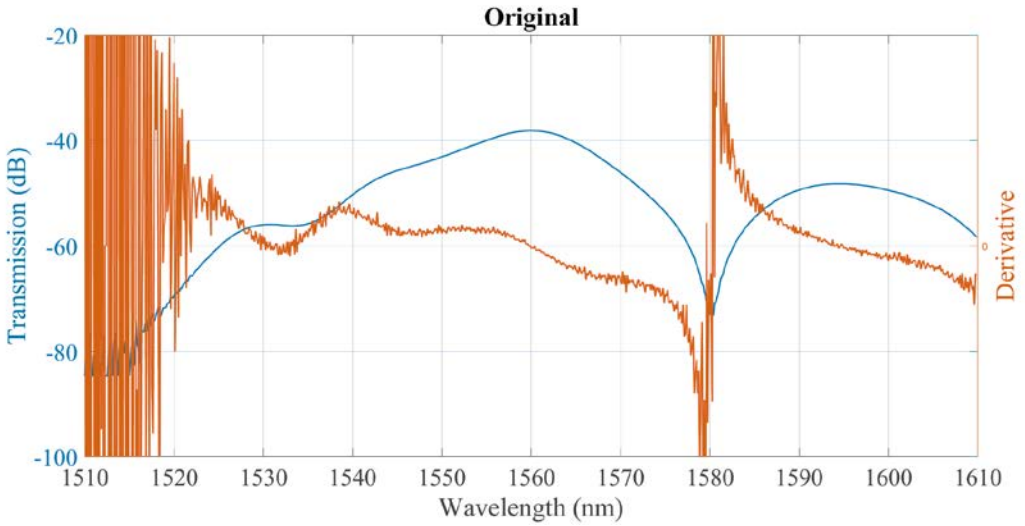

Figure 3.8. Derivative of the original reference (air) transmission spectrum.

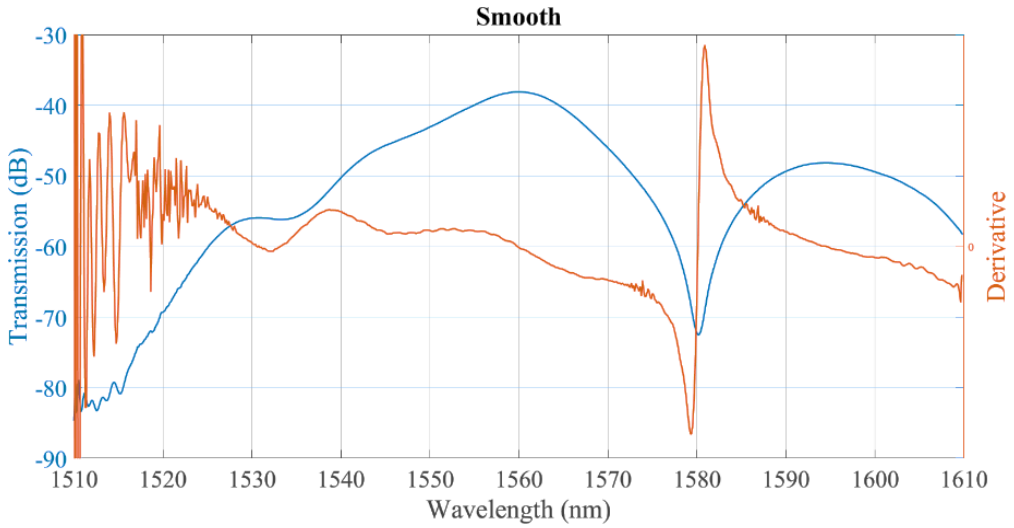

Figure 3.9. Derivative of the reference transmission spectrum after smoothing process.

After determining the shifted resonant wavelength values observed for chemicals having different refractive index values, the wavelength shifts relative to the reference spectrum were calculated (initial wavelength being for the LPFG in air) and listed in Table 3.2.

The measured shift in resonant wavelength as a function of the refractive index of the surrounding medium is represented in Figure 3.10 (glycerin-distilled water, Set-1) and Figure 3.11 (glycerin-distilled water, Set-2).

Table 3.2. Experimental results.

Chemical	**RI $n(\lambda, T)$ (589 nm) (25°C)**	**λ_{res} (nm) Exp. Set-1**	**λ_{res} (nm) Exp. Set-2**	**$\Delta\lambda$ (nm) Exp. Set-1**	**$\Delta\lambda$ (nm) Exp. Set-2**
Air (reference)	1	1579.298	1580.101	0	0
10% glycerol solution	1,34703	1578.133	1578.988	- 1.165	- 1.114
20% glycerol solution	1.36587	1577.952	1578.754	- 1.346	- 1.347
30% glycerol solution	1.37943	1577.772	1578.509	- 1.526	- 1.592
40% glycerol solution	1.39341	-	1578.434	-	- 1.667
50% glycerol solution[2]	1.40163	1577.079	1578.076	- 2.219	- 2.025
60% glycerol solution	1.42228	1576.624	1577.454	- 2.674	- 2.647
70% glycerol solution	1.43612	1575.632	1576.474	- 3.666	- 3.627
75% glycerol solution	1.44291	1575.014	1575.589	- 4.284	- 4.512
80% glycerol solution	1.45441	1572.508	1573.649	- 6.790	- 6.452
85% glycerol solution	1.45462	-	-	-	-
86% glycerol solution	1.45502	-	-	-	-
87% glycerol solution	1.45758	-	-	-	-
88% glycerol solution	1.45969	-	-	-	-
90% glycerol solution	1.46777	1581.572	1582.295	2.274	2.194
100% glycerol solution	1.47332	1581.722	1582.507	2.424	2.406

[2]50% glycerol solution: this solution was different for experiment one and experiment two. For the second experimental sets this solution was prepared again and its refractive index was measured with a RE50 digital refractometer ($n_{ext\_50\%}$ =1.40163). For the first one, the refractive index of the solution was 1.40900.

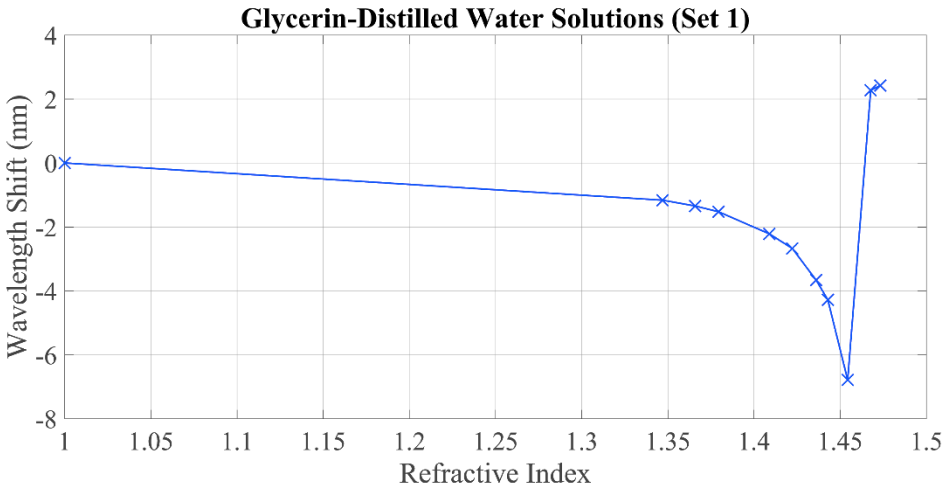

Figure 3.10. Wavelength shifts for glycerin-distilled water solutions (experiment Set-1).

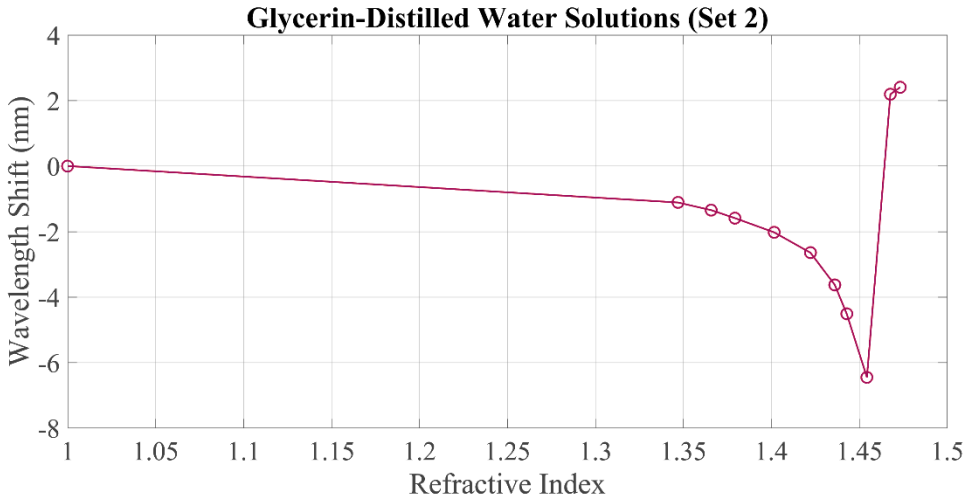

Figure 3.11. Wavelength shifts for glycerin-distilled water solutions (experiment Set-2).

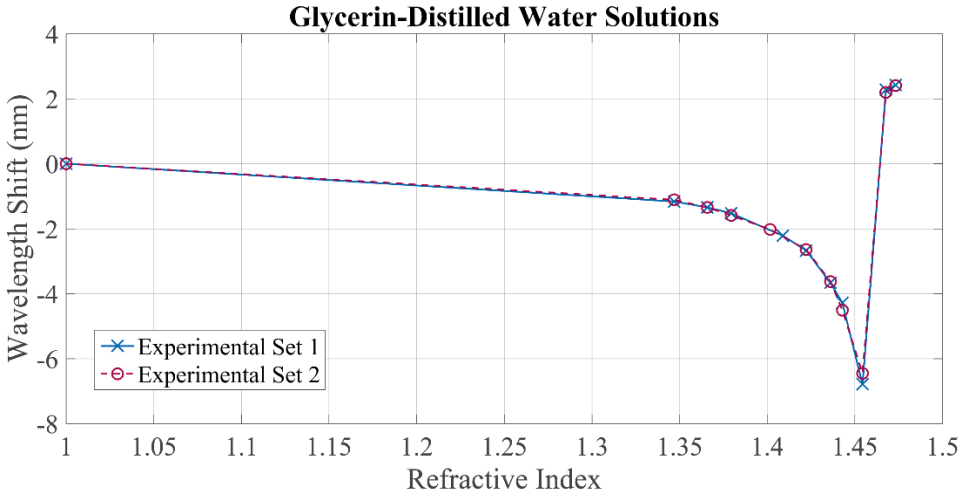

Figure 3.12. Wavelength shifts for glycerin-distilled water solutions for experiment Set 1 and 2.

The wavelength shifts obtained for experimental Set-1 and Set-2 were consistent with each other. This shows the results are reproducible. Small differences may be attributed to the bending sensitivity of the sensor and/or refractive index differences of the solutions due to the evaporation of water.

Experiments were also performed with glucose-distilled water solutions prepared from 10% to 50% (the concentration values of more than 50% were not prepared as the solutions would become saturated after a certain glucose ratio at room temperature). Higher wavelength shifts were observed for 30% and 50% glucose-distilled water solutions compared to the experiments with glycerine-distilled water solutions that have close refractive index values to these glucose solutions. This difference is interpreted as a result of the sugar crystals that may have accumulated on the fiber after each measurement.

The highest sensitivity determined with the sensor was of 217.913 nm/RIU obtained in the RI range of 1.44291-1.45441. The resolution of the sensor was calculated as 4.6×10^{-4} depending on the resolution of the interrogator[3].

[3] Calculation of resolution (Yong et. al., 2012):

$$Resolution_{sensor} = Resolution_{OSA}\times(gradient)^{-1}$$

$$Resolution_{sensor} = 0.1\ nm \times (217.91\ nm/RIU)^{-1} = 4.6\times10^{-4}.$$

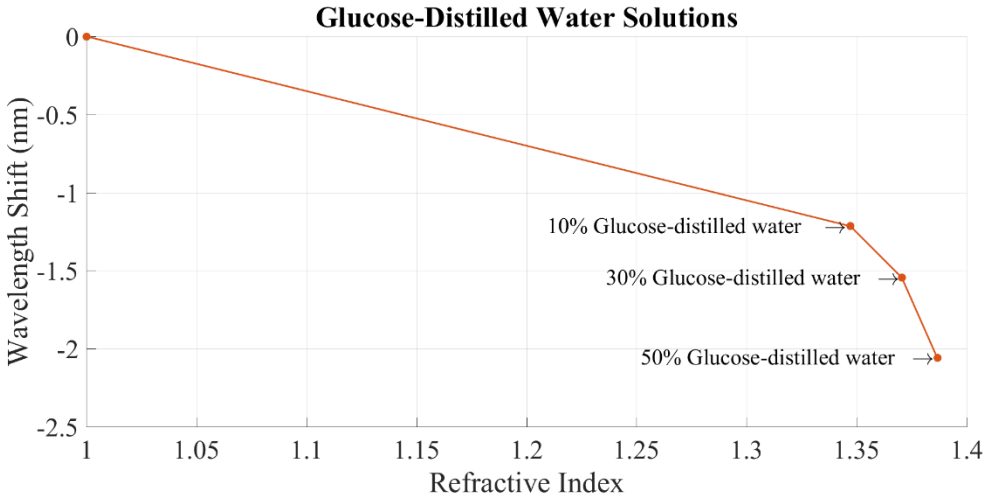

Figure 3.13. Wavelength shifts for glucose-distilled water solutions.

For finding the theoretical resonant wavelengths at different refractive index values, all the refractive index values of glycerin-water solutions were converted to the RI values at light source wavelength[4] (1550 nm was considered as the free-space wavelength) (cf. Table 3.4). The theoretical spectrums were determined for LP_{04} linearly polarize modes (for the flow-chart of the program, cf. Figure 2.10). The simulation parameters to obtain the transmission spectrum of the LPFG written in a standard (*Corning*) SMF28 are given in Table 3.3:

Table 3.3. Parameters of standard single mode fiber and written LPFG.

Parameters	Symbols	Values
Core radius	a_{co}	4.1 µm
Cladding radius	a_{cl}	62.5 µm
Core refractive index[5]	n_{co}	1.4504
Cladding refractive index[6]	n_{cl}	1.4447
Free space wavelength	λ	1550 nm
Grating period	Λ	550 µm
Grating length	L	30 mm
Induced core refractive index change	Δn	$0.5x10^{-4}$

[4] The details of RI-conversion will be discussed in Chapter-4.
[5] Core refractive index was taken as 1.4504 (refractive index of Ge-doped fused silica at 1550 nm).
[6] Cladding refractive index was taken as 1.4447 (refractive index of fused silica at 1550 nm).

The wavelength shifts obtained for two experimental sets of glycerin-distilled water solutions and the corresponding theoretical values plotted on the same graph are shown in Figure 3.14. All the experimental and theoretical results were found to be highly compatible (cf. Figure 3.14 and Table 3.4) (except the slight difference between the experimental and theoretical wavelength shifts observed at 80% glycerin-distilled water solution (n_{ext} =1.4381 at 1550 nm)). This can be attributed to the measurement errors due to the experimental difficulty of the wavelength detection due to the flattening of the spectra as the external refractive index approaches the refractive index of the cladding, and to the experimental deviation from theoretical values due to the occurred radiation modes in this range. And the other small differences may be attributed to the fixed position of the LPFG. This fixed position, where LPG is slightly inclined, may have caused experimentally more wavelength shift by increasing the sensitivity of the sensor to the external refractive index due to the increased evanescent wave interaction.

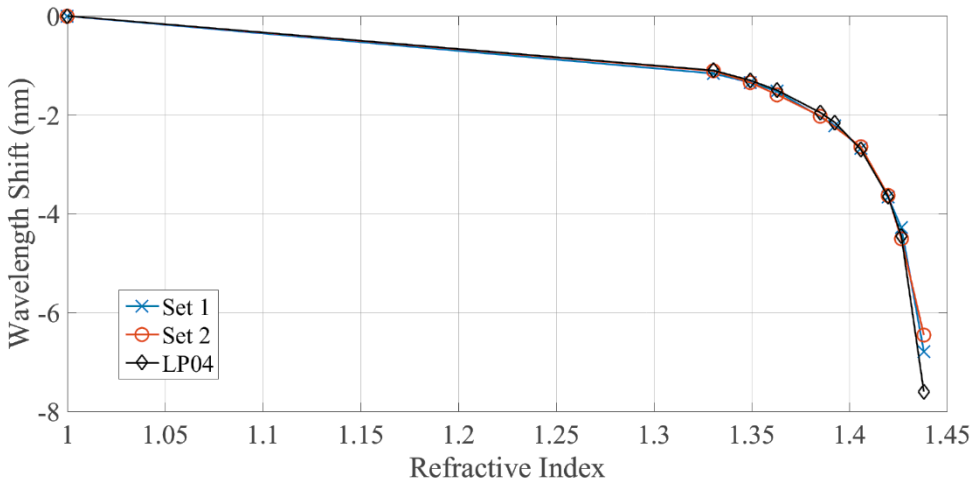

Figure 3.14. Comparison of experimental and theoretical resonant wavelength shifts.

Table 3.4. Experimental and the theoretical values.

n (λ) at 589.3 nm	**n (λ) at 1550 nm**	**Theoretical Δλ (nm) of LP04 mode**	**Experimental Δλ (nm) of LP04 mode (Set-1)**	**Experimental Δλ (nm) of LP04 mode (Set-2)**
1	1	0	0	0
1.34703	1.3305	- 1.102	- 1.165	- 1.114
1.36587	1.3494	- 1.304	- 1.346	- 1.347
1.37943	1.3630	- 1.502	- 1.526	- 1.592
1.40163	1.3852	- 1.956	-	- 2.025
1.40900	1.3926	- 2.155	- 2.219	-
1,42228	1.4059	- 2.705	- 2.674	- 2.647
1,43612	1.4198	- 3.655	- 3.666	- 3.627
1,44291	1.4266	- 4.455	- 4.284	- 4.512
1,45441	1.4381	- 7.601	- 6.790	- 6.452
1.45462	1.4383	-	-	-
1.45502	1.4388	-	-	-
1.45758	1.4413	-	-	-
1.45969	1.4434	-	-	-
1.46777	1.4515	-	2.274	2.194
1.47332	1.4571	-	2.424	2.406

Results for refractive index measurement experiments:

Table 3.5. Resonant wavelength values and wavelengths shifts.

Chemical	**λ_{res} (nm)**	**$\Delta\lambda$ (nm)**
Air (reference)	1579.453	0
Argan oil	1577.583	-1.870
65% glycerol solution	1576.051	-3.402
77% glycerol solution	1574.948	-4.505

Table 3.6. Comparison of the LPFG sensor-deduced refractive index vs reference RI for three chemicals.

Chemicals	**Measured RIs (RE50 refractometer)**	**Calculated RIs from characteristic spectrums**		
		Set 1	**Set 2**	**Theoretical**
Argan oil	1.39910	1.3941	1.3937	1.3974
65% glycerin	1.42819	1.4324	1.4329	1.4324
77% glycerin	1.44574	1.4439	1.4429	1.4431

Table 3.7. RI difference between LPFG sensor-deduced RI value and the reference value (RE50 digital refractometer).

Chemicals	$\|\Delta n\|$		
	Set 1	**Set 2**	**Theoretical**
Argan oil	5×10^{-3}	5.4×10^{-3}	1.7×10^{-3}
65% glycerin	4.2×10^{-3}	4.7×10^{-3}	4.2×10^{-3}
77% glycerin	1.8×10^{-3}	2.8×10^{-3}	2.6×10^{-3}

In the last step of this section, refractive index measurements were tried with the proposed long period fiber grating-based RI sensor for three different solutions (65% and 77% glycerine-distilled water solutions and argan oil). The refractive index values of the solutions were determined by using the experimental and theoretical characteristic response curves depends on the wavelength shifts for each solution compared to the reference spectrum ($n_{ex} = 1$). Experimental (Set-1 and 2) and theoretical spectra were plotted with the reference RIs at 589 nm (rather than at 1550 nm). Hence, the RI values measured with the digital refractometer may easily be compared with the values measured with the LPFG sensor without any further transformation. The determined refractive index values of the solutions were found very close to the reference values measured with the RE50 digital refractometer (cf. Table 3.6 and 3.7). The differences between the values were in the third digit after the decimal point.

3.3. Conclusions

In this section of the thesis, experimental demonstration of using LPFG as a refractive index sensor has been realized.

As a first step, the calibration characteristics (i.e. wavelength-shifts relative to the reference resonant wavelength versus refractive index values) of the LPFG sensor was obtained by using glycerine-pure water solutions at different concentration values. These experiments which were realized twice, having three months between the measurement sets showed a very good repeatability.

The measured characteristic curves were then compared with the theoretical ones obtained by the way of simulations. For theoretical values, all the refractive index values of the solutions at 589 nm were converted to the values at 1550 nm. All of the experimental and theoretical results showed good agreement.

In the experiments, when the RI of the surrounding medium is increased, the resonant wavelengths exhibited a blue-shift, as expected, for the solutions having smaller refractive index than the cladding's RI (these correspond to glycerol-distilled water solutions with concentration values from 10% to 80%, and all glucose-distilled water solutions). For the solutions, whose refractive index values are higher than the cladding's RI (glycerol-distilled water solutions at concentration values with 90% and 100%), a red-shift was observed. When the refractive index values of the liquids were nearly equal to the refractive index of the cladding, the height of the resonance dips decreased and the transmission spectrums became flat (glycerol-distilled water solutions at concentration values with 86% and 87%).

The sensitivity of the sensor was increased as the value of the refractive index of the external medium approached the value of the refractive index of the cladding (cf. Figures 3.10, 3.11. and 3.13). The highest sensitivity determined with the sensor was of 217.913 nm/RIU obtained in the RI range of 1.44291-1.45441, and the resolution was of 4.6×10^{-4}.

In summary, all the experimental results were not only consistent with each other, but they were also in agreement with the theoretical values.

CHAPTER 4

FRESNEL REFLECTION-BASED REFRACTIVE INDEX SENSOR

4.1. Introduction

In this part of the thesis, the refractive index measurements were repeated by using a Fresnel reflection-based sensor that had been previously established at the Optics Laboratory in the framework of Scientific Research Project (BAP-2013-IYTE-02).

Sensor's operation principle was based on the measurement of Fresnel-reflection coefficient at the interface between the optical fiber and the sample. In this sensor, conventional single mode fiber tips were used as sensing points and a multi-wavelength OTDR was used as interrogation unit.

Fresnel reflection-based refractometers have gained popularity in recent years due to their simplicity and easy accessibility (low-cost). In Fresnel-reflection-based refractometers, interrogation can be done with different techniques. The measurements can be made with a source and a photodetector or an OSA, as well as using OTDR. Table 4.1 summarizes the interrogation methods, sensitivities and precisions of different Fresnel reflection-based fiber optic refractometers.

In the conventional single-wavelength OTDR systems, the separation of different sensor points is limited by the OTDR's dead zone. In our study, a multi-wavelength OTDR was used for measuring the modified optical power of the light reflected from the sensing probes. Thanks to this approach, the spatial resolution of OTDR does not limit the distances between sensors point.

Table 4.1. Summary of the Fresnel reflection-based refractometers.

Source	**Interrogator**	**Sensitivity**	**Precision**	**Ref.**
Diode laser (modulated by a pulse train)	Photodetector and computer	-	$2.5x10^{-5}$	(Kim and Su, 2004)
Diode laser (modulated by a pulse train)	Photodetector and digital oscilloscope	-	Short-time: $2.8x10^{-6}$ Long time: $2.9x10^{-5}$	(Basgumus et. al., 2015)
Broadband Source (centered at 1550 nm)	Photodetector	-	Short-time: $8x10^{-6}$ Long-time: $5x10^{-5}$	(Xu et. al., 2013)
Broadband Source (centered at 1538 nm)	OSA	55.2 dB/RIU to 148.1 dB/RIU	-	(Zhao et. al., 2013)
Laser diode (at 635nm)	Photodetector	-	10^{-4}	(Selvas-Aguilar et. al., 2016)
OTDR's light source	Commercial OTDR (1550 nm)	38.70 dB/RIU to 304.73 dB/RIU	Long-time: $2.9x10^{-5}$	(Yeh et. al., 2012; Yuan et. al., 2014)
OTDR's light source	Multi-wavelength OTDR and AWG (1550 nm and 1625 nm)	-	$4.7x10^{-4}$	This work

4.2. Sensing Principle

At the fiber end (flat cleaved fiber end) where the index of refraction differs, a small portion of the incident light is reflected back into the source fiber. This reflection is called as Fresnel reflection, whose power reflection coefficient R can be quantified by the following expression at the interface between fiber end and air:

$$R = \left(\frac{n_1 - n_2}{n_1 + n_2}\right)^2 \tag{4.1}$$

where n_1 is the effective refractive index of the fiber, and n_2 is the refractive index of the second medium which is air in this case ($n_2 = n_{air} = 1.0002739$) (Weast and Selby, 1968).

Power reflection coefficient can be measured by using an optical time domain reflectometer (OTDR) as represented in Figure 4.1.

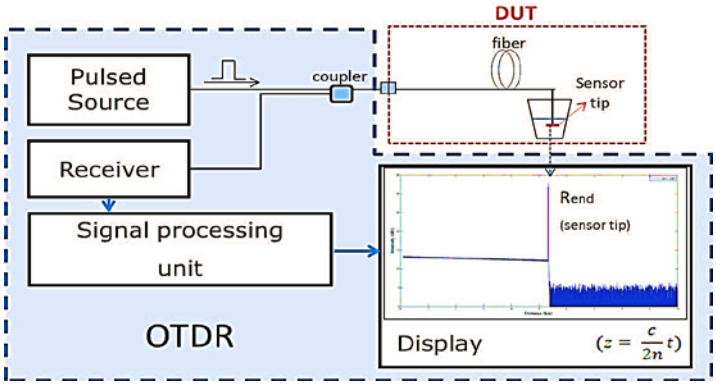

Figure 4.1. Refractive index measurement using OTDR (Source: Yüksel, 2016).

The operation principles of the OTDR-based approach represented in Figure 4.1 are as follows: a series of short optical pulses (probe signal) are injected into the fiber under test (FUT) by the optical source. Returning light (test signal) and the probe signal is separated from each other by the coupler. The test signal reaches to the receiver and its optical power is measured as a function of time. The power change as a function of time depends on the backscattering in the fiber (distributed fiber attenuation), reflection from a splice or connector, bending of the fiber, and any crack in the fiber. While connectors show both reflections and power loss, splices are usually not reflective. After

the measured signal is processed, a graph is shown on the OTDR screen. In this graph, vertical axis shows the optical losses depending on the localized attenuations and reflections and the horizontal axis shows distance in km (cf. Figure 4.2). The power loss is represented in a logarithmic scale (the measured power is displayed in dB).

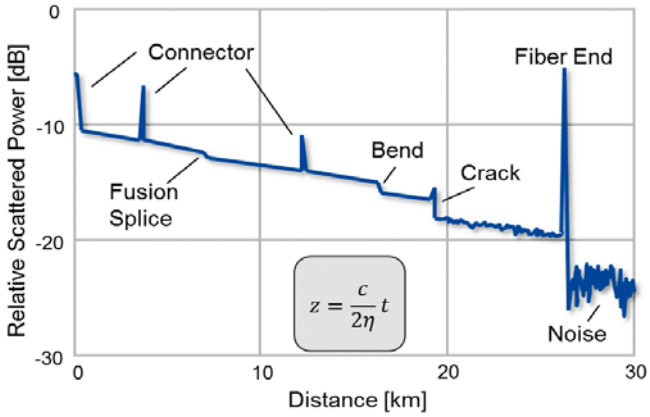

Figure 4.2. Representative measuring of the optical path (Source: online).

The amount of reflected light can be calculated by the differences in the refractive index of the two fibers joined, or any sample (air or chemical) at the end of the fiber. When the fiber tip is immersed into the liquid sample as shown in Figure 4.1, the RI value of the liquid can be determined by measuring the end reflection peak (R_{end}):

$$n_2 = n_1 \frac{\left[1 - 10^{R_{end}/20}\right]}{\left[1 + 10^{R_{end}/20}\right]}, \quad n_1 > n_2 \tag{4.2}$$

$$n_2 = n_1 \frac{\left[1 + 10^{R_{end}/20}\right]}{\left[1 - 10^{R_{end}/20}\right]}, \quad n_1 < n_2 \tag{4.3}$$

The effective refractive index of the fundamental mode (n_1 (or n_{eff})) can be obtained as previously explained in paragraph 2.3.2.1 ($n_1 = 1.4473$ at 1550 nm and 1.4463 at 1625 nm).[7]

[7]For the wavelength of 1625 nm refractive index of the core was found $n_{co} = 1.4496$ by using Sellmeier equation. For 4.5% GeO_2 doped silica fiber the first three A_i and B_i constants are; $A_1 = 0.49211$; $A_2 = 0.62925$; $A_3 = 0.59202$; $B_1 = 0.04807$; $B_2 = 0.11275$; $B_3 = 8.29299$ (Butov et. al., 2002; Kang, 2002) (Kim and Su, 2004).

$$n^2 = 1 + \sum_{i=1}^{3} \frac{A_i \lambda^2}{\lambda^2 - B_i^2} \tag{4.4}$$

In order to measure the reflection, the peak should not saturate the OTDR receiver. If the OTDR receiver is saturated, reflectance peak's top looks flat as shown I Figure 4.3.b. In this case, power reflection coefficient cannot be accurately measured, it only represents a value less than actual.

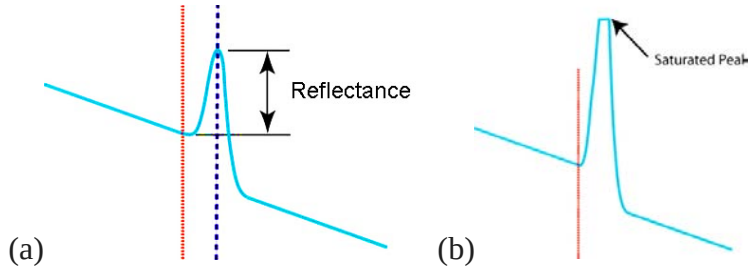

Figure 4.3. (a) Reflected peak, (b) Saturated peak (Source: online).

4.3. Experiments

The same glycerin-pure water solutions (which were used in LPFG-based experiments presented in Chapter 3) have been used again to obtain the calibration characteristics of the Fresnel-based refractive index sensor. The refractive indices were measured with a conventional refractometer (model: RE50 digital refractometer) as well. Figure 4.4 represents the relation between the concentration values and the corresponding refractive indices of the glycerin-distilled water measured by the RE50 digital refractometer. Refractometer's light source emits at 589.3 nm.

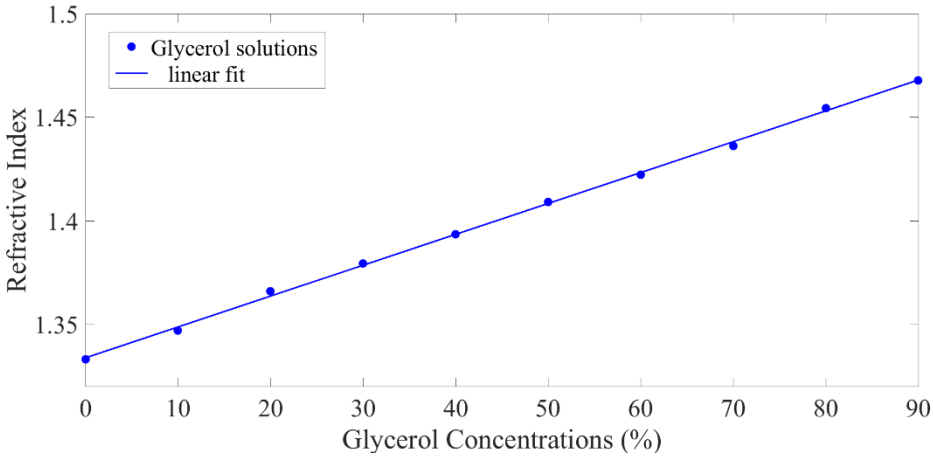

Figure 4.4. Measured refractive indices of the glycerin-distilled water solutions.

The fitting function of Figure 4.4 is; $n = 0.0014904 \times C + 1.3337$, and fitting degree is $R^2 = 0.9999$.

In the experiments, two fiber ends were used as sensing points simultaneously. The optical pulses sent by the interrogation unit (Multi-wavelength OTDR) at two wavelengths (1550 nm and 1625 nm) were separated by a WDM coupler. The fiber tips were standard single mode fibers without the jacket (cut perpendicularly to the fiber axis by using a cleaver). OTDR parameters were set as follows:

Table 4.2. OTDR parameters.

Parameter	**Value**
Distance range	10 km
Averaging time	15 secs
Pulse width	5 ns

The experiments were realized in two parts:

- SET-1: the sensor tip at 1550 nm was immersed in glycerin solutions prepared at different concentrations, while a second sensor tip at 1625 nm was kept in pure water.
- SET-2: the sensor tip at 1625 nm was immersed in glycerin solutions prepared at different concentrations, while a second sensor tip at 1550 nm was kept in pure water.

In both cases, the reflection coefficients from sensor tips were measured on the OTDR display.

Once the calibration characteristics have been obtained for both sensor tips, additional experiments were realized to measure the refractive indices of some chemicals such as acetone, isopropyl alcohol, methanol, and ethanol.

The change of end reflection peak for three different glycerol concentration values (20%, 30%, and 40%) is shown in Figure 4.5.

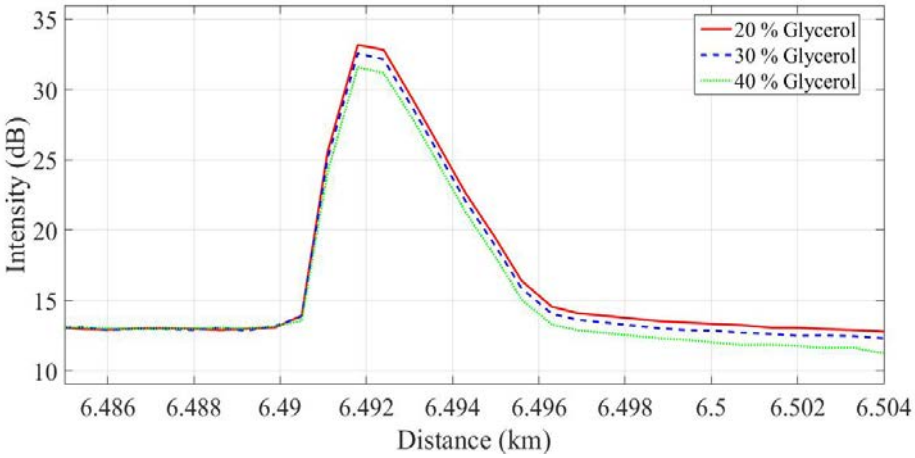

Figure 4.5. Enlarged view of the reflection from the sensor tip when the fiber is exposed to 20%, %30, and 40% glycerol solutions.

4.4. Analysis of Experimental Results

Based on the measured reflection coefficient from the sensor tips, the refractive indices of the prepared solutions were calculated using the Equation (4.2) and (4.3). Table 4.3 shows R_{end} values measured at different wavelengths (at 1550 nm and 1625 nm), and calculated refractive indices using these R_{end} and n_1 values. The absence of highly sensitive test equipment (e.g. electronic micropipette) prevented the preparation of the solution at the aimed concentration values. Therefore, the actual amount of concentration of the prepared chemicals were determined using the RI values measured by RE50 digital refractometer of distilled water, pure glycerin and related chemical[8]. These concentration amounts were then used to determine the refractive indices of the solutions at 1550 nm. Conversion of the refractive indices of the chemicals at 589 nm wavelength to at 1550 nm was realized based on the refractive index values of distilled water

[8]Determination of real concentration values (X_{real}) of a glycerin-water solution at different wavelengths:

$$n_x(\lambda) = \frac{\left(n_{pure\_glycerin}(\lambda) \times X_{real}\right) + \left(n_{water}(\lambda) \times (100 - X_{real})\right)}{100} \quad (4.5)$$

A numerical example for determining the exact concentration value of 70% glycerin solution for 589.3 nm: $n_{water} = 1.33300$, $n_{pure\_glycerin} = 1.47332$ and $n_x = 1.43612$ at 589.3 nm.

X_{real} found from the above equation as $X_{real} = 73.489\%$.

and glycerin at 1550 nm given by Saunders et. al. (2016)[9]. Refractive index transformations could not be done for 1625 nm since no reference value has been provided in the literature so far, for RI values of glycerin and distilled water at 1625 nm.

Table 4.3. Experimental results and reference RI values for glycerol solutions (SET-1).

Concentrations		**Reference RIs**		R_{end} **(dB)**	**Calculated RIs at λ =1550 nm, n_1 = 1.4473**
Originally aimed %	**Real %**	**n(λ) $\lambda = 589.3$ nm**	**n(λ) λ =1550 nm**		
Air	-	1.00027	-	- 16.35	$1.0649 \pm 3.85\times10^{-3}$
Water	-	1.33300	1.3164	- 27.70	$1.3327 \pm 1.25\times10^{-3}$
10	9.999	1.34703	1.3305	- 28.80	$1.3459 \pm 1.10\times10^{-3}$
20	23.425	1.36587	1.3494	- 30.80	$1.3662 \pm 0.95\times10^{-3}$
30	33.089	1.37943	1.3630	- 32.00	$1.3764 \pm 0.80\times10^{-3}$
40	43.052	1.39341	1.3770	- 34.00	$1.3907 \pm 0.65\times10^{-3}$
50	48.439	1.40097	1.3846	-	-
60	63.626	1.42228	1.4059	- 38.40	$1.4129 \pm 0.40\times10^{-3}$
70	73.489	1.43612	1.4198	- 41.60	$1.4234 \pm 0.30\times10^{-3}$
75	78.328	1.44291	1.4266	- 43.80	$1.4287 \pm 0.20\times10^{-3}$
84	85.640	1.45317	1.4369	- 48.70	$1.4367 \pm 0.10\times10^{-3}$
86	86.959	1.45502	1.4388	- 49.40	$1.4375 \pm 0.10\times10^{-3}$
87	88.783	1.45758	1.4413	- 50.50	$1.4387 \pm 0.10\times10^{-3}$
88	90.287	1.45969	1.4434	- 52.00	$1.4400 \pm 0.05\times10^{-3}$
90	96.045	1.46777	1.4515	- 58.97	$1.4506 \pm 0.05\times10^{-3}$
100	-	1.47332	1.4571	- 52.23	$1.4544 \pm 0.05\times10^{-3}$

[9]A numerical example for determining the refractive index value of 73.489% glycerine-water solution at 1550 nm:
$n_{water} = 1.3164$ and $n_{pure\_glycerin} = 1.4571$ at 1550 nm, and $X_{real} = 73.489\%$, n_x were found from the Equation (4.5) as $n_x = 1.419799 \cong 1.4198$.

Table 4.4. Experimental results and reference RI values for glycerol solutions (SET-2).

Concentrations		**Reference RIs (n(λ)) $\lambda = 589.3$ nm**	**R_{end} (dB)**	**Calculated RIs at $\lambda = 1625$ nm, $n_1 = 1.4463$**
Originally aimed %	**Real %**			
Air	-	1.00027	- 16.40	$1.0660 \pm 3.80\times10^{-3}$
Water	-	1.33300	- 28.10	$1.3368 \pm 1.20\times10^{-3}$
10	9.999	1.34703	- 28.50	$1.3415 \pm 1.15\times10^{-3}$
20	23.425	1.36587	- 29.70	$1.3546 \pm 1.00\times10^{-3}$
30	33.089	1.37943	- 31.00	$1.3670 \pm 0.90\times10^{-3}$
40	43.052	1.39341	- 32.70	$1.3808 \pm 0.75\times10^{-3}$
50	48.439	1.40097	- 34.30	$1.3916 \pm 0.60\times10^{-3}$
60	63.626	1.42228	- 38.40	$1.4119 \pm 0.40\times10^{-3}$
70	73.489	1.43612	-	-
75	78.328	1.44291	- 43.90	$1.4280 \pm 0.25\times10^{-3}$
84	85.640	1.45317	- 51.45	$1.4386 \pm 0.10\times10^{-3}$
86	86.959	1.45502	-	-
87	88.783	1.45758	- 54.10	$1.4406 \pm 0.10\times10^{-3}$
88	90.287	1.45969	- 57.75	$1.4426 \pm 0.05\times10^{-3}$
90	96.045	1.46777	- 59.85	$1.4492 \pm 0.05\times10^{-3}$
100	-	1.47332	- 54.84	$1.4515 \pm 0.05\times10^{-3}$

In the Table 4.3 and 4.4. calculated RIs were given by adding the OTDR's precision ($\pm$ 0.1 dB). A systematic difference between the measured and the theoretical R_{end} values was observed. This difference can be attributed to the OTDR's optical return loss (ORL) measurement accuracy, which is $\pm$ 1 dB.

The RI values obtained by using the proposed method versus reference refractive index values calculated for 1550 nm (for experimental Set-1 at 1550 nm) is represented in Figure 4.6. The slope of the linear fit is: 0.83901. The fitting function is; $n = 0.83901\times REF + 0.23157$, and fitting degree is $R^2 = 0.9973$, norm of residuals =

0.0074. The corrected version based on the OTDR's ORL accuracy was plotted on a new graph (Figure 4.7) and the slope closer to 1 was obtained. The slope of the linear fit is: 0.93735 The fitting function is; $n = 0.93735 \times REF + 0.089037$, and fitting degree is $R^2 = 0.9975$, norm of residuals = 0.0081.

It was observed that the refractive index differences occured between the reference and the calculated values due to the accuracy and precision of the interrogation unit decreased as the refractive index of the external medium becomes closer to the effective refractive index value of the core (cf. Table 4.3, 4.4 and 4.5).

The refractive index of the materials varies depending on the wavelength of the light source used for the measurement, as well as on the temperature. For most of the liquids, the temperature dependence of the refractive index ($\partial n/\partial T$) is $10^{-4} {}^{\circ}\mathrm{C}^{-1}$ (Chen et. al., 2011). Temperatures were measured during the whole experiments. The temperature variation of the laboratory was maximum 1 – 2℃, therefore the influence of temperature could be ignored for measurements.

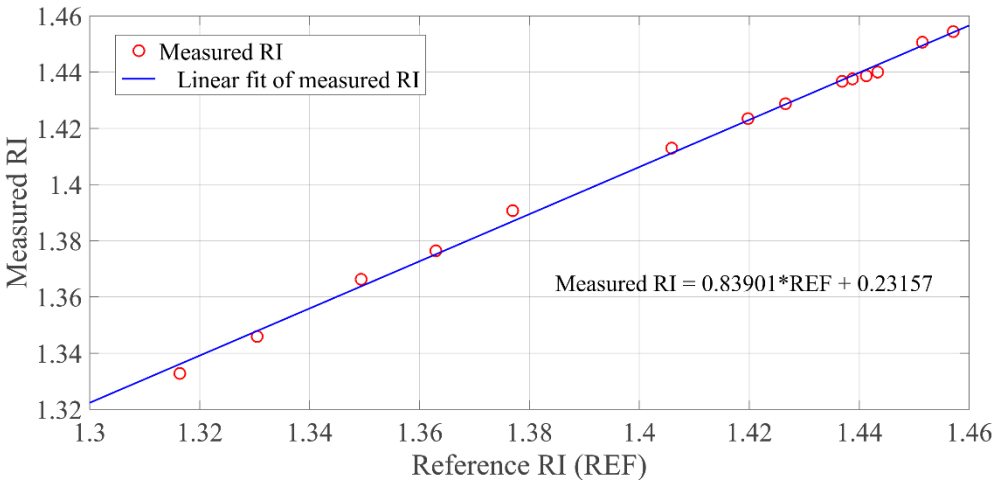

Figure 4.6. The reference refractive index values (at 1550 nm) vs the refractive index values (at 1550 nm) calculated using the proposed method.

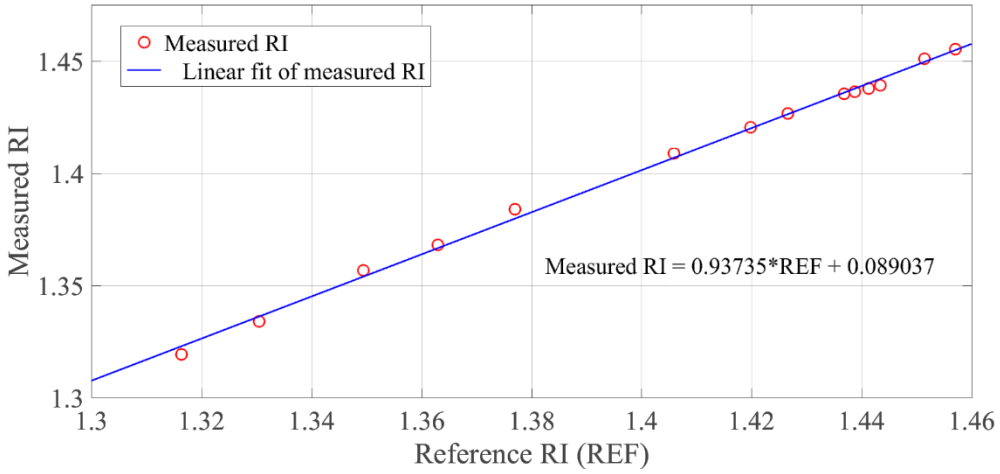

Figure 4.7. The reference refractive index values (at 1550 nm) vs the refractive index values (at 1550 nm) calculated using the corrected R_{end} values.

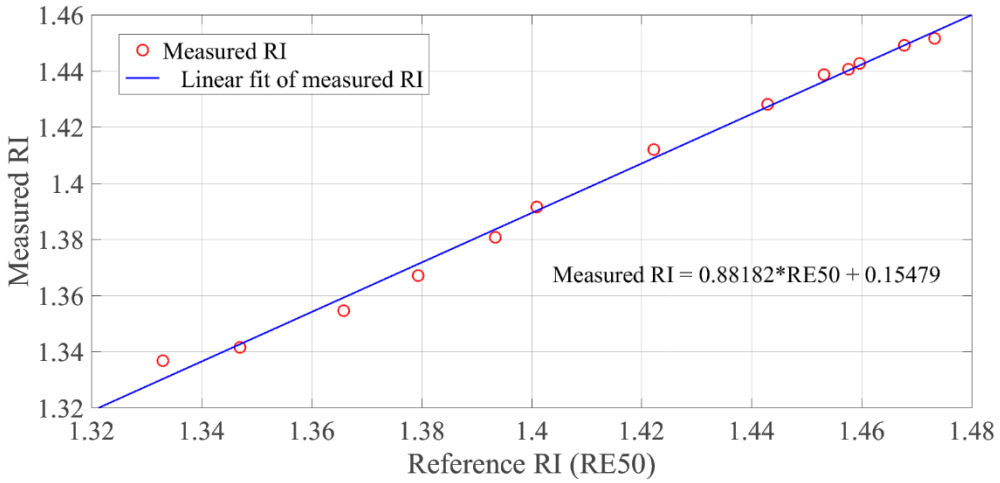

Figure 4.8. The reference refractive index values (at 589 nm) vs the refractive index values (at 1625 nm) calculated using the proposed method.

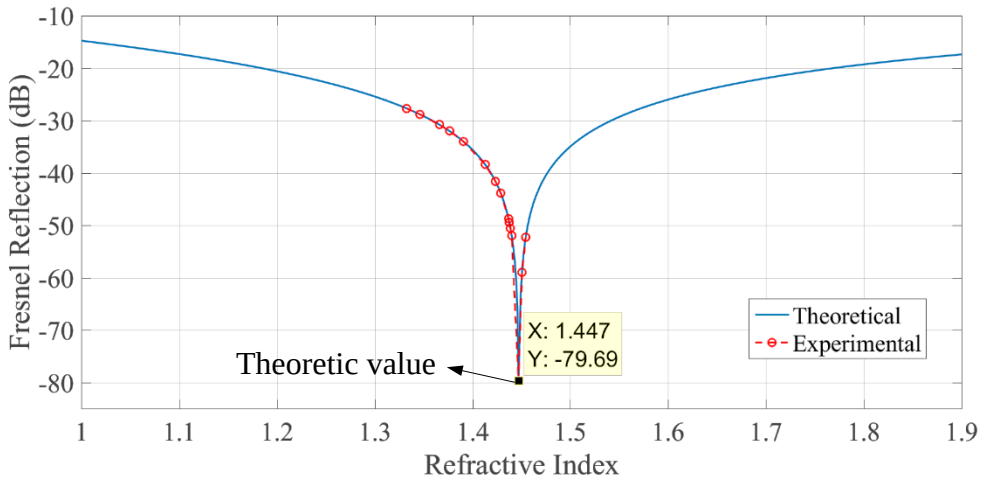

Figure 4.9. Experimental results and the theoretical curve fitting.

Figure 4.9 shows the experimental results (at λ=1550 nm) and the theoretical curve fitting these experimental points in the same graph.

Table 4.5. Differences between calculated refractive indices and reference values.

Reference RIs (λ =1550 nm)	**Calculated RIs, n_1 = 1.4473**	**$\lvert\Delta n\rvert$**
1.3164	1.3327	0.0163
1.3305	1.3459	0.0154
1.3494	1.3662	0.0168
1.3630	1.3764	0.0134
1.3770	1.3907	0.0137
1.4059	1.4129	0.0070
1.4198	1.4234	0.0036
1.4266	1.4287	0.0021
1.4369	1.4367	0.0002
1.4388	1.4375	0.0013
1.4413	1.4387	0.0026
1.4434	1.4400	0.0034
1.4515	1.4506	0.0009
1.4571	1.4544	0.0027

Various Chemicals:

Table 4.6. Experimental results and reference RI values for various chemicals.

Chemical	Reference RIs $(n(\lambda))$		Experimental RIs At 1550 nm	Δn
	At 589 nm	At 1550 nm[10]		
2-propanol	1.3772	1.3661	$1.3756 \pm 0.80\times10^{-3}$	0.95×10^{-2}
Ethanol	1.3614	1.3522	$1.3624 \pm 0.95\times10^{-3}$	1.02×10^{-2}
Acetone	1.3586	1.3483	$1.3605 \pm 0.95\times10^{-3}$	1.22×10^{-2}
Methanol	1.3284	1.3174	$1.3556 \pm 1.05\times10^{-3}$	3.82×10^{-2}

The differences between the values were in the second digit after the decimal point.

The measurements were repeated three times for acetone. And the standard deviation (precision) was obtained as $4.7x10^{-4}$.

Acetone (1625 nm)

Table 4.7. Determination of sensor precision.

Number of measurement	R_{end} (dB)	n_1 = 1.4463	Deviation of each point
1	- 29.9	1.3566	0.0003
2	- 29.9	1.3566	0.0003
3	- 29.8	1.3556	0.0007

The average, variance and the standard deviation were calculated as:

Average (mean) = 1.3563,

Variance = $2.23x10^{-7}$,

Standard deviation = Sqrt(variance) = $4.7x10^{-4}$.

[10] (Saunders et. al., 2016).

4.5. Conclusions

In this chapter, we realized RI measurements by the way of an OTDR-based sensor on the same glycerin-distilled water solutions which were previously used in Chapter 3.

In general terms, the optical fiber sensors have been fast becoming popular in many new application areas (e.g. food industry, environmental analysis and biomedical applications...). The wavelength range implemented in most of such domains is within the classical telecommunication wavelength region as the commercial optoelectronic devices are readily available with reasonable prices.

OTDR is one of these equipments. On the current marketplace, one can easily find out a hand-held OTDR emitting at two wavelengths in the order of a few hundreds of dollars. This opportunity is largely due to the emerging deployment (and related testing requirements) of the optical fiber, particularly in the broadband access networks (e.g. NG-PONs). Hence, the proposed method based on OTDR provides cheap and easy RI measurement capability eliminating all expensive devices (lock-in amplifier, fast pulse modulation of the laser source, fast detectors, GHz oscilloscopes...) and custom fibers (photonic crystal, microfiber, plastic optical fibers) reported in the previous literature.

The measurement of refractive indices of common solvents in the range of telecommunication wavelengths is becoming critical due to aforementioned interest in fiber optic sensing at telecommunication wavelength range. Hence, there is a clear interest for RI measurements to calibrate the RI sensors that operate at 1550 nm window. Another outcome of this chapter is that we report new measurements of refractive indices of common solvents and solutions at both 1550 nm and 1625 nm using a cheap and easy technique, which, we believe, contributes to the previous work.

CHAPTER 5

PERSPECTIVES AND FUTURE WORK

In this part of the thesis, the methods to improve the sensitivity of the LPFG-based refractive index sensors have been reviewed. Then, some preliminary trials have been realized with the test fibers on one of the sensitivity enhancement methods.

5.1. Methods for Sensitivity Enhancement of LPFG: State of The Art

In 1996, it was proved that LPFGs can be used as a refractometer based on attenuation band shift as a function of the external refractive index (Bhatia and Vengsarkar, 1996). Since then, many studies have been done to increase the sensitivity of LPFG-based RI sensors. To this purpose, three different method have been achieved during the last two decades.

5.1.1. Dispersion Turning Point (DTP) Method

When the grating period of the LPFG is short (typically below 200 µm (~ 170 µm), it is possible to couple energy into the same cladding mode at two different wavelengths (Shu et al., 2002). These peaks are called as dual resonant peaks. In other words, for specific periods it is possible to split the optical resonance in two bands, which respectively experience a blue-shift and a red-shift with the variation of several parameters (e.g. external refractive index, temperature, strain, pressure, fiber parameters). And at last, they merged into a single peak. This point is called as dispersion turning point (DTP) (Shu X. et al., 2002) or turn around point (TAP) (Kanka, 2013) and in this case, gratings have an optimal sensitivity to physical and chemical changes. The tuning of LPFG can be done during the fabrication by adjusting the UV-expose, or after the fabrication by reducing the cladding diameter (post-fabrication method). The propagation constants and hence the peak positions of the cladding modes depend on the cladding diameter. In the post-fabrication method, the radius of the fiber can be thinned until the

spectrum reaches to the dispersion turning point (Del Villar et. al., 2016; Śmietana et. al., 2013; Szymańska et. al., 2014).

5.1.2. Thin-film Coating

High refractive index nano-film coating over the cladding surface where the LPFG is written is another method to improve the sensitivity of the LPFG-based sensors to external refractive index. Enhancement of the sensor sensitivity is based on the transition of a cladding mode to the overlay (Del Villar et. al., 2005), and this event is usually called mode transition (MT) (Cusano et. al., 2005). Metal-oxide thin film coating over the LPFG part of the fiber was done for the first time in 2002 (Rees et. al., 2002), and since that time different films with various thicknesses have been tried on the different types of LPFGs. It is possible to optimize the device sensitivity, with adjusting the characteristics of the thin-film (i.e. refractive index and thickness) (Del Villar et. al., 2005 (2)). Control of the coating thickness at nm level has been achieved by various liquid-based (sol-gel (Gu and Xu et. al., 2007), Langmuir-Blodgett (Rees et. al., 2002) and self-assembly monolayers (Wang et. al., 2005)); and vapor-based (physical (Lee et. al., 2007) or chemical vapor-based (Śmietana et. al., 2007)) deposition methods. The highest sensitivity achieved with this technique is the sensitivity of 9100 nm/RIU obtained in 2002 using the combination of the first two sensitivity improvement methods (thin film coated LPFG at near the dispersion turning point) (Pilla et.al., 2012). See Table 3.1 for a summary of the performance data of sensors developed using this sensitivity enhancement method.

Table 5.1. SOTA of the thin-film-coated LPFG based refractometers.

Type of Film	***Film Thicknesses***	***Sensitivity***	***Ref.***
$\boldsymbol{Al_2O_3}$	100, 200 and 300 nm	970 nm/RIU for bare LPFG (in the range 1.4426-1.4524), 3000 nm/RIU for 100 nm-film coated LPFG (in the range 1.437-1.461)	(Zou et. al., 2015)
$\boldsymbol{TiO_2}$	10 to 80 nm	100 nm/RIU for bare LPFG, 215 nm/RIU for 40 nm- and 330 nm/RIU for 60 nm-film coated LPFG (in the range 1.34-1.36), 5250 nm/RIU for 50 nm-film coated LPFG (in the range 1.444-1.456)	(Coelho et. al., 2014)
$\boldsymbol{ZnO}$	29 to 145 nm	56.3 nm/RIU for bare LPFG and 806.3 nm/RIU for 145 nm-film coated LPFG (in the range 1.32-1.36), 3433 nm/RIU for a 58 nm-film coated LPFG (in the range 1.450-1.470)	(Coelho et. al., 2016)
$\boldsymbol{Ag}$[11]	12.3 μm	1660 nm/RIU for Ag-coated LPFG (in the range 1.330-1.337)	(Hu et. al., 2014)

In addition to being used to increase the sensitivity of LPFG-based refractometers, thin film coated LPFGs are used in chemical detection applications such as humidity measurement (Viegas et al., 2009; Corres et. al, 2008; Urrutia et. al., 2016), temperature measurement (Urrutia et. al., 2016; Wang Q. et. al., 2016), gas detection (Hromadka et. al. .2015; Yang et. al., 2014; Wang T. et. al., 2016), and in a variety of biological applications (cf. Table 5.2) (Baliyan et. al., 2016; Bandara et al., 2015; Mathews et. al., 2016; Marques et. al., 2016).

[11] Metal film coating: In this method, the sensing performance was improved via excitation of surface Plasmon resonance (SPR), different from as the other coated LPFGs.

Table 5.2. Summary of biological applications using thin film coated LPFG based sensors.

Type of sensor	*Detection*	*Ref.*
Nanoscale bio-recognition molecules coated-LPFG	Triacylglyceride	(Baliyan et. al., 2016)
Ionic self-assembled multilayer (ISAM) film coated-LPFG	Methicillin-resistant staphylococci	(Bandara et. al., 2015)
Chitosan coated-LPFG[12]	Cholesterol levels	(Mathews et. al., 2016)
Biotin modified-silica core gold shell ($\boldsymbol{SiO_2}$:$\boldsymbol{Au}$) nanoparticles (NPs) coated-LPFG	Streptavidin (SV)	(Marques et. al., 2016)

5.1.3. Reducing the Fiber Radius

A third way of increasing the sensitivity of LPFGs is to reduce the fiber radius. In a recent work, it has been theoretically proved that a sensitivity around 143000 nm/RIU can be achieved by combining these three methods (Del Villar, 2015). But it is difficult to obtain it experimentally. Especially due to the need for high precision during the thin film deposition.

Among the above-mentioned methods, we focused on the reduction of the cladding diameter with the purpose of obtaining a sensitivity enhancement without the need of a thin-film. Reducing the cladding diameter instead of thin film deposition eliminates the requirement the expensive physical (e.g. RF sputter, e-beam evaporator) and chemical deposition (e.g. ALD, PECVD) systems and the cross-sensitivity of the thin-film.

Enhancing the sensitivity of the LPFG-based refractometer by reducing the fiber diameter is based on a simple principle: when the diameter of the fiber is reduced, evanescent wave significantly grows up in the external medium and cladding modes are influenced more from the ambient refractive index. So, when the fiber diameter is reduced, external refractive index sensitivity of the sensor is increased. As mentioned be-

[12] Cholesterol level-sensor was tried with a bare LPFG by the same working group (Mathews et. al., 2012). Chitosan coated-LPFG based sensor sensitivity was more than double of the uncoated LPFG sensor.

fore; thinning the cladding of the LPFG written fibers can also be used for optimizing the spectral behavior of the sensor (tuning the LPFG at DTP).

Reduction of fiber thickness could be done before or after writing the LPFG in an optical fiber. In one of these methods, standard fiber is tapered first, then the LPFG is written in this thinned part (Allsop et. al. 2006; Ji et. al. 2013; Yin et. al. 2014). In the other fabrication method (Del Villar, 2016; Myśliwiec et. al., 2013; Iadicicco et. al., 2007; Martinez-Rios et. al., 2010), after writing the LPFG in the optical fiber, the cladding of the fiber is reduced. Thinned fibers can be fabricated with two methods: etching or heat-pulling method. Heat pulling method (Allsop et. al. 2006; Ji et. al. 2013; Yin et. al. 2014) cannot be used for LPFG written fibers because heating and pulling the fiber changes the grating period and the length of the grating part.

As previously mentioned, etching is a way for reducing the fiber cladding. There are two etching techniques: *wet etching* and *dry etching*. Wet etching is the most common method (Del Villar et. al., 2016; Myśliwiec et. al., 2013; Iadicicco et. al., 2007), where the etching is done with corrosive chemicals (usually, hydrofluoric acid is used). No additional device is necessary. The concentration of etching solution and process time determine the etch rate. This method is simple and inexpensive but requires precise control of critical process parameters, and extreme care must be taken when operating acids due to corrosive and hazardous effects. The other technique is dry etching (Śmietana et. al., 2013, 2014 and 2015; Martinez-Rios et. al., 2010). In this method, the etching process is based on ion bombardment and chemical reactions which occur on the material's surface. Contrary to the wet etching method, dry etching is more repeatable and safer and it is easier to control the parameters. But for dry etching, a special device is necessary (e.g. RIE (reactive ion etching)). This device basically includes a vacuum chamber and RF power supply. The etching process is realized in plasma created by radio frequency (RF) power in the vacuum chamber filled with etching gasses. Reactive ions and radicals, generated in the plasma, are responsible for surface bombardment and chemical reactions, respectively. This method is also called as plasma-based etching. CF4, CHF3, and SF3 are gasses typically used for etching the silicon-based material (Tzeng and Lin, 1987).

5.1.3.1. Wet Etching Techniques in the Literature

Wet etching of LPFGs was first proposed by Vasiliev et al. (1996), but they used it just for the post-fabrication resonant peak positioning mechanism of LPFG spectra. For enhancing the SRI sensitivity of the LPFG-based RI sensor, wet etching method was investigated first by Chiang et al. (2000). In their study, the LPFG was etched with a 15% HF solution. Cladding radius was reduced from 62.5 μm to 61.0±0.5 μm and 59.0±0.5 μm. The etched LPFG was immersed in liquids with different refractive indices and it was observed that the sensitivity of the wavelength shift to the external index could be significantly increased by a small reduction in the cladding radius.

In reference (Myśliwiec et. al., 2013), arc-induced LPFG with period 283 μm was etched in HF buffer (HF:NH4F 1:40) for nearly 18 minutes that resulted in 1.7 μm reduction of fiber cladding radius. This reduction allowed the LPFG spectrum to reach the dispersion turning point (DTP). The sensitivity of the etched LPFG was 5 times higher than the sensitivity of the non-etched LPFG (sensitivity for non-etched LPG was SRI = - 190 nm/RI and SRI = - 971 nm/RIU for etched LPFG).

In reference (Iadicicco et. al., 2008), the reduction in the cladding diameter was limited to 93 μm. The maximum wavelength shift induced by changes in the SRI was 19.6 nm (for $LP_{0,4}$ mode). The same value was 5.3 nm when the fiber diameter was 125 μm. Different from this study in ref. (Martinez-Rios et. al., 2010), cladding of the fiber was etched where only one resonant peak remained in the wavelength range between 1200 nm and 1700 nm. Cladding diameter reduction of 68.24% was obtained (i.e., reduced cladding diameter was 39 μm). The maximum wavelength shift was up to 230 nm when the external refractive index is changed in a range between 1 and 1.456 (sensitivity of order 20 000 nm/RIU).

In reference (Iadicicco et. al., 2007), 12% HF acid solution was used for cladding etching. 125 μm diameter claddings were etched with different thicknesses. Remaining diameters were 121.4, 119.7, 117, 112.9, 110.8 and 103.8 μm. Compared to other LPFGs with different etching rates, the maximum sensitivity to external refractive index was obtained for the LPFG with 104 μm cladding diameters. When the SRI changed from 1 to 1.45, the resonant wavelength shift of the $LP_{0,6}$ mode was about 12.1 nm for the original 125 μm-diameter LPFG, and 71.6 nm for 104 μm-diameter LPFG. in addition, for the same SRI range, the wavelength shifts related to the $LP_{0,5}$ and the

$LP_{0,4}$ modes were 4.7 and 1.5 nm for the original 125 μm-diameter LPFG and 13.6 and 4.9 nm for the 104 μm-diameter LPFG, respectively.

In reference (Del Villar et al., 2016), two LPFGs with the same gratings period (210 μm) were used. First LPFG was etched up to 75 μm with a slow etching process (10% HF solution) to obtain the $LP_{0,6}$ DTP band, and the second LPFG was etched up to 35 μm with a faster etching process (40% HF solution) to obtain the $LP_{0,3}$ DTP band. A variation of more than 100 nm was observed in both cases, when the LPFGs were immersed in the calibrated index solutions (glycerine-water). The sensitivity in the range 1.353 – 1.398 for $LP_{0,6}$ DTP was 1343 nm/refractive index unit (nm/RIU), whereas the sensitivity for $LP_{0,3}$ DTP improved to 3166 nm/RIU. The highest sensitivity was achieved by 8734 nm/refractive index unit (RIU) for the $LP_{0,3}$ mode in the 1400 – 1650 wavelength range.

5.1.4. Combination of Etching and Coating

In order to improve the sensitivity of the LPFG written in standard optical fiber to external RI, etching and coating can be applied at the same time (thin film coating of thinned fiber) (Śmietana et. al., 2015, 2015 (2), and 2016; Shen et. al., 2010). Usually, the etching process is used for tuning the LPFGs at DTP.

Shen et al. (2010), first etched the cladding with hydrofluoric (HF) acid, and then coated this thinned grating part with 20 μm-thick zeolite film. In the experiment, the resonant wavelength shifted from 1542 nm (in air) to less than 1530 nm (in water), and the shift was larger than 12 nm. The same value was 3 nm for the thinned uncoated LPFG and 1 nm for the original LPFG. Thinned-coated LPFG was more sensitive to external refractive index than thinned-uncoated LPFG and the original LPFG. In this application, LPFG did not etched until the spectrum reach to the DTP. Decreases in cladding diameter improved evanescent wave interaction and, zeolite coating outside the etched fiber make the interactions between evanescent wave and external liquids more efficient. Hence, both processes enhanced the refractive index sensitivity of the LPFG sensor.

In reference (Śmietana et. al., 2015 (2)), after fabrication and etching processes LPFGs were coated with the TiO_2 thin film by atomic layer deposition (ALD) technique. In order to reduce the fiber cladding diameter LPFGs were immersed in highly

concentrated HF (40%) and subsequently HF buffer (6 to 1 volume ratio of 40% NH4F in water and 49% HF in water). The aim of the etching process was shifting the resonant wavelength to the dispersion turning point, where the highest sensitivity can be obtained (post-fabrication method). In the experiments, when the TiO_2 overlay thickness reached 70 nm, 6200 nm/RIU sensitivity was achieved. In addition to this, when the TiO_2 surface was functionalized with endotoxin binding protein (adhesin) of T4 bacteriophage, LPFGs were shown to have improved sensitivity to bacteria endotoxin (E. coli B lipopolysaccharide) detection.

5.1.5. Combination of Etching, Coating and DTP Method

In reference (Śmietana et al. 2016), the etching process was used to tune the properties of the grating up to the dispersion turning point (DTP). The MT was obtained with deposition of Al_2O_3 overlays. Atomic Layer Deposition method (ALD) was used for coating similar to the reference (Śmietana et. al., 2015 (2)), but different from reference (Śmietana et. al., 2015 (2)) etching was performed for both cladding and Al_2O_3 overlay in this work. The aim of the etching process of overlay was; tuning the working point back toward the DTP when it was shifted away from this point after film coating and in this way, increasing the sensitivity. Wet etching method was preferred where; hydrofluoric acid (HF) was used as corrosive chemical. In the experiments, this post-deposition fine-tuning of the overlay thickness resulted in a remarkable increase in RI sensitivity at the DTP of the $LP_{0,9}$ cladding mode. At an external RI (n_{ext}) above 1.39 RIU, the DTP of $LP_{0,10}$ became visible, and its RI sensitivity increased to 9,000 nm/RIU. In the next stage of the same work, the cladding of the fiber was etched deeper and coated with thicker overlays (up to 201 nm in thickness). This process allowed the sensitivity to reach values of over 40,000 nm/RIU in a narrow RI range. The sensitivities obtained in this work were the highest values obtained experimentally to date.

In reference (Śmietana et al. 2015) (the same working group as in reference (Śmietana et. al, 2016)), to increase the refractive index (RI) sensitivity of LPFG sensor, the fiber was first etched using a reactive ion etching (RIE) device for tuning the LPFG at DTP. The cladding was over-etched to prevent resonant wavelength for the water ($n_{ext} = 1.3330$) from moving away from the DTP, after coating the thin film. The thinned fiber was next coated with diamond-like carbon (DLC) nano-film using radio

frequency plasma enhanced chemical vapor deposition (RF PECVD) device. RI sensitivity was enhanced up to 12,360 nm/RIU and -10,090 nm/RIU for red and blue shifting resonances, respectively in narrow RI range (1.3344-1.3355), and over 2000 nm/RIU in broader RI range (1.34-1.356). For the thinned LPFG (not coated), the sensitivity was 4,375 nm/RIU in the same RI range.

5.2. Preliminary Trials: Determining the Etch Rate with Test Fibers

To obtain the etch rate of silica fiber (Corning SMF28), some etching tests were done with SMFs and FBGs written in standard optical fiber. Wet etching (chemical etching) method was preferred. All test procedures were done at Ermaksan Optoelectronic R&D Center's Class 6 and Class 7 cleanrooms (ISO 1000 and ISO 10000 cleanrooms)[13].

Two different etching techniques had been tried in the etching process for window stripped fibers:

- **Method-1:** The first of these was immersing the fiber in HF bath (5 ml) (bath's material was PP).
- **Method-2:** The second was fixing the fiber on a natural polypropylene (PP) material and dropping HF (1 ml – 20 drops) to the bare part of the fiber. Polypropylene is chemically resistant to the hydrofluoric acid.

But before all, if there is a protective (polyacrylate) coating on the fiber (cf. Figure 5.1), it was stripped away with an automatic fiber window stripper and then the fiber was cleaned with isopropyl alcohol to remove the residues from the coating. Highly concentrated HF (40%) solution was used for etching. After different durations, HF solution was removed from the fibers' surfaces and the etched regions of the fibers were rinsed with deionized water for a few minutes. However; it would be better to leave the fiber in the deionized water overnight.

- **Additional Method (Method-3):** In this method, the fiber was stripped from the cleaved end and perpendicularly immersed into a 5-ml dropper filled with 40% HF solution. After being waited for 35 and 55 minutes, the same tip was im-

[13]Due to the privacy policy of the company, the brand names and the models of the devices that were used for the experiments were not given and the photographs of the laboratory, devices and test equipment had not been taken.

mersed in a beaker filled with deionized water and rinsed for a few minutes. However, this method cannot be used for window etched-fibers, it can be used to make fiber sensor tips.

All experiments were done in the wet bench with using personal protective equipment, due to the corrosive effects of hydrofluoric acid.

The images of test fibers before and after the wet etching were taken with an optical microscope and the remaining diameters of the fibers were measured. Some fibers were also observed with scanning electron microscope (SEM).

Table 5.3. Summary of etched FBG-based RI sensors.

Remaining Diameter	***RI Range***	***Sensitivity***	***Resolution***	***Ref.***
11 µm	1.333-1.345	2.66 nm/RIU	$5x10^{-4}$	(Asseh et al., 1998)
8.3 µm	1.333-1.341	7.3 nm/RIU	-	(Pereira et al., 2004)
3.4 µm	Near 1.44	1394 nm/RIU	$7.2x10^{-6}$	(Chryssis et al., 2005)
5.73 µm	1.330 to 1.359	49.44 nm/RIU	-	(Luo et al., 2012)
2.2 µm	1.3265	428.07nm/RIU	$2.24x10^{-4}$	(Zhou et al., 2014)
9.3 µm	Near 1.318	2.9 nm/RIU	$1.4x10^{-5}$	(Zhang et al., 2013)
5 µm	Near 1.445	317.5nm/RIU[14]	-	(Xu et al., 2014)
10 µm	1.320-1.342	30 nm/RIU	$2x10^{-4}$	(Kumar et al., 2015)

[14] Theoretical value

5.2.1. Results

Process times, etch rates and the images of the etched test fibers are as shown in the following figures.

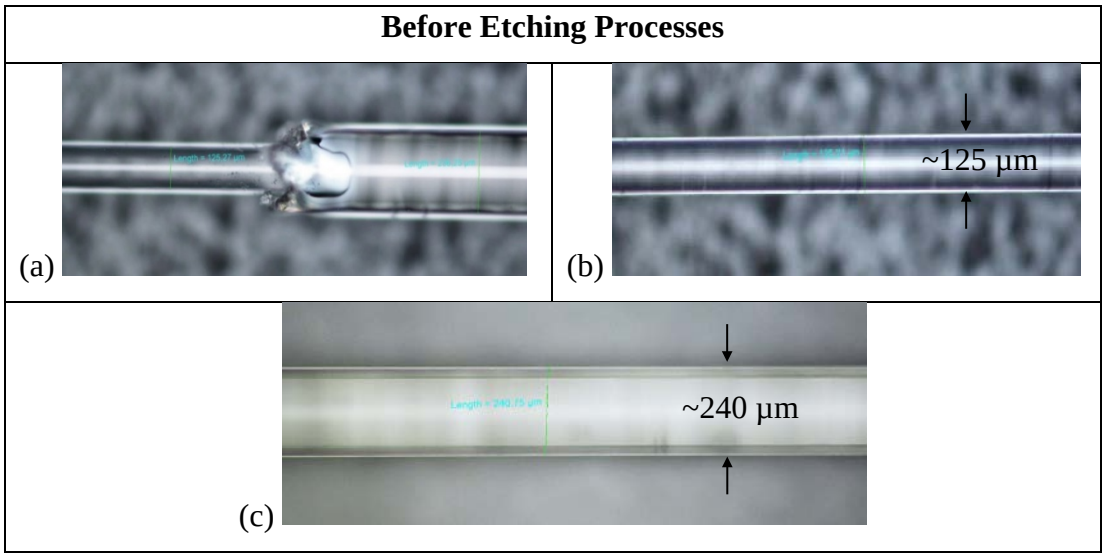

Figure 5.1. (a) SMF28 window stripping, (b) Stripped part of SMF28 (fiber diameter= ~125 µm), (c) Protective coating of the fiber (fiber diameter= ~240 µm).

5.2.1.1. Method 1

Method-1: Immersing the fiber into the HF bath (5 ml 40% HF Solution)

Determined Etch Rate: ~2.1 µm/min

In this method fibers were immersed in 5 ml 40% HF bath. After different period of times (45 and 50 minutes), HF solution was removed from the fibers' surfaces and the etched regions of the fibers were rinsed with deionized water for a few minutes. Etch rate was determined as 2.1 µm/min. The images were taken with the optical microscope (see Figure 5.3).

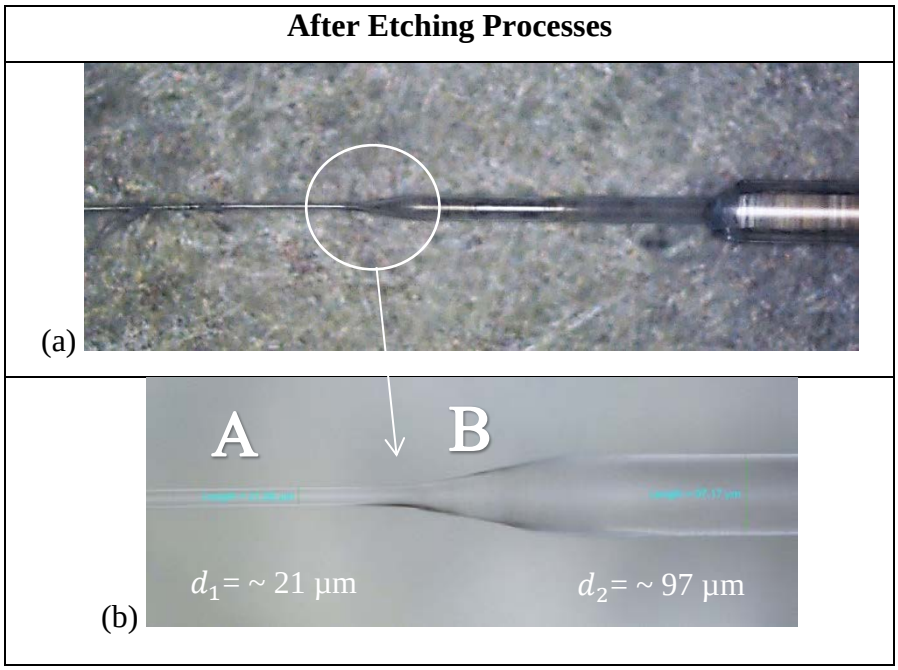

Figure 5.2. METHOD-1: (a) After wet etching and (b) magnified image (remaining diameters: ~21 µm and ~97 µm).

As shown in Figure 5.2, different parts of the fiber have different etching rates, due to the concentration gradient because of the HF acid vapor diffusion. The lower amount of acids leads to a lower etching rate. Thus, the etching rate of the middle of the stripped part of the fiber (where the HF is dropped) is much faster than that of near of the coating part. Therefore, while the etched part A looks like a filament in shape, part B is trapezoidal (see Figure 5.2 (b)).

Figure 5.3. METHOD-1: After 50-minutes wet etching process (remaining dimeter: ~19-20 µm).

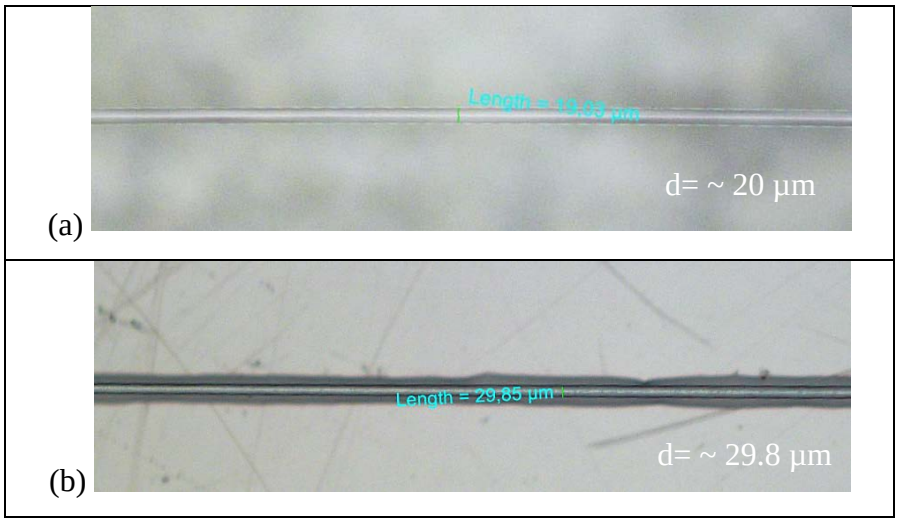

Figure 5.4. METHOD-1: (a) After 50-minutes wet etching process (remaining dimeter: ~19-20 µm), (b) after 45-minutes wet etching process (remaining dimeter: 29.85 µm).

5.2.1.2. Method 2

Method-2: Dropping HF to the bare part of the fiber (1 ml – 20 drops 40% HF)

Determined Etch Rate: ~1.1 µm/min

In this method fibers were fixed slightly on a natural polypropylene (PP) material and dropping HF (1 ml – 20 drops) to the bare part of the fiber. After different durations (55, 80, 90 and 95 minutes), HF solution was removed and the etched regions were rinsed with deionized water for a few minutes. Determined etch rate was nearly 1.1 µm/min. In this process, the diameter reduction was limited to about 20 µm.

The images of the fibers were taken with the optical microscope (cf. Figure 5.5) and SEM (cf. Figure 5.6).

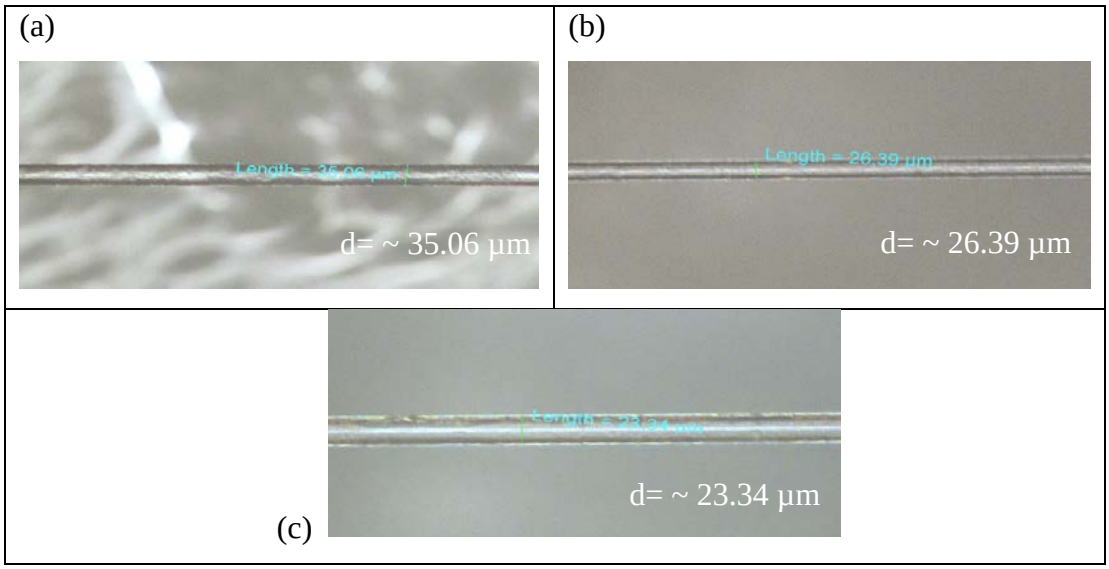

Figure 5.5. METHOD-2: (a) After 80-minutes wet etching process (remaining diameter: ~35.06 µm), (b) After 90-minutes wet etching process (remaining diameter: ~26.39 µm, (c) After 95-minutes wet etching process (remaining diameter: ~23.34 µm).

SEM and optical microscope images of the fiber was etched during 55 minutes are given in Figure 5.6 (for the SEM image, the fiber was broken manually from the middle of the thinned part).

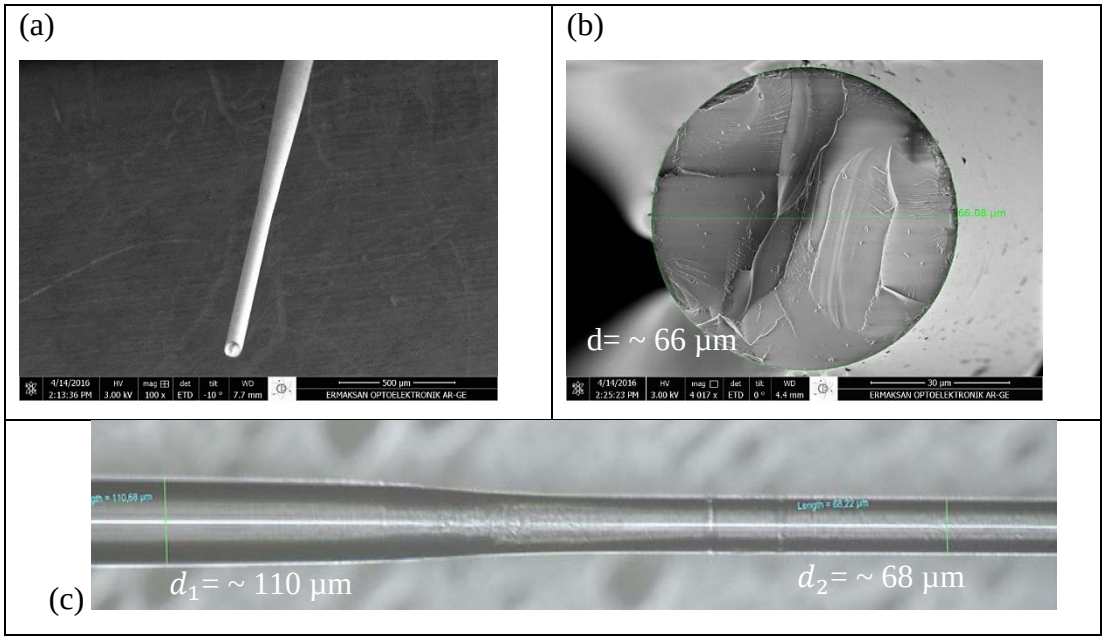

Figure 5.6. METHOD-2: (a) SEM image of the fiber after 55 minutes-etching process, (b) SEM image of the fiber end (remaining diameter: ~66 µm), (c) Optical microscope image of the same fiber.

5.2.1.3. Method 3

Method-3: Dip etching method (immersing the cleaved end of the fiber perpendicularly into 5-ml dropper filled with 40% HF solution)

Determined Etch Rate*:* 2.1 µm/min

In this method, the fiber was stripped from the cleaved end and vertically immersed into a 5-ml dropper filled with 40% HF solution. After being waited at different times (35 and 55 minutes), the same tip was immersed in a beaker filled with deionized water and rinsed for a few minutes. Determined etch rate was same as the Method-1 (2.1 µm/min). This method can be used for making fiber sensor tips.

In order to compare the ends of the fibers (after stripping the coating) SEM-images of both manually broken and device-cleaved fiber were taken before the etching process. As expected, it was seen that the device-cleaved fiber was smoother, hence more suitable for the etching process (cf. Figure 5.7. (a) and (b)).

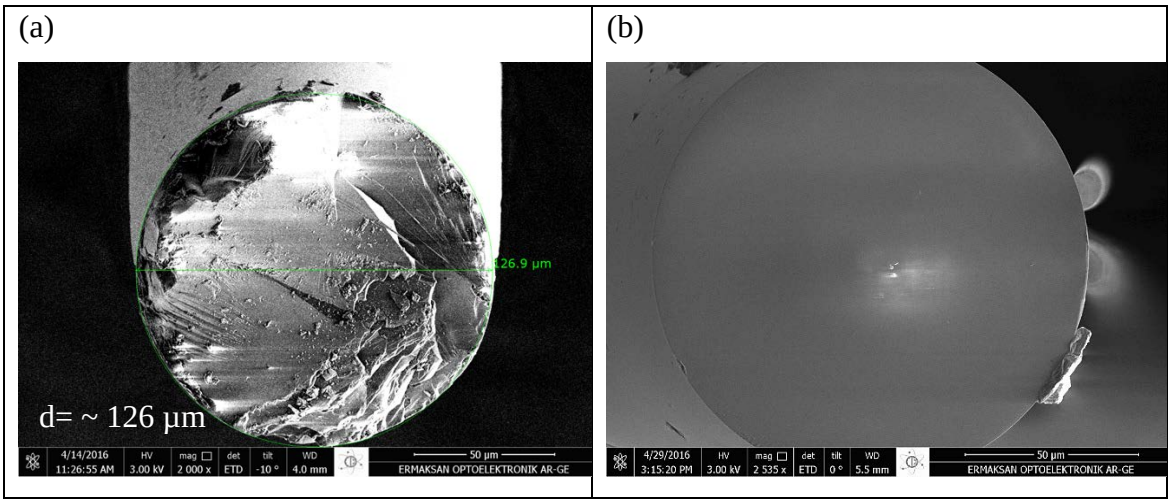

Figure 5.7. (a) SEM image of the fiber before etching (hand-cleaved end), (b) SEM image of the fiber before etching (fiber was cleaved with an automatic fiber cleaver).

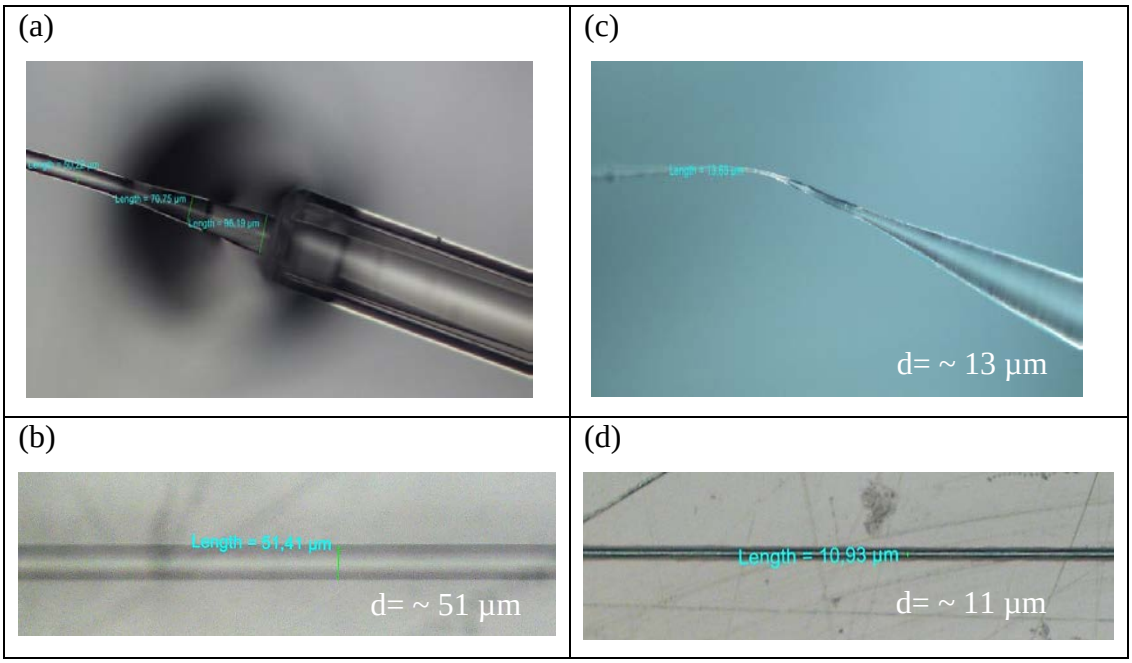

Figure 5.8. METHOD-3: (a) and (b) After 35-minutes wet etching process, (remaining diameter: ~51 µm, (c) and (d) After 55-minutes wet etching process, (remaining diameter: ~11 µm).

During the etching processes, fibers show three different stages of variation. First, there is a filament at the end of the fiber (or around the middle of the window stripped part). Then, it gets thinner and thinner, until it disappears. After that, the width of the fiber end gradually decreases until the fiber becomes a cone (Figure 5.9). Such an etching process may be referred to as *over-etching* for our applications.

In addition to over-etching, in some applications the fiber may break during or after thinning processes. The weight of the etching acid or the rinsing water, inclined or too tight fixing of the fiber, and air flow of the wet bench's fan are the effects that can create tension on the fibers. For such small diameters, the tensions applied to the fiber with these kinds of effects are enough to break the fiber from the thinned section.

The images of the broken or the over etched fibers taken with the optical microscope and SEM are as follows:

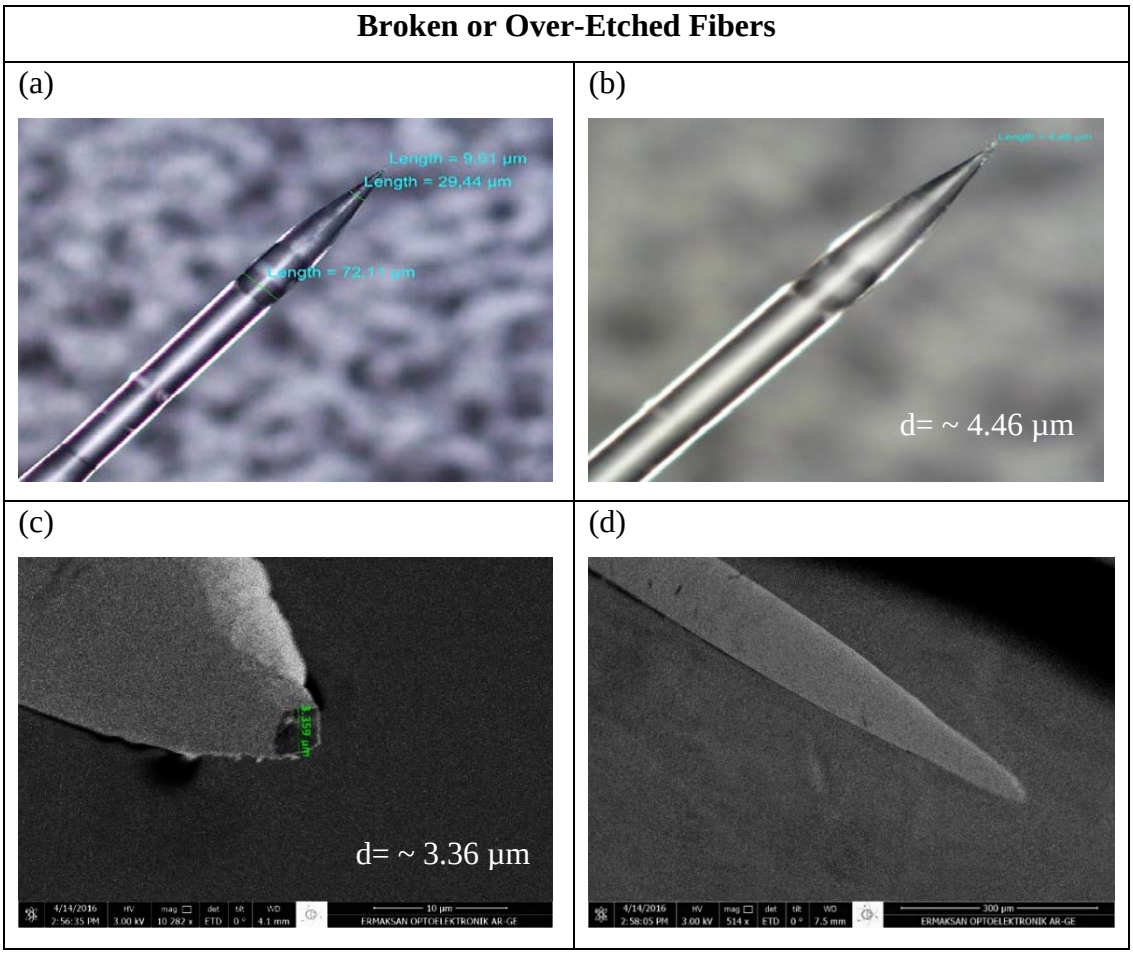

Figure 5.9. (a) Conic fiber tip (~60 minutes later with METHOD-1), (b) microscope image of the broken fiber, (c) and (d) SEM images of the broken fiber.

5.3. Conclusions

In this section, different methods had been tried for the etching process, which is one of the methods used to increase the sensitivity of the LFPG-based refractometer, and as a result, the etching rates of the silica fibers were determined using the test fibers.

As more fluids can be filled into the bath (in order to prevent the acid from spreading due to fan's air flow and to ensure that there are no dry spots that the acid cannot reach), METHOD-1 may be preferred instead of METHOD-2. However, since too much ratios of HF increases etch rates, diluted or buffered HF solutions can be prepared with DI water or NH4F, respectively, for a more controlled etching. Fibers should be kept in water overnight after the etching process.

Depending on the amount of the desired sensitivity enhancement, the LPFGs may be subjected to a few microns of etching or may be thinned up to DTP appearance in their spectrum.

In the framework of this thesis, the refractive index measurements were not tried with these etched FBGs and SMFs. Because, to get an external refractive index sensitivity, the FBG written fibers' diameter must be etched to under 20 μm (especially to achieve higher RI sensitivity fiber should be etched up to the core or more, cf. Table 5.3). When the diameter of the fiber is lower than 20 μm, the fiber gets very fragile and vulnerable and transporting it without breaking over long distances becomes a challenging issue. Therefore, to compensate the reduction in the mechanical integrity and robustness of the device, careful packaging and transporting have a critical role in here. As mentioned before, the purpose of our preliminary trials was to determine the etch rate of the silica fiber and gain expertise for the future work.

In contrast to FBGs, LPFGs can be used without etching the cladding for measuring the external mediums' refractive indices. And in order to enhance the sensitivity of the sensor, too much thinning is not required. However, due to very limited number of LPFG in our disposition, no etching procedures have been realized.

CHAPTER 6

CONCLUSIONS

In the last two decades, fiber based refractive index sensors have attracted a growing interest due to their ability to perform environmental analysis, to determine quality and safety standards in different areas (e.g. food, and petroleum industry), and also their capability in the development of label free and high-sensitive sensors in the biomedical area.

In the framework of this thesis, two intrinsic fiber-based refractive index sensors with different modulation techniques (intensity and wavelength modulation) were investigated; namely the long-period fiber grating (LPFG) and Fresnel reflection sensors. The former has been chosen due to its capability to offer very good resolution values (up to $10^{-6} - 10^{-8}$, that is critical for various biomedical applications); while the latter provides a simple and robust solution for the remote monitoring applications

First of all, we reported a complete state-of-the-art of different types of fiber-based refractive index sensors. The performance characteristics and application areas have been presented with the aid of tables.

Then, the complete mathematical demonstration of the LPFG functionality has been provided. The mathematical modeling starts with the solutions of Maxwell equations in cylindrical coordinates. Characteristic equations (also called eigenvalue equations, or dispersion relation) were found for different modes (TE, TM and hybrid modes) by applying the boundary conditions for a light propagated in a step index fiber. To simplify the characteristic equations, *the weakly guiding approximation* has been implemented and linearly polarized modes (LP modes) were defined. By using the general coupled mode theory and the coupled-mode equations, the set of differential equations describing mode couplings in single mode long period fiber gratings (co-directional coupling between the fundamental core mode and the cladding modes) were defined, and the transmission formula was found to simulate the spectrum of the LPFG by solving the couple mode equations in the appropriate boundary conditions.

Two-layer model was used for the simulation to avoid complex derivations in the *three-layer model*, hence the effect of the core is neglected at the cladding ambient

interface when determining the cladding effective refractive index. In the simulations (implemented in MATLAB), the propagation constants and the corresponding effective refractive indices of the core and the cladding modes, the coupling coefficients and the detuning parameters were calculated, and the theoretical transmission spectrums were plotted for different external refractive indices (at 1550 nm) for an individual LPFG. The simulations were limited in the range where the external refractive index is smaller than the refractive index of the cladding.

Simulated results were experimentally verified for both techniques (LPFG and Fresnel). Our calculations were validated by a fairly good agreement with the experimental results. For the experimental work, glycerin-distilled water solutions (10% to 100%) and glucose-distilled water solutions (10% to 50%) were prepared at different concentrations. The refractive indices of these solutions were measured with a RE50 (digital refractometer at 589.3 nm). The absence of high-precision experimental equipment prevented the preparation of solutions at the aimed concentration values. Therefore, the real concentration values of the solutions were found from the refractive indices of water and pure glycerin at 589 nm. The reference refractive indices were then converted into values at 1550 nm.

In the LPFG-based sensor, a broadband light source was used as light source and OSA was used as interrogation unit. The prepared solutions were dropped to the sensing part of the fiber which the LPFG was written and the transmission spectrums were recorded with a software controlled on a PC. Resonant wavelength shifts relative to the reference spectrum (LPFG at air) were determined from the zero-cross point, after the smoothing operation was applied to the transmission spectrums and derivatives of the curve were taken. The characteristic (calibration) curve (wavelength shifts versus refractive index change) of the sensor was found and plotted for the reference values (at 589 nm). Long-term repeatability measurements showed a very consistent result.

The refractive index values found from the theoretical and the experimental calibration curves were compatible with the values that were measured by the RE50 digital refractometer. The sensitivity of 217.4 nm/RIU (in the RI range of 1.44291-1.45441) was demonstrated for the LPFG-based RI sensor.

The second fiber sensor was Fresnel reflection-based (intensity modulated). Compared to the LPFG based RI-sensor, Fresnel-reflection based RI-sensor was straightforward and practical. The Fresnel reflection-based RI sensor does not require complex mode analysis for simulation.

In the Fresnel reflection-based sensor, SMF was used as sensor tip. Conventional SMF is easy-to-reach and that reduces the cost of this sensor compared to the LPFG-based sensor which is required special fabrication techniques. LPFG-based sensors are also required high cost interrogation unit (i.e. OSA) for demodulation.

The LPFG-based sensor was demonstrated to have a better sensitivity compared to Fresnel-based sensor approach. However, it is difficult to implement LPFG sensor in some cases, for instance, when working with glucose-water solutions (sugar crystals can accumulate on the fiber) and oils (hard to clean). In order to clean these materials from the LPFG surface, it is necessary to keep the sensing part of the fiber in solvents such as alcohol or water for longer time. In the Fresnel reflection-based sensor, the SMF tip can easily be cleaved and the next measurement was realized with the new and clean tip.

Intensity-based sensors, on the other hand, are influenced by the power fluctuations of the light source (which is not a problem for LPFG). Moreover, LPFG sensor's sensitivity can be significantly improved by using various enhancement methods. These methods have been discussed in the perspectives of the thesis.

REFERENCES

Abramowitz, M. and Stegun, I.A., (1965). Handbook of mathematical functions. Dover Publications, New York.

Adams, M.J., (1981). An introduction to optical waveguides. John Wiley & Sons.

Akki J. F., Lalasangi A. S., Raikar P. U., Srinivas T., Laxmeshwar L. S., Raikar U. S., (2013). Core-cladding mode resonances of long period fiber grating in concentration sensor. IOSR J. Appl. Phys., 2278-4861. 4(3), 41-46.

Allsop, T., Reeves, R., Webb, D.J., Bennion, I., and Neal, R., (2002). A high sensitivity refractometer based upon a long period grating Mach-Zehnder interferometer. Rev. Sci. Instrum. 73(4), 1702-1705.

Allsop T, Floreani F, Jedrzejewski K P, Marques P V S, Romero R, Webb D J and Bennion I., (2006). Spectral characteristics of tapered LPG device as a sensing element for refractive index and temperature. J. Lightw. Technol. 24(2), 870–8.

Alvarez-Herrero A., Guerrero H., and Levy D., (2004). High-Sensitivity Sensor of Low Relative Humidity Based on Overlay on Side-Polished Fibers, IEEE, Sens. J., 4(1), 52-56.

Aparicio, R., Aparicio-Ruiz, R, (2000). Authentication of vegetable oils by chromatographic techniques. J. Chromatogr. A. 881(1-2), 93-104.

Asseh, A., Sandgren, S., Ahlfeldt, H., Sahlgren, B., Stubbe, R., and Edwall, G., (1998). Fiber optical Bragg grating refractometer. Fiber Integrated Opt., 17(1), 51-62.

Baek S, Jeong Y., and Lee B., (2002). Characteristics of short-period blazed fiber Bragg gratings for use as macro-bending sensors. Appl. Opt., 41(4), 631–636.

Baeten, V., Meurens, M., Morales, M. T., Aparicio, R., (1996). Detection of virgin olive oil adulteration by Fourier transform Raman spectroscopy. J. Agric. Food Chem., 44(8), 2225-2230.

Baeten, V., Dardenne, P., Aparicio, R., (2001). Interpretation of Fourier transform Raman spectra of the unsaponifiable matter in a selection of edible oils. J. Agric. Food Chem., 49(11), 5098-5107.

Baliyan A., Sital S., Tiwari U., Gupta R., Sharma E. K., (2016). Long period fiber grating based sensor for the detection of triacylglycerides, Biosens. Bioelectron., 79(15), 693-700.

Bandara A. B., Zuo Z., Ramachandran S., Ritter A., Heflin J. R., Inzana T. J., (2015) Detection of methicillin-resistant staphylococci by biosensor assay consisting of nanoscale films on optical fiber long-period gratings. Biosens. Bioelectron., 70(15), 433-440.

Basgumus A., Durak F. E., Altuncu A., and Yilmaz G., (2015). A universal and stable all-fiber refractive index sensor system, IEEE Photon. Technol. Lett., 28(2), 171-174.

Beyer, W. H. (1987). Standard Mathematical Tables, (28th Ed.). Boca Raton, FL: CRC Press.

Bhatia V., (1999). Applications of long-period gratings to single and multi-parameter sensing. Opt. Express, 4(11), 457-466.

Bhatia V. and Vengsarkar A. M., (1996). Optical fiber long-period grating sensors. Opt. Lett., 21(9), 692–694.

Buck, J.A. (1995). Fundamentals of optical fibres. New York: John Wiley & Sons.

Butov O.V., Golant K. M., Tomashuk A. L., van Stralen M. J. N., and Breuls A. H. E., (2002). Refractive index dispersion of doped silica for fiber optics. Opt. Comm., 213, 301–308.

Brenci M., Conforti G., Mignani A. G. and Scheggi A.M., (1988). Fiber Optic Position Sensor Array. Opt. Fib. Sens., Techn. Digest Series, 2, 141-144.

Caldas P., Jorge P. A. S., Araujo F. M., Ferreira L. A., Marques M. B., Rego G., Santos J. L., (2008). Fiber modal Michelson interferometers with coherence addressing and heterodyne interrogation. Opt. Eng., 47(4), 044401(1-7).

Caucheteur C., and Mégret P., (2005). Demodulation technique for weakly tilted fiber Bragg grating refractometer. IEEE Photon. Technol. Lett., 17(12), 2703–2705.

Caucheteur C., (2007). Realization of mechanical and chemical sensors based on the fiber Bragg gratings technology, PhD thesis, Faculté polytechnique de Mons.

Caucheteur, C., Tuan G., Fu L., Bai-Ou G., Jacques A., (2016). Ultrasensitive plasmonic sensing in air using optical fibre spectral combs. Nature Comm.., 7, id. 13371.

Caucheteur C., Shevchenko Y., Shao L.-Y., Wuilpart M., and Albert J., (2011). High resolution interrogation of tilted fiber grating SPR sensors from polarization properties measurement. OSA, Opt. Express, 19(2), 1656-1664.

Chan, C.-F., Chen, C., Jafari, A., Laronche, A., Thomson, D. J., and Albert, J., (2007). Optical fiber refractometer using narrowband cladding-mode resonance shifts. Appl. Opt., 46(7), 1142-1149.

Chen H.-W., Tien C.-L., Liu W. F., Lin S.-W., (2007). The Measurement of Liquid Refractive Index by D-shaped Fiber Bragg Grating. 2007 IEEE/LEOS International Conference on Optical MEMS and Nanophotonics, Hualien, 119-120.

Chen C.-H., Yeh B.-K., Tang J.-L., Wu W.-T., (2013). Fabrication Quality Analysis of a Fiber Optic Refractive Index Sensor Created by CO2 Laser Machining. J. Sens., 13, 4067-4087.

Chen X., Zhou K., Zhang L., Bennion I., Optical Chemsensors Utilizing Long-Period Fiber Gratings UV-Inscribed in D-Fiber With Enhanced Sensitivity Through Cladding Etching, (2004). IEEE, Photon. Technol. Lett., 16(5), 1352-1354.

Chen J.-H., Huang X.-G., He W.-X., and Tao J., (2011). A parallel-multipoint fiber-optic temperature sensor based on Fresnel reflection. Opt. Laser Technol., 43, 1424–1427.

Cherif K., Hleli S., Abdelghani A., Jaffrezic-Renault N., Matejec V., (2002). Chemical detection in liquid media with a refractometric sensor based on a multimode optical fibre, Sens., 2(1424-8220),195-204.

Cherin, A.H. (1983). An introduction to optical fibres. New York: McGraw-Hill.

Chiang K., Liu Y., Ng M., and Dong X., (2000). Analysis of etched long-period fiber grating and its response to external refractive index. Electron. Lett., 36, 966 –967.

Chryssis, A. N., Lee, S. M., Lee, S. B., Saini, S. S., and Dagenais, M., (2005). High sensitivity evanescent field fiber Bragg grating sensor. Photon. Technol. Lett., IEEE, 17(6), 1253-1255.

Coelho L., Kobelke J., Schuster K., Santos J. L. and Frazão O., (2011). Optical refractometer based on multimode interference in a pure silica tube. Opt. Eng., 50(10), 100504-100504-3.

Coelho, L., Kobelke, J., Schuster, K., Frazão, O. (2012). Multimode interference in outer cladding large-core, air-clad photonic crystal fiber. Microw. Opt. Technol. Lett., 54, 1009–1011.

Coelho L., Viegas D., Santos J. L., de Almeida J.M.M.M., (2014). Enhanced refractive index sensing characteristics of optical fibre long period grating coated with titanium dioxide thin films. Sens. Actuators B Chem., 202(0925-4005), 929-934.

Coelho L., Viegas D., Santos J. L., de Almeida J.M.M.M., (2016). Characterization of zinc oxide coated optical fiber long period gratings with improved refractive index sensing properties. Sens. Actuators B Chem., 223(0925-4005), 45-51.

Corres J.M., Del Villar I., Matias I. R., Arregui F. J., (2008). Two-layer nanocoatings in long period fiber gratings for improved sensitivity of humidity sensors. IEEE Trans. Nanotechnol., 7, 394–400.

Cooper, P.R., (1983). Refractive-index measurements of liquids used in conjunction with optical fibres. Appl. Opt., 22, 3070–3072.

Conforti G., Brenci M., Mencaglia A. and Mignani A.G., (1989). Fiber optic vibration sensor for remote monitoring in high power electric machines. Appl. Opt., 28(23), 5158-61.

Cusano A., Iadicicco A., Pilla P., Contessa L., Campopiano S., Cutolo A., and Giordano M., (2005). Cladding mode re-organization in high-refractive-index-coated long-period gratings: effects on the refractive-index sensitivity. Opt. Lett., 30(19), 2536–2538.

Davies, A. N., McIntyre, P., Morgan, E., (2000). Study of the use of molecular spectroscopy for the authentication of extra virgin olive oils. part I: Fourier transform Raman spectroscopy. Appl. Spectrosc., 54, 1864-1867.

Del Villar I., Cruz J. L., Socorro A. B., Corres J. M., and Matias I. R., (2016). Sensitivity optimization with cladding etched long period fiber gratings at the dispersion turning point. Opt. Express, 24(16), 17680–17685.

Del Villar I., Achaerandio M., Matías I. R., and Arregui F. J., (2005). Deposition of overlays by electrostatic self-assembly in long-period fiber gratings. Opt. Lett., 30(7), 720–722.

Del Villar I., Matías I., Arregui F., and Lalanne P., (2005). Optimization of sensitivity in Long Period Fiber Gratings with overlay deposition. Opt. Express., 13(1), 56–69. (2).

Del Villar I., (2015). Ultrahigh-sensitivity sensors based on thin-film coated long period gratings with reduced diameter, in transition mode and near the dispersion turning point. Opt. Express, 23(7), 8389–8398.

Díaz-Herrera, N., González-Cano, A., Viegas, D., Santos, J.L., Navarrete, M., (2010). Refractive index sensing of aqueous media based on plasmonic resonance in tapered optical fibres operating in the 1.5 μm region. Sens. Actuators B Chem., 146, 195–198.

Díaz-Herrera, N., Viegas, D., Jorge, P., Araújo, F.M., Santos, J.L., Navarrete, M.C., González-Cano, A. (2010). Fiber-optic SPR sensor with a FBG interrogation scheme for readout enhancement. Sens. Actuators B Chem., 144, 226–231. (2).

Eggleton B. G., Krug P. A., Poladian L., and Ouellette F., (1994). Long periodic superstructure Bragg gratings in optical fibres. Electron. Lett., 30(19), 1620–1622.

Enriquez D. A. C., Cruz A. R., Giraldi M. T. M. R., (2012). Hybrid FBG–LPG sensor for surrounding refractive index and temperature simultaneous discrimination. Opt. Laser Technol., 44, 981–986.

Erdogan, T., (1997). Fiber grating spectra. J. Lightw. Technol., 15(8), 1277-1294.

Erdogan, T., (1997). Cladding-mode resonances in short- and long-period fiber grating filters. J. Opt. Soc. Am. A,14(8), 1760-1773. (2).

Erdogan, T., (2000). Cladding-mode resonances in short- and long-period fiber grating filters: errata. J. Opt. Soc. Am. A, 17(11), 2113.

Falco, L., Spescha, G., Roth, P., Parriaux, O., (1986). Non-ambiguous evanescent-wave fibre refractive index and temperature sensor. Optica Acta, 33(12), 1563-70.

Falate, R., Frazão, O., Rego, G., Fabris, J.L., Santos, J.L., (2006). Refractometric Sensor based on a phase-shifted long-period fiber grating. Appl. Opt., 45, 5066–5072.

Frazão, O., Martynkien, T., Baptista, J.M., Santos, J.L., Urbanczyk, W., Wojcik, J., (2009). Optical refractometer based on a birefringent Bragg grating written in an H-shape fiber. Opt. Lett., 34, 76–78.

Frazão, O., Baptista, J.M., Santos, J.L., Kobelke, J., Schuster, K., (2009). Refractive index tip sensor based on Fabry-Perot cavities formed by a suspended core fibre. J. Eur. Opti. Soc.-Rapid Publ., 4, 09041. (2).

Gastón A., Lozano I., Sevilla J., (2006). A Novel Approach to On Line Oil Quality Sensing Through Side- Polished Optical Fiber. Instrumentation and Measurement Technology Conference, Sorrento Italy.

Garg R. and Thyagarajan K., (2012). Superimposed long period fiber grating-based refractive index sensor. J. Mod. Opt., 59(21), 1856-1862.

Garg R., Tripathi S. M., Thyagarajan K., Bock W. J., (2013). Long period fiber grating based temperature-compensated high performance sensor for bio-chemical sensing applications. Sens. Actuators B, 176, 1121– 1127.

Ghetia S., Gajjar R., and Trivedi P., (2013). Classification of Fiber Optical Sensors. Int. J. Electron. Commun. Comput. (IJECCT), 3(4), 442-445.

Govindan G., Raj S. G., Sastikumar D., (2009). Measurement of refractive index of liquids using fibre optic displacement sensors. Marsland Press: J. Am. Sci., 5(2), 13-17.

Gouveia, C., Jorge, P.A.S., Baptista, J.M., Frazão, O., (2012). Fabry-Pérot cavity based on a high-birefringent fiber Bragg grating for refractive index and temperature measurement. IEEE Sens. J., 12, 17–21.

Gu, Z., Lan, J., Gao, K. (2015). Characteristics of plasmon coupling mode in SPR based LPFG. In Proceedings of the 2015 International Conference on Numerical Simulation of Optoelectronic Devices (NUSOD), Taipei, Taiwan, pp. 55–56.

Gu Z. and Xu Y., (2007). Design optimization of a long-period grating with sol-gel coating for a gas sensor. Meas. Sci. Technol. 18(11), 3530–3536.

Guo T., Chen C., Laronche A., and Albert J., (2008). Power-referenced and temperature-calibrated optical fiber refractometer. IEEE Photon. Technol. Lett., 20(8), 635–637.

Hill K. O., Malo B, Bilodeau F., Johnson D.C., and Albert J., (1993). Bragg gratings fabricated in monomode photosensitive optical fiber by UV exposure through a phase mask. Appl. Phys. Lett., 62, 1035.

Hu H. F., Deng Z. Q., Zhao Y., Li J. and Wang Q., (2015). Sensing Properties of Long Period Fiber Grating Coated by Silver Film. IEEE Photon. Technol. Lett., 27(1), pp. 46-49.

Hromadka J., Tokay B., James S., Tatam R. P., Korposh S., (2015). Optical fibre long period grating gas sensor modified with metal organic framework thin films. Sens. Actuators B Chem., 221 (0925-4005), 891-899.

Hochreiner H., Cada M., Wentzell P. D., (2008). Modeling the Response of a Long-Period Fiber Grating to Ambient Refractive Index Change in Chemical Sensing Applications. J. Lightw. Technol., 26(13), 1986-1992.

Huang, J.F., He, Y.J., and Lo, Y.L., (2006). Spectrum analysis for high-order cladding modes based on long-period fiber gratings. Opt. Eng., 45(9), 095001-(1-7).

Huy M. C. P., Laffont G., Dewynter V., Huy P. F., (2006). Tilted Fiber Bragg Grating photowritten in Microstructured Optical Fiber for improved refractive index measurement. Opt. Express, 14(22), 10359-10370.

Hou, R., Ghassemlooy, Z., Hassan, A., Lu, C. and Dowker, K.P., (2001). Modelling of long-period fibre grating response to refractive index higher than that of cladding. Meas. Sci. Technol., 12(10), 1709-1713.

Iezzi V. L., Boisvert J.-S., Loranger S., and Kashyap R., (2016). 3D printed long period gratings for optical fibers. Opt. Lett., 41, 1865-1868.

Iadicicco, A., Campopiano, S., Cutolo, A., Giordano, M., Cusano, A., (2005). Refractive index sensor based on microstructured fiber Bragg grating. Photon. Technol. Lett., 17(6), 1250-2.

Iadicicco A, Campopiano S, Giordano M and Cusano A., (2007). Spectral behavior in thinned long period gratings: effects of fiber diameter on refractive index sensitivity. Appl. Opt., 46 (28), 6945–52.

Iadicicco A., Campopiano S., Cutolo A., Korwin-Pawlowski M. L., Bock W. J. and Cusano A., (2008). Refractive index sensitivity in thinned UV and arc induced long-period gratings: a comparative study. Int. J. Smart Sens. Intell. Syst., 1(2), 354-369.

James, S.W. and Tatam, R.P., (2003). Optical fibre long-period grating sensors: characteristics and applications. Meas. Sci. Technol., 14(5), 49-61.

Jason J., (2008). Theory and Applications of Coupling Based Intensity Modulated Fibre-Optic Sensors, Mid Sweden University Licentiate Thesis.

Jesus, C., Caldas, P., Frazão, O., Santos, J. L., Jorge, P. A. S. and Baptista, J. M., (2009). Simultaneous Measurement of Refractive Index and Temperature Using a Hybrid Fiber Bragg Grating/Long-Period Fiber Grating Configuration. Fib. Integr. Opt., 28(6), 440-449.

Ji W. B., Tjin S. C., Lin B., and Ng C. L., (2013). Highly Sensitive Refractive Index Sensor Based on Adiabatically Tapered Microfiber Long Period Gratings. Sens., 13(10), 14055–14063.

Jones W. B., (1995). Introduction to Optical Fiber Communications Systems, Oxford University Press, ISBN: 9780195107265.

Kang Y., (2002). Calculations and Measurements of Raman Gain Coefficients of Different Fiber Types, MSc Thesis, Virginia Polytechnic Institute and State University.

Kanka J., (2013). Design of turn-around-point long-period gratings in a photonic crystal fiber for refractometry of gases. Sens. Actuators B Chem., 182, 16–24.

Kashyap, R., (1999). Fiber Bragg Gratings. San Diego: Academic Press.

Kawasaki Y. f. D. C. J. B.S., Hill K.O., (1978). Narrow-band bragg reflectors in optical fibers. Opt. Letters, 3, 66–68.

Keck, D. B., (1976). Fundamentals in Optical Fiber Communications, M. K. Bamoski (ed.). New York: Academic Press, Chapter 1.

Keiser, G. (2000). Optical Fibre Communications. (3rd Ed.). Boston: McGraw-Hill.

Kersey A. D., Davis M. A., Patrick H. J., LeBlanc M., Koo K. P, Askins C. G., Putnam M. A., and Friebele E. J., (1997). Fibre grating sensors. J. Lightw. Technol., 15(8), 1442–1463.

Kim C.-B., Su C.-B., (2004). Measurement of the refractive index of liquids at 1.3 and 1.5 micron using a fibre optic Fresnel ratio meter, Meas. Sci. Technol., 15, 1683–1686.

Kim K. T., Song H. S., Mah J. P., Hong K. B., Im K., Baik S.-J., and Yoon Y.-I., (2017). Hydrogen Sensor Based on Palladium Coated Side-Polished Single-Mode Fiber. IEEE, Sens. J., 7(12), 1767-1771.

Klantsataya E., Jia P., Ebendorff-Heidepriem H., Monro T. M., François A., (2017). Plasmonic Fiber Optic Refractometric Sensors: From Conventional Architectures to Recent Design Trends. Sens., 17(1), 12.

Koyamada Y., (2001). Numerical analysis of core-mode to radiation-mode coupling inlong-period fiber gratings. IEEE Photon. Technol. Lett., 13, 308–310.

Kogelnik H., (1990). Theory of optical waveguides in Guided-Wave Optoelectronics, T. Tamir, Ed., New York: Springer-Verlag.

Kumar, A., Subrahmanyam, T. V. B., Sharma, A. D., Thyagarajan, K., Pal, B. P., Goyal, I. C., (1984). Novel refractometer using a tapered optical fibre. Electron. Lett., 20, 534–535.

Kumar J., Mahakud R., Kumbhkar U., Prakash O., Dixit S. K., Nakhe S. V., (2015). Analysis of experimental results on the adulteration measurement by an etched fiber Bragg grating sensor. Optik – Int. J. Light Electron Opt., 126(24), 5698-5702.

Laffont G., and Ferdinand P., (2001). Tilted short-period fiber-Bragg-grating induced coupling to cladding modes for accurate refractometry. Meas. Sci. Technol., 12(7), 765–770.

Lee, B. H., Liu, Y., Lee, S.B., Choi, S.S., Jang, J.N., (1997). Displacements of the resonant peaks of a long-period fiber grating induced by a change of ambient refractive index. Opt. Lett., 22(23), 1769-1771.

Lee J., Chen Q., Zhang Q., Reichard K., Ditto D., Mazurowski J., Hackert M., and Yin S., (2007). Enhancing the tuning range of a single resonant band LPG while maintaining the resonant peak depth by using an optimized high index ITO overlay. Appl. Opt., 46(28), 6984–6989.

Li, Q.-S., Zhang, X.-L., Shi, J.-G., Xiang, D., Zheng, L., Yang, Y., Dong, W.-F., et. al., (2016). An Ultrasensitive Long-Period Fiber Grating-Based Refractive Index Sensor with Long Wavelengths. Sens. (Basel, Switzerland), 16(12), 2205.

Li L., Xia L., Wuang Y., Ran Y., Yang C., and Liu D., (2012). Novel NCF-FBG Interferometer for Simultaneous Measurement of Refractive Index and Temperature. IEEE, Photon. Technol. Lett., 24(24), 2268-2271.

Li, H. and Xie S., (1996). Measurement method of the refractive index of bio-tissue by total internal reflection. App. Opt., 35, 1793-5.

Liang X. J., Liu A. Q., Lim C. S., Ayi T. C. & Yap P. H., (2007). Determining refractive index of single living cell using an integrated microchip. Sens. Actuators A Phys., 133, 349-54.

Liang W., Huang Y., Xu Y., Lee R. K., and Yariv A., (2005). Highly sensitive fiber Bragg grating refractive index sensors. Appl. Phys. Lett., 86, 151122.

Libish T. M., Linesh J., Biswas P., Bandyopadhyay S., Dasgupta K., Radhakrishnan P., (2010). Fiber Optic Long Period Grating Based Sensor for Coconut Oil Adulteration Detection. Sens. Transd. J., 114(3), 102-111.

Libish T. M., Linesh C. J., Bobby M. C., Biswas P., Bandyopadhyay S., Dasgupta K., Radhakrishnan P., (2011). Fiber Optic Sensor For The Adulteration Detection Of Edible Oils. Optoelectron. Adv. Materials, Rapid Comm., 5(1), 68 – 72.

Linesh J., Libish T. M., Bobby M. C., Radhakrishnan P. and Nampoori V. P. N., (2011). Periodically Tapered LPFG for Ethanol Concentration Detection in Ethanol-Gasoline Blend. Sens. Transd. J., 125(2), 205-212.

Liu Y., and Qu S., (2013). Femtosecond laser pulses induced ultra-long-period fiber gratings for simultaneous measurement of high temperature and refractive index. Optik, 124, 1303– 1306.

Liu L., Gong Y., Wu Y., Zhao T., Wu H.-J., Rao Y.-J., (2012). Spatial Frequency Multiplexing of Fiber-Optic Interferometric Refractive Index Sensors Based on Graded-Index Multimode Fibers. Sens., 12, 12377-12385.

Luo B.-b., Zhao M.-f., Zhou X.-j, Shi S.-h., Han X., (2012). Mechanism of refractive index distribution measurement based on etched fiber Bragg grating. Proc. SPIE 8421, OFS2012 22nd International Conference on Optical Fiber Sensors.

Malo, B., Hill, K. O., Bilodeau, F., Johnson, D. C., Albert, J., (1993). Point-by-point fabrication of micro-Bragg gratings in photosensitive fiber using single excimer pulse refractive index modification techniques. Electron. Lett., 29, 1668-9.

Marcuse, D., Gloge, D., Marcatili, E.A., (1979). Guiding properties of fibres. In Miller, S.E., Chynoweth, A.G. (Eds.). Optical fiber telecommunications. New York: Academic Press.

Marcuse D., (1991). Theory of Dielectric Optical Waveguides. New York: Academic.

Martinez-Rios A., Monzon-Hernandez D. and Torres-Gomez I., (2010). Highly sensitive cladding-etched arc-induced long-period fiber gratings for refractive index sensing. Opt. Commun., 283 958–62.

Marques L., Hernandez F. U., James S. W., Morgan S. P., Clark M., Tatam R. P., Korposh S., (2016). Highly sensitive optical fibre long period grating biosensor anchored with silica core gold shell nanoparticles. Biosens. Bioelectron., 75(15), 222-231.

Mathews, J., Walker, R. L., (1970). Mathematical methods of physics, (2nd Ed.). Benjamin, New York.

Mathews C. B., Libish T. M., Kaushalkumar B., Vivek V., Prabhu R., and Radhakrishnan P., (2016). A fiber optic biosensor for the detection of cholesterol levels based on chitosan coated long period grating. Optoelectron. Lett., 12(1), 23-26.

Mathews C. B., Libish T.M, Linesh J., Biswas P., Bandyopadhyay S., Dasgupta K., Radhakrishnan P., (2012). A Long Period Grating based biosensor for the detection and estimation of cholesterol. International Conference on Fiber Optics and Photonics (PHOTONICS), Chennai, pp. 1-3.

Mechery S. J., (2000). Evanescent Wave Fibre Optic Sensors: Design, Fabrication and Characterization. PhD Thesis. Cochin University of Science & Technology.

Meltz W. G., Morey W.W., (1989). Formation of bragg grating in optical fibers by a transverse holographic method. Opt., 14, 823–825.

Mendez A., (2011). Medical Applications of Fibre-optics: Optical Fibre Sees Growth as Medical Sensors. Las. Focus World, 47(1), 91.

Mishra, V., Jain, S. C., Singh, N., Poddar, G. C., & Kapur, P., (2008). Fuel adulteration detection using long period fiber grating sensor technology. J. Scient. Indust. Research (JSIR), 46(2), 106-110.

Monzón-Hernández D., Villatoro, J., Luna-Moreno, D., (2005). Miniature optical fiber refractometer using cladded multimode tapered fiber tips. Sens. Actuators B 110(1), 36-40.

Morey, W. W., Ball, G. A. and Meltz, G., (1994). Photoinduced Bragg gratings in optical fibers. Optics and Photonics News, Opt. Soc. Am., 5(2), 8-14.

Mou C., Yan Z., Zhou K. and Zhang L., (2014). Optical Fibre Sensors Based on UV Inscribed Excessively Tilted Fibre Grating. Optical Sensors - New Developments and Practical Applications, Dr Moh. Yasin (Ed.), InTech, DOI: 10.5772/57146.

Myśliwiec M., Grochowski J., Krogulski K., Mikulic P., Bock W. J., Śmietana M., (2013). Effect of Wet Etching of Arc-Induced Long-Period Gratings on Their Refractive Index Sensitivity. Acta Phys. Pol. A, 124, 521-524.

Nath P., (2010). Non-intrusive refractometer sensor, Pramana, J. Phys, 74(4), 661- 668.

Okamoto, K., (2006). Fundamentals of Optical Waveguides. (2nd Ed.) San Diego: Academic Press.

Othonos A., Lee X., and Measures R. M., (1994). Superimposed multiple Bragg gratings. Electron. Lett., 30(23), 1972–1974.

OTDR working principle: *http://blog.cubeoptics.com/index.php/2015/11/how-does-an-otdr-work)*

Patrick H. J., Kersey A. D. and Bucholtz F., (1998). Analysis of the response of long period fiber gratings to external index of refraction. J. Lightw. Technol., 16(9), 1606-1612.

Pereira D. A., Frazao O., and Santos J. L., (2004). Fiber Bragg grating sensing system for simultaneous measurement of salinity and temperature. Opt. Eng., 43(2), 299–304.

Pilla P., Trono C., Baldini F., Chiavaioli F., Giordano M., and Cusano A., (2012). Giant sensitivity of long period gratings in transition mode near the dispersion turning point: an integrated design approach. Opt. Lett., 37(19), 4152–4154.

Polynkin, P., Polynkin, A., Peyghambarian, N., Mansuripur, M., (2005). Evanescent field-based optical fiber sensing device for measuring the refractive index of liquids in microfluidic channels. Opt. Lett., 30(11), 1273-5.

Rahman H. A., Harun S. W., Yasin M., Ahmad H., (2011). Non-contact refractive index measurement based on fiber optic beam-through technique. Optoelectron. Adv. Materials, Rapid Commu., 5(10), 1035 – 1038.

Rego, G. M., Santos, J. L., Salgado, H. M. (2006). Refractive index measurement with long-period gratings arc-induced in pure-silica-core fibres. Opt. Commun., 259, 598–602.

Reflected & saturated peaks: http://www.thefoa.org/tech/ref/testing/test/reflectance.html

Rees N. D., James S. W., Tatam R. P., and Ashwell G. J., (2002). Optical fiber long-period gratings with Langmuir Blodgett thin-film overlays. Opt. Lett., 27(9), 686–688.

Roy S., (1999). Fiber optic sensor for determining adulteration of petrol and diesel by kerosene, Sens Actuators B Chem., 55, 212–216.

Rong Q., Qiao X., Guo T., Zhang J., Wang R., Hu M., Feng Z., Weng Y, and Ma Y., (2013). Reflective fiber-optic refractometer based on a compact Hi-Bi fiber tip. IEEE Sens. J., 13(5), 1473-1477.

Saleh, B.E.A. & Teich, M.C., (1991). Fundamentals of photonics. New York: John Wiley & Sons.

Saunders J. E., Sanders C., Chen H., and Loock H. P., (2016). Refractive indices of common solvents and solutions at 1550 nm. Appl. Opt., 55, 947-953.

Schroeder, K., Ecke, W., Mueller, R., Willsch, R., Andreev, A., (2001). A fibre Bragg grating refractometer. Meas. Sci.& Tech., 12(7), 757-64.

Schuster, T. Herschel, R., Neumann, N., Schäffer, C.G., (2012). Miniaturized long-period fiber grating assisted surface plasmon resonance sensor. J. Lightw. Technol., 30, 1003–1008.

Selvas-Aguilar R., Castillo-Guzman A., Cortez-Gonzalez L., et al., (2016). Noncontact Optical Fiber Sensor for Measuring the Refractive Index of Liquids. J. Sens., vol. 2016, Article ID 3475782, 6 pages.

Shao, L.-Y., Zhang, A. P., Liu, W.-S., Fu, H.-Y., He, S., (2007). Optical refractive-index sensor based on dual fiber-Bragg gratings interposed with a multimode-fiber taper. IEEE Photon. Technol. Lett., 19(1), 30-32.

Shen G., Jiang L., Wang S., Li B., Zhou L., Tsai H.-L., Xiao H., (2010). Thinned-cladding zeolite-coated long period fiber grating chemical sensor. Proc. SPIE 7657, 5th International Symposium on Advanced Optical Manufacturing and Testing Technologies: Design, Manufacturing, and Testing of Micro- and Nano-Optical Devices and Systems.

Shi Q., Kuhlmey B. T., (2009). Optimization of photonic bandgap fiber long period grating refractive-index sensors. Opt. Commu., 282 (24), 4723–4728.

Shu X., Zhang L., and Bennion I., (2002). Sensitivity Characteristics of Long-Period Fiber Grating. J. Lightw. Technol., 20(2), 255–266.

Silva S., Frazão O., Caldas P., Santos J. L., Araújo F. M., Ferreira L. A., (2008). Optical fibre refractometer based on a fabry-pérot interferometer. Opt. Eng., 47, 054403.

Silva S., Frazão O., Santos J.L., Malcata F.X., (2012). A reflective optical fiber refractometer based on multimode interference. Sens. Actuators B Chem., 161, 88–92.

Silva S., Santos J. L., Malcata F. X., Kobelke J., Schuster K., Frazão O., (2011). Optical refractometer based on large-core air-clad photonic crystal fibers. Opt. Lett., 36, 852–854.

Singh N., Kaler R. S., Tiwari U., Mishra V., Singh N., Kapur P., (2012). Investigation of Long Period Grating as refractive index sensor. Opt., 123, 1071–1073.

Śmietana M., Koba M., Tripathi S., Mikulic P. and Bock W. J., (2013). Improving sensing properties of the long-period gratings by reactive ion etching. Sensing Technology (ICST), 2013 Seventh International Conference on, Wellington, 665-668.

Śmietana M., Szmidt J., Korwin-Pawlowski M. L., Bock W. J., and Grabarczyk J., (2007). Application of diamond-like carbon films in optical fibre sensors based on long-period gratings. Diamond Related Materials, 16(4–7), 1374– 1377.

Śmietana M., Koba M., Mikulic P., and Bock W. J., (2014). Measurements of reactive ion etching process effect using long-period fiber gratings. Opt. Express, 22, 5986-5994.

Śmietana M., Koba M., Mikulic P., and Bock W. J., (2015). Enhancing sensitivity of long-period gratings by combined fiber etching and diamond-like carbon nano-overlay deposition. Proc. SPIE 9634, 24th International Conference on Optical Fibre Sensors, 963456.

Śmietana M., Koba M., Mikulic P., and Bock W. J., (2016). Towards refractive index sensitivity of long-period gratings at level of tens of μm per refractive index unit: fiber cladding etching and nano-coating deposition. Opt. Express, 24, 11897-11904.

Śmietana M., Koba M, Brzozowska E, Krogulski K., Nakonieczny J., Wachnicki L., Mikulic P., Godlewski M., and Bock W. J., (2015). Label-free sensitivity of long-period gratings enhanced by atomic layer deposited TiO2 nano-overlays. Opt. Express, 23, 8441-8453. (2)

Sun H., Zhang J., Rong Q., Feng D., Du Y., Zhang X., Su D., Zhou L., Feng, Z. X. Qiao, Hu M., (2013). A Hybrid Fiber Interferometer for Simultaneous Refractive Index and Temperature Measurements Based on Fabry Perot/Michelson Interference. IEEE, Sens. J., 13(5), 2039.

Sun H., Yang S., Zhang J., Rong Q., Liang L., Xu Q., Xiang G., Feng D., Du Y., Feng Z., Qiao X., Hu M., (2012). Temperature and refractive index sensing characteristics of an MZI-based multimode fiber–dispersion compensation fiber–multimode fiber structure. Opt. Fib. Technol., 18(6), 425-429.

Sun A. and Wu Z., (2012). A Hybrid LPG/CFBG for Highly Sensitive Refractive Index Measurements, J. Sens., 12, 7318-7325.

Szymańska M., Krogulski K., Mikulic P., Bock W.J., Śmietana M., (2014). Sensitivity of Long-period Gratings Modified by their Bending. Procedia Eng., 87, 1180-1183.

Swart, P.L., (2004). Long-period grating Michelson refractometric sensor. Meas. Sci. Technol., 15(8), 1576-1580.

Tai Y.-H., Wei P.-K., (2010). Sensitive liquid refractive index sensors using tapered optical fiber tips. Opt. Lett., Vol. 35(7), 944-946.

Takeishi R. T., Gusken E., Raizer K., de Souza H. G. E, Meirelles B. M., Giacomassi J. L., Lucio G. C., Suzuki C. K., (2008). Flexfuel Vehicle Alcohol-Gasoline Blend Ratios Determination by Optical Fiber Sensoring. 19th International Conference on Optical Fibre Sensors, Proc. of SPIE, Vol. 7004, 70044F.

Takeo, T. and Hattori, H., (1982). Optical fiber sensor for measuring refractive index, Jpn. J. of Applied Phys. 1, 21(10), 1509-12.

Tian Z., Yam S., and Loock H. P., (2008). Refractive index sensor based on an abrupt taper Michelson interferometer in a single-mode fiber. Opt. Lett., 33(10), 1105–1107.

Tian Y., Wang W., Wu N., Zou X., Guthy C., Wang X., (2011). A Miniature Fiber Optic Refractive Index Sensor Built in a MEMS-Based Microchannel. J. Sens., 11, 1078-1087.

Tien C.-L., Lin T.-W., Hsu H.-Y., Chen L.-C., Chen Y.-C., Liu W.-F., (2009). Double-Sided Polishing Long Period Fiber Grating Sensors for Measuring Liquid Refrac-

tive Index. Asia Communications and Photonics conference and Exhibition (ACP), Shanghai, pp. 1-2.

Toshima K., Satoh H., and Kimura M., (1999). One-dimensional vibration sensor using a Si-cantilever coupled with an optical fibre. Proc. SPIE 3878, Miniaturized Systems with Micro-Optics and MEMS, 350-357.

Trudeau J. M., Paradis P., Paré C., Meneghini C., Cournoyer A., Savard E., Doyon G., Jacob-Poulin A.-J. and Fougères A., (2006). Combined fibre-optic sensor for colour and refractive index (CI) monitoring. Meas. Sci. & Tech., 17(5), 1134-9.

Tzeng Y. and Lin T. H., (1987). Dry Etching od Silicon Materials in SF6 Based Plasmas. Roles of N2O and O2 Gas Additives. J. Electrochem. Soc., 134, 2304-2309.

Udd E., William B., Spillman Jr. (2011). Fibre Optic Sensors: An Application to engineers and scientists, (2nd Edition), Published by John Wiley and Sons.

Urrutia A., Goicoechea J., Ricchiuti A. L., Barrera D., Sales S., Arregui F. J., (2016). Simultaneous measurement of humidity and temperature based on a partially coated optical fiber long period grating. Sens. Actuators B Chem., 227, 135-141.

Van Etten, W. & Van der Plaats, J. (1991). Fundamentals of optical fiber communications. New York: Prentice Hall.

Van Brakel A., (2004). Sensing characteristics of an optical fibre long-period grating Michelson refractometer. PhD. thesis (Rand Afrikaans University, Johannesburg, 2004).

Vasiliev S. A., Dianov E. M., Varelas D., Limberger H. G., and Salathé R. P., (1996). Post-fabrication resonance peak positioning of long-period cladding-mode-coupled gratings. Opt. Lett., 21, 1830 –1832.

Vengsarkar, A.N., Lemaire, P.J., Judkins, J.B., Bhatia, V., Erdogan, T. and Sipe, J.E., (1996). Long-period fiber gratings as band-rejection filters. J. Lightw. Technol., 14(1), 58-65.

Viegas D., Goicoechea J., Corres J.M, Santos J.L., Ferreira L.A., Arajo F.M., Matias I.R., (2009). A fibre optic humidity sensor based on a long-period fibre grating coated with a thin film of SiO2 nanospheres. Meas. Sci. Technol., 20(3).

Villatoro J., Monzón-Hernández D., (2006). Low-Cost Optical Fiber Refractive-Index Sensor Based on Core Diameter Mismatch. IEEE, J. Lightw. Technol., 24(3), 1409-1413.

Vlahov, G., Shaw, A. D., Kell, D. B., (1999). Use of C-13 nuclear magnetic resonance distortionless enhancement by polarization transfer pulse sequence and multivariate analysis to discriminate olive oil cultivars. J. Am. Oil Chem. Soc., 76, 1223-1231.

Wang T., Wang M., (2012). Fabry–Pérot Fiber Sensor for Simultaneous Measurement of Refractive Index and Temperature Based on an In-Fiber Ellipsoidal Cavity. IEEE Photon. Technol. Lett., 24(19), 1733-1736.

Wang T., Yasukochi W., Korposh S., James S. W, Tatam R. P., Lee S.-W., (2016). A long period grating optical fiber sensor with nano-assembled porphyrin layers for detecting ammonia gas. Sens. Actuators B Chem., 228, 573-580.

Wang J., Shen C., Lu Y., Chen D., Zhong C., Chu J., Dong X., Chan C. C., (2011). Liquid refractive index sensor based on a polarization-maintaining fiber loop mirror. IEEE Sens. J., 13(5), 1721-1724,

Wang, P., Brambilla, G., Ding, M., Lee, T., Bo, L., Semenova, Y., Wu, Q, Farrell, G., (2013). Enhanced Refractometer Based on Periodically Tapered Small Core Singlemode Fiber. IEEE Sens. J., 13(1) 180-185.

Wang P., Brambilla G., Ding M., Semenova Y., Wu Q. and Farrell G., (2011). Investigation of single-mode-multimode-single-mode and singlemode-tapered-multimode-single-mode fiber structures and their application for refractive index sensing. J. Opt. Soc. Am. B, 28(5), 1180-1186.

Wang Z., Heflin J., Stolen R., and Ramachandran S., (2005). Analysis of optical response of long period fiber gratings to nm-thick thin-film coating. Opt. Express, 13(8), 2808-2813.

Wang Q., Du C., Zhang J., Lv R., Zhao Y., (2016). Sensitivity-enhanced temperature sensor based on PDMS-coated long period fiber grating. Opt. Commun., 377, 89-93.

Won P. C., Leng J., Lai Y., Williams J., (2004). Distributed temperature sensing using a chirped fibre Bragg grating. Meas. Sci. Technol., 15(8), 1501–1505.

Weast R.C. and Selby S.M. (ed), (1968). Handbook of Chemistry and Physics, (48th edition), CRC Handbook of Chemistry and Physics Press.

Wu Q., Semenova Y., Wang P., and Farrell G., (2011). High sensitivity SMS fiber structure based refractometer-Analysis and experiment. Opt. Express, 19(9), 7937-7944,

Xu H.-z., Lou J., Tan Y.-c., Li B.-c., Huang J., Shen W.-m., (2014). Simulation and analysis of sensitivity for tapered fiber Bragg grating evanescent wave sensor. Proc. SPIE 9297, International Symposium on Optoelectronic Technology and Application 2014: Laser and Optical Measurement Technology; and Fiber Optic Sensors, 92972R.

Xu M.G., Dong L., Reekie L., Tucknott J.A., Cruz J.L., (1995). Temperature independent strain sensor using a chirped Bragg grating in a tapered optical fibre. IEEE, Electron. Let., No: 19959542, 31(10), 823-825.

Xu W., Huang X. G., Pan J. S., (2013). A simple fiber-optic refractive index sensor based on Fresnel reflection and optical switch. IEEE Sens. J., 13, 1571–1574.

Xue L. L. and Yang L., (2012). Sensitivity enhancement of RI sensor based on SMS fiber structure with high refractive index overlay. J. Lightw. Technol., 30(10), 1463-1469.

Yang, H., Irudayaraj, J. (2001). Comparison of near-infrared, Fourier transform-infrared, and Fourier transform-Raman methods for determining olive pomace oil adulteration in extra virgin olive oil. J. Am. Oil Chem. Soc., 78, 889-895.

Yang J., Zhou L., Huang J., Tao C., Li X., Chen W., (2015). Sensitivity enhancing of transition mode long-period fiber grating as methane sensor using high refractive index polycarbonate/cryptophane A overlay deposition. Sens. Actuators B Chem., 207, Part A, 477-480.

Yariv, A., Yeh, P., (2007). Photonics, Optical Electronics in Modern Communication. (6th Ed.). New York: Oxford University Press.

Yariv A., (1973). Coupled-mode theory for guided-wave optics. IEEE J. Quant. Electron., 9(9), 919-933.

Yeh C.-H., Chow C.-W., Sung J.-Y., Wu P.-C., Whang W.-T., and Tseng F.-G., (2012). Measurement of organic chemical refractive indexes using an optical time-domain reflectometer. Sens., 12, 481–488.

Yin G., Wang Y., Liao C., Zhou J., Zhong X., Wang G., Sun B., He J., (2014). Long Period Fiber Gratings Inscribed by Periodically Tapering a Fiber. IEEE Photon. Technol. Lett., 26(7), 698-701.

Yuan J.-Y., Zhao C.-L., Ye M., Kang J., Zhang Z., and Jin S.-Z., (2014). A Fresnel reflection-based optical fiber sensor system for remote refractive index measurement using OTDR. Photon. Sens., 4, 48–52.

Yüksel K., (2016). Optical fiber sensor system for remote and multi-point refractive index measurement. Sens. Actuators A Phys., 250, 29-34.

Yong D., Yu X., Ren G., Zhang H., Zhang Y., Chan C. C, Wei H., Tong W., (2012). Photonic Bandgap Fiber for Infiltration-Free Refractive-Index Sensing, IEEE J. Select. Top. Quant. Electron., 18(5), 1560-1565.

Zhang X., Peng W., Liu Y., Pan L., (2013). Core–cladding mode recoupling based fiber optic refractive index sensor. Opt. Commu., 294, 188–191.

Zhang Q., Ianno N. J., Han M., (2013). Fiber-Optic Refractometer Based on an Etched High-Q π-Phase-Shifted Fiber-Bragg-Grating. J. Sens., 13, 8827-8834.

Zhao C.-L., Li J., Zhang S., Zhang Z., and Jin S., (2013). Simple Fresnel reflection-based optical fiber sensor for multipoint refractive index measurement using an AWG. Photon. Technol. Lett., 25, 606–608.

Zou F., Liu Y., Deng C., Dong Y., Zhu S., and Wang T., (2015). Refractive index sensitivity of nano-film coated long-period fiber gratings. Opt. Express, 23, 1114-1124.

Zhou, K. M., Zhang, L., Chen, X. F., Bennion, I., (2006). Optic sensors of high refractive-index responsivity and low thermal cross sensitivity that use fiber Bragg gratings of >80° tilted structures. Optics Let., 31(9), 1193-1195.

Zhou D., (2010). Optical Fiber Sensors for Temperature and Strain Measurement. UWSpace (University of Waterloo). http://hdl.handle.net/10012/5655

Zhou Y. H., Guang Q. X., Rajibul I. Md., Kok-Sing L., Ahmad H., (2014). Simultaneous measurement of aliphatic alcohol concentration and temperature based on etched taper FBG. Sens. Actuators B Chem., 202, 959-963.

Zibaii, M., Frazão, O., Latifi, H., Jorge, P. A. S., (2011). Controlling the sensitivity of refractive index measurement using a tapered fiber loop mirror. IEEE, Photon. Technol. Lett., 23, 1219-1221.

Zubia, J., Garitaonaindia, G., Arrue, J., (2000). Passive device based on plastic optical fibers to determine the indices of refraction of liquids. Appl. Opt., 39(6), 941-946.

APPENDIX A

WAVE EQUATION IN CYLINDRICAL COORDINATES AND BESSEL FUNCTIONS

A.1. Wave Equations in Cylindrical Coordinates

Propagation of light in optical fiber is described by Maxwell equations. The wave propagation equation in optical fibers can be derived from these equations after some assumptions. These assumptions are based on the physical properties of the fiber. The optical waveguide is assumed to consist of a linear, homogeneous, isotropic (Keiser, 2000), lossless (Okamoto, 2006), nonmagnetic (Kashyap, 1999), and dielectric material without any sources (Keiser, 2000).

Maxwell's equations (Keiser, 2000):

$$\nabla \times \mathbf{E} = -\frac{\partial \mathbf{B}}{\partial \mathrm{t}} \tag{A.1}$$

$$\nabla \times \mathbf{H} = \frac{\partial \mathbf{D}}{\partial \mathrm{t}} \tag{A.2}$$

$$\nabla . \mathbf{D} = 0 \tag{A.3}$$

$$\nabla . \mathbf{B} = 0 \tag{A.4}$$

E is the electric field vector and $\mathbf{D} = \varepsilon \mathbf{E}$ is the electric displacement vector (Kashyap, 1999) (ε is the permittivity and defined here as $\varepsilon = \varepsilon_0 n^2$ (Okamoto, 2006)), **H** is the magnetic field vector and $\mathbf{B} = \mu \mathbf{H}$ is the magnetic flux vector (Kashyap, 1999), (μ is the permeability and in this case $\mu = \mu_0$ (Okamoto, 2006)).

Standard wave equations can be derived from the above expressions. Equation (A.5) is obtained, by taking the curl of Equation (A.1) and substituting it into Equation (A.2):

$$\nabla \times (\nabla \times \mathbf{E}) = -\varepsilon \mu \frac{\partial^2 \mathbf{E}}{\partial t^2} \tag{A.5}$$

By using the vector identity $\nabla\times(\nabla\times\mathrm{b}) = \nabla.(\nabla.\mathrm{b}) - \nabla^2 b$ and Equation (A.3) (that is $\nabla.\mathbf{E} = 0$), one homogeneous wave equation is provided (Keiser, 2000; Yariv and Yeh, 2007):

$$\nabla^2\mathbf{E} = \varepsilon\mu\frac{\partial^2\mathbf{E}}{\partial t^2} \tag{A.6}$$

Similarly, by taking the curl of Equation (A.2) and substituting it into Equation (A.1), Equation (A.7) is obtained:

$$\nabla\times(\nabla\times\mathbf{H}) = -\varepsilon\mu\frac{\partial^2\mathbf{H}}{\partial t^2} \tag{A.7}$$

By using the vector identity $\nabla\times(\nabla\times\mathrm{b}) = \nabla.(\nabla.\mathrm{b}) - \nabla^2 b$ and Equation (A.4), other homogeneous wave equation is provided (Keiser, 2000; Yariv and Yeh, 2007):

$$\nabla^2\mathbf{H} = \varepsilon\mu\frac{\partial^2\mathbf{H}}{\partial t^2} \tag{A.8}$$

As the optical fibers are cylindrically symmetric, the wave equations can be described in cylindrical coordinates (cf. Figure A.1). The electric field components are E_r, E_ϕ, E_z and magnetic field components are H_r, H_ϕ, H_z. Those six field components are not independent of each other. Once the longitudinal components E_z and H_z are found, the other four components $(E_r, E_\phi, H_r, H_\phi)$ can be derived in terms of E_z and H_z using Maxwell's equations.

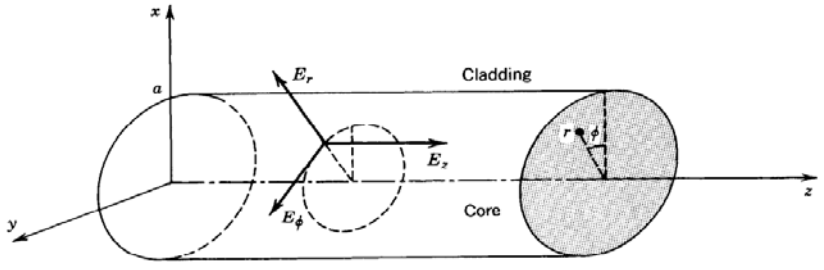

Figure A.1. Cylindrical co-ordinate system in optical fiber (Source: Saleh et.al, 1991).

Equation (A.9) and (A.10) are temporally and spatially harmonic phasors in cylindrical coordinates for a guided mode travelling in the z-direction (along the fiber axis) with an angular frequency ω and propagation constant β:

$$\mathbf{E}(\mathbf{r},t) = \mathbf{E}(r,\phi)\exp[\mathrm{j}(\omega t - \beta z)] \quad (A.9)$$

$$\mathbf{H}(\mathbf{r},t) = \mathbf{H}(r,\phi)\exp[\mathrm{j}(\omega t - \beta z)] \quad (A.10)$$

that is, every component of the field vector assumes the same z and t dependence of $\exp[\mathrm{j}(\omega t - \beta z)]$ (Yariv and Yeh, 2007).

Maxwell's equations are now written in the cylindrical coordinates by substitution of Equation (A.9) and (A.10) into the wave Equations (A.6) and (A.8), and the following waveguide equations are provided (Keiser, 2000; Okamoto, 2006; Yariv and Yeh, 2007):

$$j\omega\varepsilon E_r = j\beta H_\phi + \frac{1}{r}\frac{\partial}{\partial\phi}H_z$$

$$j\omega\varepsilon E_\phi = -j\beta H_r - \frac{\partial}{\partial r}H_z$$

$$j\omega\varepsilon E_z = -\frac{1}{r}\frac{\partial}{\partial\phi}H_r + \frac{1}{r}\frac{\partial}{\partial r}(rH_\phi)$$

and (A.11)

$$-j\omega\mu H_r = j\beta E_\phi + \frac{1}{r}\frac{\partial}{\partial\phi}E_z$$

$$-j\omega\mu H_\phi = -j\beta E_r - \frac{\partial}{\partial r}E_z$$

$$-j\omega\mu H_z = -\frac{1}{r}\frac{\partial}{\partial\phi}E_r + \frac{1}{r}\frac{\partial}{\partial r}(rE_\phi)$$

Using above equations E_ϕ, E_r, H_ϕ and H_r components can be determined in terms of E_z and H_z. The results are (Yariv and Yeh, 2007):

$$E_r = \frac{-j\beta}{\omega^2\mu\varepsilon - \beta^2}\left(\frac{\partial}{\partial r}E_z + \frac{\omega\mu}{\beta}\frac{\partial}{r\partial\phi}H_z\right)$$

$$E_\phi = \frac{-j\beta}{\omega^2\mu\varepsilon - \beta^2}\left(\frac{\partial}{r\partial\phi}E_z - \frac{\omega\mu}{\beta}\frac{\partial}{\partial r}H_z\right)$$

and (A.12)

$$H_r = \frac{-j\beta}{\omega^2\mu\varepsilon - \beta^2}\left(\frac{\partial}{\partial r}H_z - \frac{\omega\varepsilon}{\beta}\frac{\partial}{r\partial\phi}E_z\right)$$

$$H_\phi = \frac{-j\beta}{\omega^2\mu\varepsilon - \beta^2}\left(\frac{\partial}{r\partial\phi}H_z + \frac{\omega\varepsilon}{\beta}\frac{\partial}{\partial r}E_z\right)$$

According to these relations, determining of E_z and H_z is sufficient to specify the wave solution.

In the refractive index profile (especially for step-index fibers) discontinuities exist and this directly affects the permittivity. Boundary conditions limit the possibilities provided by the Equations in (A.12) (Okamoto, 2006). The boundary conditions are given as:

1) The tangential components of electric and magnetic field are continuous along the core-cladding boundary. Therefore, at the cladding-core interface ($r = a$), the tangential components of the electric and magnetic fields must match their counterparts (Keiser, 2000):

$$E_{\phi}^{(co)} = E_{\phi}^{(cl)}, H_{\phi}^{(co)} = H_{\phi}^{(cl)} \quad \text{(A.13)}$$

$$E_{z}^{(co)} = E_{z}^{(cl)}, H_{z}^{(co)} = H_{z}^{(cl)} \quad \text{(A.14)}$$

2) A natural boundary condition also requires that the electric and magnetic field vectors tend to zero at infinity (Okamoto, 2006).

Wave equation in cylindrical coordinates is found by writing Equation (A.12) in terms of E_z and H_z (Keiser, 2000; Yariv and Yeh, 2007):

$$\frac{\partial^2 E_z}{\partial r^2} + \frac{1}{r}\frac{\partial E_z}{\partial r} + \frac{1}{r^2}\frac{\partial^2 E_z}{\partial \phi^2} + (k^2 n^2 - \beta^2)E_z = 0 \quad \text{(A.15)}$$

and

$$\frac{\partial^2 H_z}{\partial r^2} + \frac{1}{r}\frac{\partial H_z}{\partial r} + \frac{1}{r^2}\frac{\partial^2 H_z}{\partial \phi^2} + (k^2 n^2 - \beta^2)H_z = 0 \quad \text{(A.16)}$$

where $k^2 = \omega^2 \mu \varepsilon$.

A.2. Wave Equations for Step Index Fiber

The refractive index distribution for a step-index fiber with a core diameter a is as follows (Marcuse, 1979):

$$n(r) = \begin{cases} n_{co}, & 0 \le r \le a \\ n_{cl}, & r > a \end{cases} \quad \text{(A.17)}$$

Figure A.2 shows the longitudinal cross-sectional area of a single-mode and multi-mode step index fibers and index profiles of them, n_1 is core refractive index (n_{co}) and n_2 is cladding refractive index (n_{cl}).

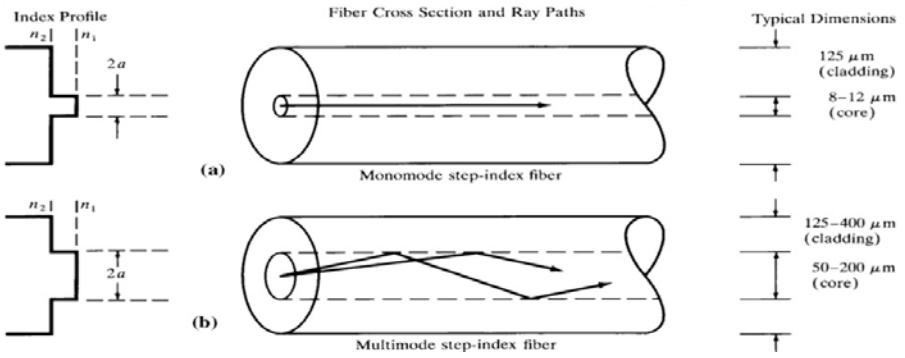

Figure A.2. (a) Single-mode and (b) multi-mode step-index optical fibers (Source: Keiser, 2000).

As mentioned before; limited propagation occurs in fibers. These propagation modes are referred to as guided modes (or guided waves, confined modes), and the structures that support guided modes are called waveguides.

Figure A.3 shows the electric field distributions of various lower-order guided modes in a symmetrical slab waveguide, in two dimensions. In practice, the fiber optic cladding radius is generally chosen to be large enough so that the core-guided modes have exponentially decreasing fields outside the core and the guide-mode field does not reach the outer boundary of the cladding (the field of the guided-waves is almost zero at $r = a_{cl}$) (Keiser, 2000).

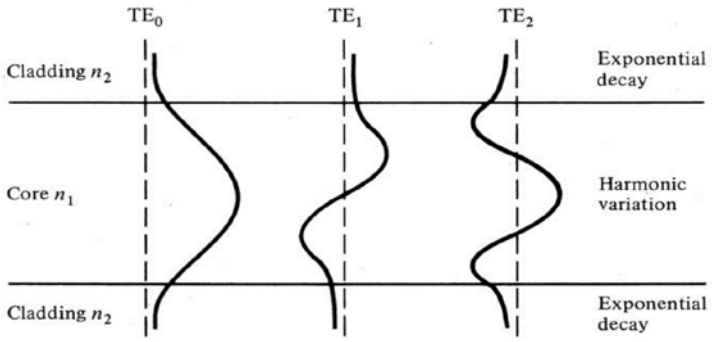

Figure A.3. Two-dimensional electric field distributions of some lower-order guided modes (Source Keiser, 2000).

In order to find the different guided modes in a step-index fiber, the wave equations (A.15) and (A.16) should be solved for E_z and H_z in the core and cladding regions, then solutions can be obtained for the transverse components from equation (A.12) (Cherin, 1983). For solving the Equation (A.15), a standard mathematical procedure, namely the separation of variables method can be used. The solution is assumed to be of the following form (Keiser, 2000):

$$E_z = AF_1(r)F_2(\phi)F_3(z)F_4(t) \tag{A.18}$$

As was already assumed, the time- and z-dependent factors are given by:

$$F_3(z)F_4(t) = \exp[\mathrm{j}(\omega\mathrm{t} - \beta\mathrm{z})] \tag{A.19}$$

since the wave is sinusoidal in time and its propagation direction is z. $F_2(\phi)$ field component must be the same when the coordinate ϕ is increased by 2π, because of the circular symmetry of the waveguide. Thus, we assume a periodic function for $F_2(\phi)$ (Keiser, 2000):

$$F_2(\phi) = e^{j\nu\phi} \tag{A.20}$$

ν is a constant. It can be positive or negative, but it must be an integer since the fields must be periodic in ϕ with a period of 2π.

Substituting (A.20) and (A.19) into (A.18) the wave equation for E_z [(A.15)] becomes

$$\frac{\partial^2 F_1}{\partial r^2} + \frac{1}{r}\frac{\partial F_1}{\partial r} + \left((k^2n^2 - \beta^2) - \frac{\nu^2}{r^2}\right)F_1 = 0 \tag{A.21}$$

which is a well-known differential equation for Bessel functions (Abramowitz and Stegun, 1965; Mathews and Walker, 1970; Beyer, 1987). Similarly, an identical equation can be derived for H_z. We can write the wave Equations (A.15) and (A.16) in the following forms:

$$\frac{\partial^2 E_z(r)}{\partial r^2} + \frac{1}{r}\frac{\partial E_z(r)}{\partial r} + \left((k^2n^2 - \beta^2) - \frac{\nu^2}{r^2}\right)E_z(r) = 0 \tag{A.22}$$

$$\frac{\partial^2 H_z(r)}{\partial r^2} + \frac{1}{r}\frac{\partial H_z(r)}{\partial r} + \left((k^2 n^2 - \beta^2) - \frac{\nu^2}{r^2}\right) H_z(r) = 0 \qquad (A.23)$$

Equation (A.22) and (A.23) must be solved separately for the core and cladding regions. Since $h^2 = k^2 n^2 - \beta^2$, it is defined to be positive in the core, and negative in the cladding.

a) Core Region ($0 \leq r \leq \alpha$)

For the core region (Okamoto, 2006; Adams, 1981):

$$\kappa^2 = k^2 n_{co}^2 - \beta^2 > 0 \qquad (A.24)$$

Then the Bessel equations for this region:

$$\frac{\partial^2 R(r)}{\partial r^2} + \frac{1}{r}\frac{\partial R(r)}{\partial r} + \left(\kappa^2 - \frac{\nu^2}{r^2}\right) R(r) = 0 \qquad (A.25)$$

where $R(r) = E_z(r)\ or\ H_z(r)$. The solution of the Equation (A.25) (Van Etten and Van der Plaats, 1991):

$$R(r) = XJ_\nu(\kappa r) + YN_\nu(\kappa r) \qquad (A.26)$$

X and Y constants. J_ν is a Bessel function of the first kind, and N_ν is a Bessel function of the second kind (or Neumann function (Okamoto, 2006)), both of order ν (Adams, 1981). The solutions for the guided modes must remain finite as $r \to 0$. $N_\nu(0) = -\infty$, this means that $Y = 0$ in equation (A.26) and therefore in the core (Okamoto, 2006; Adams, 1981):

$$E_z^{(co)} = AJ_\nu(\kappa r)e^{j\nu\phi}e^{j(\omega t - \beta z)} \qquad (A.27)$$

$$H_z^{(co)} = BJ_\nu(\kappa r)e^{j\nu\phi}e^{j(\omega t - \beta z)} \qquad (A.28)$$

b) Cladding Region ($r > \alpha$)

For the cladding region (Okamoto, 2006; Adams, 1981);

$$-\sigma^2 = k^2 n_{cl}^2 - \beta^2 < 0 \tag{A.29}$$

Then the Bessel equations for this region:

$$\frac{\partial^2 R(r)}{\partial r^2} + \frac{1}{r}\frac{\partial R(r)}{\partial r} + \left(\sigma^2 + \frac{\nu^2}{r^2}\right) R(r) = 0 \tag{A.30}$$

where $R(r) = E_z(r)\ or\ H_z(r)$. The solution of the Equation (A.30) (Van Etten and Van der Plaats, 1991):

$$R(r) = XI_\nu(\sigma r) + YK_\nu(\sigma r) \tag{A.31}$$

X and Y constants. In this case I_ν is a modified Bessel function of the first kind and K_ν is a modified Bessel function of the second kind (or modified Hankel function (Adams, 1981)), both of order ν. On the outside of the core the solutions must decay to zero as $r \to \infty$. However, $I_\nu(\sigma r)$ diverges infinitely at $r = \infty$. Therefore, $K_\nu(\sigma r)$ is the proper solution in the cladding region, and $X = 0$ in Equation (A.31). In the cladding (Okamoto, 2006; Adams, 1981):

$$E_z^{(cl)} = CK_\nu(\sigma r)e^{j\nu\phi}e^{j(\omega t - \beta z)} \tag{A.32}$$

$$H_z^{(cl)} = DK_\nu(\sigma r)e^{j\nu\phi}e^{j(\omega t - \beta z)} \tag{A.33}$$

Normalized transverse wave numbers are (Okamoto, 2006):

$$u = \kappa\alpha = \alpha\sqrt{k^2 n_{co}^2 - \beta^2} \tag{A.34}$$

$$w = \sigma\alpha = \alpha\sqrt{\beta^2 - k^2 n_{cl}^2} \tag{A.35}$$

Another important parameter for the fibers is the normalized frequency, V, (also called as the fiber parameter, V-parameter (Saleh and Teich, 1991) or V-number (Oka-

moto, 2006; Marcuse, 1979). V-number gives the number of modes a fiber can support. It is related to the normalized transverse wave numbers (Okamoto, 2006; Erdogan, 1997):

$$V^2 = u^2 + w^2 = \left(\frac{2\pi\alpha}{\lambda}\sqrt{n_{co}^2 - n_{cl}^2}\right)^2 = k^2(n_{co}^2 - n_{cl}^2)\alpha^2 \qquad (A.36)$$

Longitudinal components of the electromagnetic fields in terms of u and w:

$$E_z = \begin{cases} AJ_v(ur/a)e^{jv\phi}e^{j(\omega t-\beta z)}, & 0 \le r \le a \\ CK_v(wr/a)e^{jv\phi}e^{j(\omega t-\beta z)}, & r > a \end{cases} \qquad (A.37)$$

$$H_z = \begin{cases} BJ_v(ur/a)e^{jv\phi}e^{j(\omega t-\beta z)}, & 0 \le r \le a \\ DK_v(wr/a)e^{jv\phi}e^{j(\omega t-\beta z)}, & r > a \end{cases} \qquad (A.38)$$

A.3 Modes in Step Index Fiber and Derivation of Characteristic Equations

The boundary conditions in (A.13) and (A.14) determine whether coupling occurs between E_z and H_z (Keiser, 2000). These determine the type of obtained mode solutions. If there is no coupling between field components, mode solutions can be obtained in either transverse electric (TE) modes (for which $E_z = 0$), or transverse magnetic (TM) modes (for which $H_z = 0$). Usually, however, coupling between the E_z and H_z field components occurs in the optical fiber waveguides. These modes called as hybrid modes (for which both E_z and H_z are nonzero). Hybrid modes are represented as HE or EH modes, respectively depending on whether the magnetic component, H_z, or the electric component, E_z, has a dominant influence on the magnitude of the transverse field (Keiser, 2000).

a) TE Modes

Substitution of the condition for TE modes ($E_z = 0$) into Equation (A.12), yields the following set of equations (Okamoto, 2006; Mathews, 1970):

$$E_r = -\frac{j\omega\mu}{[k^2n^2 - \beta^2]}\left(\frac{1}{r}\frac{\partial H_z}{\partial \phi}\right)$$

$$E_\phi = \frac{j\omega\mu}{[k^2n^2 - \beta^2]}\left(\frac{\partial H_z}{\partial r}\right)$$

and (A.39)

$$H_r = -\frac{j\beta}{[k^2n^2 - \beta^2]}\left(\frac{\partial H_z}{\partial r}\right)$$

$$H_\phi = -\frac{j\beta}{[k^2n^2 - \beta^2]}\left(\frac{1}{r}\frac{\partial H_z}{\partial \phi}\right)$$

The boundary conditions (given in (A.13) and (A.14)) at the core-cladding interface, requires only continuity of the tangential components H_z, H_ϕ and E_ϕ ($E_z = 0$ for TE modes) (Okamoto, 2006).

Equation (A.38) can be simplified by neglecting the time and z-dependent ($e^{j(\omega t - \beta z)}$) components (Van Etten and Van der Plaats, 1991):

$$H_z = \begin{cases} BJ_\nu(ur/a)e^{j\nu\phi}, & 0 \le r \le a \\ DK_\nu(wr/a)e^{j\nu\phi}, & r > a \end{cases} \quad (A.40)$$

By substituting (A.40) into (A.39), we get:

$$H_\phi = \begin{cases} \left(\frac{\nu\beta}{\kappa^2 r}\right) BJ_\nu(ur/a)e^{j\nu\phi}, & 0 \le r \le a \\ -\left(\frac{\nu\beta}{\sigma^2 r}\right) DK_\nu(wr/a)e^{j\nu\phi}, & r > a \end{cases} \quad (A.41)$$

and

$$E_\phi = \begin{cases} \left(\frac{j\omega\mu}{\kappa}\right) BJ'_\nu(ur/a)e^{j\nu\phi}, & 0 \le r \le a \\ -\left(\frac{j\omega\mu}{\sigma}\right) DK'_\nu(wr/a)e^{j\nu\phi}, & r > a \end{cases} \quad (A.42)$$

If the first two continuity conditions are applied at $r = a$ for H_z and H_ϕ, then (Okamoto, 2006):

$$H_z^{(co)}(a) = H_z^{(cl)}(a) \quad (A.43)$$

$$BJ_\nu(u) = DK_\nu(w)$$

$$H_{\phi}^{(co)}(a) = H_{\phi}^{(cl)}(a) \tag{A.44}$$

$$\left(\frac{B}{\kappa^2}\right) J_{\nu}(u) = -\left(\frac{D}{\sigma^2}\right) K_{\nu}(w)$$

In the step-index fiber, the refractive index at the boundary of the core is not equal to the refractive index of the cladding. The only way to satisfy the boundary conditions is thus to set ν = 0. Consequently, the azimuthal dependency in the TE modes $\partial/\partial\phi = 0$, and H_{ϕ}, E_r are found zero from equations (A.39) (Okamoto, 2006):

$$H_{\phi} = E_r = 0 \tag{A.45}$$

If the derivatives of zeroth order Bessel functions are transformed into the first order functions when writing the remaining TE modes for ν = 0 (Okamoto, 2006):

$$J_0'(u) = -J_1(u) \tag{A.46}$$

$$K_0'(w) = -K_1(w)$$

The remaining field components can be given as (Okamoto, 2006):

$$H_z = \begin{cases} BJ_0(ur/a), & 0 \le r \le a \\ DK_0(wr/a), & r > a \end{cases} \tag{A.47}$$

$$E_{\phi} = \begin{cases} -\left(\frac{j\omega\mu a}{u}\right) BJ_1(ur/a), & 0 \le r \le a \\ \left(\frac{j\omega\mu a}{w}\right) DK_1(wr/a), & r > a \end{cases} \tag{A.48}$$

$$H_r = \begin{cases} -\left(\frac{j\beta a}{u}\right) BJ_1(ur/a), & 0 \le r \le a \\ \left(\frac{j\beta a}{w}\right) DK_1(wr/a), & r > a \end{cases} \tag{A.49}$$

By using the boundary conditions (continuity of H_z and E_{ϕ} (or H_r)) at the core cladding interface ($r = a$), the following expressions are derived:

$$BJ_0(u) = DK_0(w) \tag{A.50}$$

$$-\left(\frac{B}{u}\right) J_1(u) = \left(\frac{D}{w}\right) K_1(w) \tag{A.51}$$

For the TE modes, it is now possible to obtain the characteristic equation (or the eigenvalue equation) from Equations (A.50) and (A.51) (Okamoto, 2006; Saleh and Teich, 1991):

$$\frac{1}{u}\frac{J_1(u)}{J_0(u)} = -\frac{1}{w}\frac{K_1(w)}{K_0(w)} \tag{A.52}$$

b) TM Modes

If the same derivations are also made for the TM modes, as previously done for TE modes ($H_z = 0$ in this case), then it is once again found that the boundary conditions require ν = 0 (Okamoto, 2006). Hence, the electromagnetic field components are:

$$\begin{aligned} E_r &= -\frac{j\beta}{[k^2n^2 - \beta^2]}\left(\frac{\partial E_z}{\partial r}\right) \\ H_\phi &= -\frac{j\omega\varepsilon}{[k^2n^2 - \beta^2]}\left(\frac{\partial E_z}{\partial r}\right) \\ E_\phi &= H_r = 0 \end{aligned} \tag{A.53}$$

Solving the Bessel equation in the core region and the cladding region, with ν = 0, provides the expression for E_z. It can then be used to find E_r and H_ϕ (Okamoto, 2006; Adams, 1981) (to simplify the resulting expressions, in here once again proportionality to $e^{j(\omega t - \beta z)}$ has been ignored):

$$E_z = \begin{cases} AJ_0(ur/a), & 0 \le r \le a \\ CK_0(wr/a), & r > a \end{cases} \tag{A.54}$$

$$H_\phi = \begin{cases} \left(\frac{j\omega\varepsilon_{co}a}{u}\right)AJ_1(ur/a), & 0 \le r \le a \\ -\left(\frac{j\omega\varepsilon_{cl}a}{w}\right)CK_1(wr/a), & r > a \end{cases} \tag{A.55}$$

$$E_r = \begin{cases} \left(\frac{j\beta a}{u}\right)AJ_1(ur/a), & 0 \le r \le a \\ -\left(\frac{j\beta a}{w}\right)CK_1(wr/a), & r > a \end{cases} \tag{A.56}$$

By using the boundary conditions (continuity of E_z and E_r (or H_ϕ)) at the core cladding interface ($r = a$), the following expressions are derived:

$$AJ_0(u) = CK_0(w) \tag{A.57}$$

$$\left(\frac{\varepsilon_{co}}{u}\right) AJ_1(u) = -\left(\frac{\varepsilon_{cl}}{w}\right) CK_1(w) \tag{A.58}$$

The characteristic equation for TM modes is found by combining these two equations (Cherin, 1983):

$$\frac{1}{u}\frac{J_1(u)}{J_0(u)} = -\left(\frac{\varepsilon_{cl}}{\varepsilon_{co}}\right)\frac{1}{w}\frac{K_1(w)}{K_0(w)} \tag{A.59}$$

where $\varepsilon = \varepsilon_0 n^2$ (Okamoto, 2006), so the dispersion equation for TM modes can be written in terms of core and cladding refractive indices:

$$\frac{1}{u}\frac{J_1(u)}{J_0(u)} = -\left(\frac{n_{cl}}{n_{co}}\right)\frac{1}{w}\frac{K_1(w)}{K_0(w)} \tag{A.60}$$

c) Hybrid Modes

In hybrid modes, the axial electromagnetic field components E_z and H_z are non-zero. Hence, the characteristic equation for hybrid modes are more complicated than were derived for TE and TM modes. Time and z-dependence are neglected again. By taking this into consideration, the longitudinal electromagnetic fields are expressed as in (A.61) and (A.62) (Okamoto, 2006; Yariv and Yeh, 2007; Cherin, 1983; Adams, 1981):

$$E_z = \begin{cases} AJ_\nu(ur/a)e^{j\nu\phi}, & 0 \le r \le a \\ CK_\nu(wr/a)e^{j\nu\phi}, & r > a \end{cases} \tag{A.61}$$

$$H_z = \begin{cases} BJ_\nu(ur/a)e^{j\nu\phi}, & 0 \le r \le a \\ DK_\nu(wr/a)e^{j\nu\phi}, & r > a \end{cases} \tag{A.62}$$

As were done for TE and TM modes, the remaining field components are obtained by substituting E_z and H_z into (A.12):

$$E_r = \begin{cases} -\frac{ja^2}{u^2}\left[A\beta\frac{u}{a}J_\nu'(ua/r) + jB\nu\frac{\omega\mu_0}{r}J_\nu(ur/a)\right]e^{j\nu\phi}, & 0 \le r \le a \\ -\frac{ja^2}{w^2}\left[C\beta\frac{w}{a}K_\nu'(wa/r) + jD\nu\frac{\omega\mu_0}{r}K_\nu(wa/r)\right]e^{j\nu\phi}, & r > a \end{cases} \quad (A.63)$$

$$E_\phi = \begin{cases} -\frac{ja^2}{u^2}\left[jA\beta\frac{\nu}{r}J_\nu(ua/r) - B\omega\mu_0\frac{u}{a}J_\nu'(ua/r)\right]e^{j\nu\phi}, & 0 \le r \le a \\ -\frac{ja^2}{w^2}\left[C\beta\frac{\nu}{r}K_\nu(wa/r) - D\omega\mu_0\frac{w}{a}K_\nu'(wa/r)\right]e^{j\nu\phi}, & r > a \end{cases} \quad (A.64)$$

$$H_r = \begin{cases} -\frac{ja^2}{u^2}\left[-jA\omega\varepsilon_0 n_{co}^2\left(\frac{\nu}{r}\right)J_\nu(ua/r) + B\beta\frac{u}{a}J_\nu'(ua/r)\right]e^{j\nu\phi}, & 0 \le r \le a \\ -\frac{ja^2}{w^2}\left[-C\omega\varepsilon_0 n_{cl}^2\left(\frac{\nu}{r}\right)K_\nu\left(\frac{wa}{r}\right) + D\beta\frac{w}{a}K_\nu'(wa/r)\right]e^{j\nu\phi}, & r > a \end{cases} \quad (A.65)$$

$$H_\phi = \begin{cases} -\frac{ja^2}{u^2}\left[A\omega\varepsilon_0 n_{co}^2\left(\frac{u}{a}\right)J_\nu'(ua/r) + jB\beta\frac{\nu}{r}J_\nu(ua/r)\right]e^{j\nu\phi}, & 0 \le r \le a \\ -\frac{ja^2}{w^2}\left[C\omega\varepsilon_0 n_{cl}^2\left(\frac{w}{a}\right)K_\nu'(wa/r) + D\beta\frac{\nu}{r}K_\nu(wa/r)\right]e^{j\nu\phi}, & r > a \end{cases} \quad (A.66)$$

where $J_\nu'(ua/r) = \frac{\partial J_\nu(ua/r)}{\partial(ua/r)}$ *and* $K_\nu'(ua/r) = \frac{\partial K_\nu(wa/r)}{\partial(wa/r)}$.

The constants A, B, C and D are found by applying boundary conditions described in equation (A.13) and (A.14) (Okamoto, 2006; Yariv and Yeh, 2007):

$$AJ_\nu(u) = CK_\nu(w) \quad (A.67)$$

$$A\left(\frac{\beta\nu}{u^2a}\right)J_\nu(u) + jB\left(\frac{\omega\mu_0}{ua}\right)J_\nu'(u) = -jC\left(\frac{\beta\nu}{w^2a}\right)K_\nu(w) + jD\left(\frac{\omega\mu_0}{wa}\right)K_\nu'(w) \quad (A.68)$$

$$BJ_\nu(u) = DK_\nu(w) \quad (A.69)$$

$$-jA\left(\frac{\omega\varepsilon_0 n_{co}^2 a}{u}\right)J_\nu'(u) + B\left(\frac{\beta\nu}{u^2a}\right)J_\nu(u) = C\left(\frac{\omega\varepsilon_0 n_{cl}^2 a}{w}\right)K_\nu'(w) + jD\left(\frac{\beta\nu}{w^2a}\right)K_\nu(w) \quad (A.70)$$

The characteristic equation for hybrid (HE or EH) modes is given by (Okamoto, 2006; Cherin, 1983; Adams, 1981):

$$\left[\frac{1}{u}\frac{J_\nu'(u)}{J_\nu(u)} + \frac{1}{w}\frac{K_\nu'(w)}{K_\nu(w)}\right]\left[n_{cl}^2\left(\frac{1}{u}\right)\frac{J_\nu'(u)}{J_\nu(u)} + n_{co}^2\left(\frac{1}{w}\right)\frac{K_\nu'(w)}{K_\nu(w)}\right] = \frac{\beta^2}{k^2}\left(\frac{1}{u^2} + \frac{1}{w^2}\right)\nu^2 \quad (A.71)$$

By using the equations of the normalized transverse wave numbers u and w given in (A.34) and (A.35), the following relation is found (Okamoto, 2006):

$$\frac{\beta^2}{k^2}\left(\frac{1}{u^2}+\frac{1}{w^2}\right)=\frac{n_{co}^2}{u^2}+\frac{n_{cl}^2}{w^2} \tag{A.72}$$

Using the above equation, the eigenvalue equation of the hybrid modes (A.71) can also be written in terms of the index of refraction:

$$\left[\frac{1}{u}\frac{J_\nu'(u)}{J_\nu(u)}+\frac{1}{w}\frac{K_\nu'(w)}{K_\nu(w)}\right]\left[\frac{1}{u}\frac{J_\nu'(u)}{J_\nu(u)}+\left(\frac{n_{cl}}{n_{co}}\right)^2\frac{1}{w}\frac{K_\nu'(w)}{K_\nu(w)}\right]=\left[\frac{1}{u^2}+\left(\frac{n_{cl}}{n_{co}}\right)^2\frac{1}{w^2}\right]\left(\frac{1}{u^2}+\frac{1}{w^2}\right)\nu^2 \tag{A.73}$$

A.4. Solution of Characteristic Equations

It is now appropriate to solve the derived characteristic equations for TE, TM and hybrid modes to determine eigenvalues corresponding to each different mode. Since there is no analytical solution, the characteristic equations must be solved graphically or numerically (Buck, 1995). Figure A.4 shows curves of $J_0(u), J_1(u), J_2(u)$ and $J_0'(u) = -J_1(u)$ which are lower-order first kind Bessel functions (Yariv and Yeh, 2007; Van Etten and Van der Plaats, 1991).

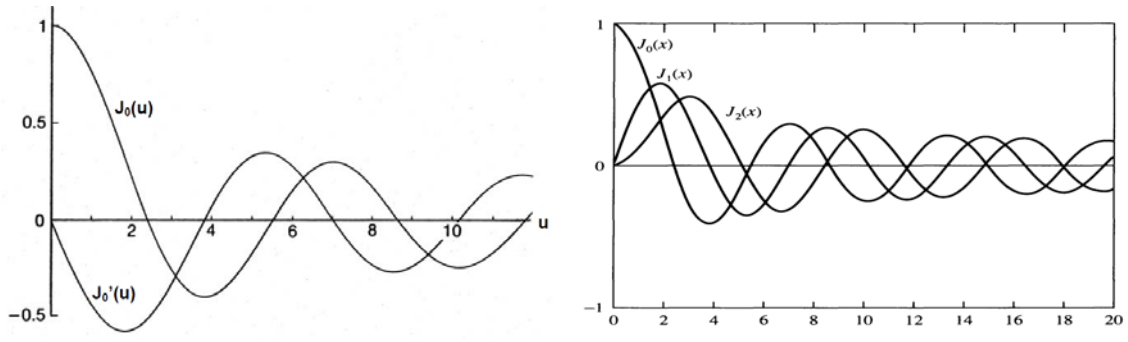

Figure A.4. Bessel functions of the first kind (Sources: Yariv and Yeh, 2007).

The characteristic equation here will be solved graphically for the TE modes. The same method can be applied for hybrid modes and TM modes.

The eigenvalue equation found in Equation (A.52) for TE modes is as follows:

$$\frac{1}{u}\frac{J_1(u)}{J_0(u)} = -\frac{1}{w}\frac{K_1(w)}{K_0(w)} \tag{A.74}$$

When the left-hand side of Equation (A.74) plotted against u, it will be form in curves similar to tangential function (Buck, 1995) as shown in Figure A.5. In this figure, the right-hand side and the left-hand side of Equation (A.74) is plotted on the same graph. Intersection points are eigenvalues that are the roots, u, of the characteristic equation (Van Etten and Van der Plaats, 1991). Once the fiber's V-parameter has been calculated by substitution of the physical parameters into equation (A.36), w is also known from equation $V^2 = u^2 + w^2$, and the propagation constant (β), for that particular mode can be obtained (Buck, 1995). V-number determines the number of solutions (see Figure A.6).

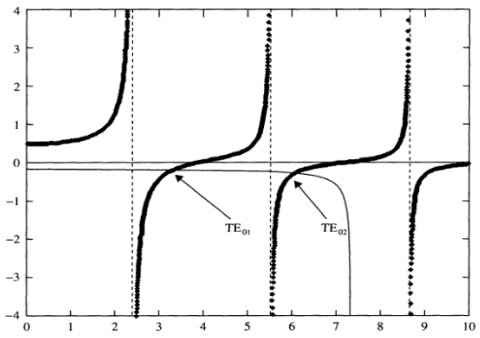

Figure A.5. Graphical determination of the propagation constants of TE modes ($\nu = 0$), ($n_{co} = 1.4628$, $n_{cl} = 1.4600$, $a = 20\mu m$, and $V = 7.334$) (Source: Yariv and Yeh, 2007).

The intersections of the graph in Figure A.5 correspond to the TE_{01} and TE_{02} modes. In here the subscript is in the form (ν, m) ($TE_{\nu m}$, $\nu = 0$ *and* $m \geq 1$) (Buck, 1995). ν and m are used to describe the distributions of the fields. ν is the azimuthal mode number and it relates to the angular variation of the field. If ν is zero, E_z and H_z are not dependent on ϕ. m is the radial mode number and it describes the field variation in the radial direction. Regardless of the mode type, each value of m is associated with certain values u, w and β. As has already found earlier, for the TM modes ν equals zero, as in TE modes. In hybrid modes, it is different from zero and there is no TE_{0m} or TM_{0m} modes. These modes are represented as $HE_{\nu m}$ or $EH_{\nu m}$ depending on which field effect is dominant.

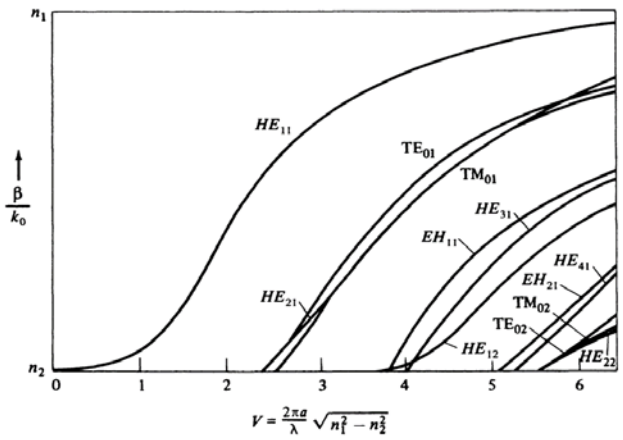

Figure A.6. Normalized propagation constant as a function of V-parameter for a few of the lowest-order modes of a step-index waveguide (Source: Keck, 1976).

For a single mode fiber, the V-number according to Figure A.6 should be less than 2.405. In such a fiber, all modes except HE_{11} mode are cut off. This kind of a step-index fiber supports only the two orthogonally polarized HE_{11} modes and both polarizations have same n_{eff} and speed. The HE_{11} mode is called as the dominant mode or the fundamental mode, and these kinds of fibers are called as single-mode or mono-mode fibers.

APPENDIX B

WEAKLY GUIDING APPROXIMATION AND LP MODES

B.1. Application of The Weakly Guiding Approximation and Characteristic Equation for Linearly Polarized (LP) Modes

The propagation modes in the circular waveguides are generally a mixture of TE and TM modes. The exact solutions of these hybrid modes (EH and HE modes) found by the characteristic Equation (A.73) obtained in Appendix A are highly complex. For this reason, a fairly accurate approach is applied. This section will describe this approach, which is called as weakly guided approximation (Keiser, 2000). This approach simplifies the analysis process compared to the definite mode solutions. And these simplified solutions are called linearly polarized modes (LP modes). This method assumes that the relative difference in refractive index (Δ) between the fibre's core and cladding is very small (typically in the order of 1%) (Okamoto, 2006). In practice, most fibers' core refractive index is only slightly higher than that of the cladding. The core-cladding index difference, given by (Keiser, 2000):

$$\Delta = 1 - \frac{n_{cl}}{n_{co}} \tag{B.1}$$

is extremely small in the weakly guiding approximation (i.e. smaller than 0.05 (Cherin, 1983)), since:

$$\frac{n_{cl}}{n_{co}} \cong 1 \qquad \longrightarrow \qquad \Delta \ll 1 \tag{B.2}$$

The using of the Equation (B.2) in Equation (A.73) and the application of the square root yields the following equation (Okamoto, 2006):

$$\frac{1}{u}\frac{J_\nu'(u)}{J_\nu(u)} + \frac{1}{w}\frac{K_\nu'(w)}{K_\nu(w)} = \pm\left(\frac{1}{u^2} + \frac{1}{w^2}\right)\nu \tag{B.3}$$

where $\nu \geq 1$.

The following Bessel function relations are appropriate in solving (B.3) (Okamoto, 2006):

$$J_\nu'(u) = \frac{1}{2}[J_{\nu-1}(u) - J_{\nu+1}(u)] \tag{B.4}$$

$$K_\nu'(w) = -\frac{1}{2}[K_{\nu-1}(w) + K_{\nu+1}(w)] \tag{B.5}$$

By using the Equations (B.4) and (B.5), Equation (B.3) can be simplified to yield the following two equations below (Okamoto, 2006; Yariv and Yeh, 2007; Buck, 1995):

$$\frac{1}{u}\frac{J_{\nu+1}(u)}{J_\nu(u)} = -\frac{1}{w}\frac{K_{\nu+1}(w)}{K_\nu(w)} \tag{B.6}$$

and

$$\frac{1}{u}\frac{J_{\nu-1}(u)}{J_\nu(u)} = \frac{1}{w}\frac{K_{\nu-1}(w)}{K_\nu(w)} \tag{B.7}$$

The Equation (B.6) is obtained from the negative sign of the Equation (B.3) and corresponds to the EH modes, the Equation (B.7) is obtained from the positive part of the (B.3) and corresponds to the HE modes (Okamoto, 2006).

The dispersion relation for the HE modes for the azimuthal mode number $\nu \geq 2$ can be rewritten as follows.

$$\frac{1}{u}\frac{J_{\nu-1}(u)}{J_{\nu-2}(u)} = -\frac{1}{w}\frac{K_{\nu-1}(w)}{K_{\nu-2}(w)} \tag{B.8}$$

For deriving this equation; first, equation (B.7) is reversed. Then the following Bessel function relations (B.9) and (B.10) are applied to $J_\nu(u)$ and $K_\nu(w)$ (Okamoto, 2006).

$$(\nu/u)J_\nu(u) = \frac{1}{2}[J_{\nu-1}(u) + J_{\nu+1}(u)] \tag{B.9}$$

$$(\nu/w)K_\nu(w) = -\frac{1}{2}[K_{\nu-1}(w) - K_{\nu+1}(w)] \tag{B.10}$$

When the weakly guiding approximation ($n_{cl}/n_{co} \cong 1$) is applied to the Equation (A.60) for the TM modes, the following dispersion relation is found:

$$\frac{1}{u}\frac{J_1(u)}{J_0(u)} = -\frac{1}{w}\frac{K_1(w)}{K_0(w)} \tag{B.11}$$

This equation is same as the dispersion equation for TE modes (A.51).

Table B.1 summarizes the dispersion equations for TE, TM and hybrid EH and HE modes under the weakly guiding approximation:

Table B.1. Dispersion equations under the weakly-guiding approximation.

Mode designation ($m \geq 1$)	Dispersion equation
$\begin{cases} TE_{0m}\, mode \\ TM_{0m}\, mode \end{cases} (\nu = 0)$	$\frac{1}{u}\frac{J_1(u)}{J_0(u)} = -\frac{1}{w}\frac{K_1(w)}{K_0(w)}$
$EH_{\nu m}\ mode\ (\nu \geq 1)$	$\frac{1}{u}\frac{J_{\nu+1}(u)}{J_\nu(u)} = -\frac{1}{w}\frac{K_{\nu+1}(w)}{K_\nu(w)}$
$HE_{1m}\ mode\ (\nu = 1)$	$\frac{1}{u}\frac{J_0(u)}{J_1(u)} = \frac{1}{w}\frac{K_0(w)}{K_1(w)}$
$HE_{\nu m}\ mode\ (\nu \geq 2)$	$\frac{1}{u}\frac{J_{\nu-1}(u)}{J_{\nu-2}(u)} = -\frac{1}{w}\frac{K_{\nu-1}(w)}{K_{\nu-2}(w)}$

B.2. Linearly Polarized (LP) Modes

If a new parameter is defined in terms of the azimuthal mode number ν:

$$l = \begin{cases} 1, & TE\ and\ TM\ modes \\ \nu + 1, & EH\ mode \\ \nu - 1, & HE\ mode \end{cases} \tag{B.12}$$

the dispersion equations of the LP modes take on the general form (Keiser, 2000; Okamoto, 2006; Yariv and Yeh, 2007; Adams, 1981):

$$\frac{1}{u}\frac{J_l(u)}{J_{l-1}(u)} = -\frac{1}{w}\frac{K_l(w)}{K_{l-1}(w)} \tag{B.13}$$

Table B.2. Compares the relation between LP modes and conventional modes.

LP Modes ($m \geq 1$)	Conventional modes ($m \geq 1$)	Dispersion equation
$LP_{0m}\ mode\ (l = 0)$	$HE_{1m}\ mode$	$\frac{1}{u}\frac{J_0(u)}{J_1(u)} = \frac{1}{w}\frac{K_0(w)}{K_1(w)}$
$LP_{1m}\ mode\ (l = 1)$	$TE_{0m}, TM_{0m}, HE_{2m}\ mode$	$\frac{1}{u}\frac{J_1(u)}{J_0(u)} = -\frac{1}{w}\frac{K_1(w)}{K_0(w)}$
$LP_{lm}\ mode\ (l \geq 2)$	$EH_{(l-1)m}, HE_{(l+1)m}$	$\frac{1}{u}\frac{J_l(u)}{J_{l-1}(u)} = -\frac{1}{w}\frac{K_l(w)}{K_{l-1}(w)}$

For the HE_{1m} mode with $l = 0$ ($\nu = 1$), Bessel function formulas of $J_{-1}(u) = -J_1(u)$ and $K_{-1}(w) = K_1(w)$ should be used in Equation (B.13).

Table B.2 compares the relation between LP modes and conventional modes. As seen in this table, $TE_{0m}, TM_{0m}, HE_{2m}$ modes correspond to $l = 1$, and $\mathrm{EH}_{(l-1)m}, \mathrm{HE}_{(l+1)m}$ modes correspond to values for $l \geq 2$. This means that, all of these modes satisfy approximately the same dispersion equation for the same mode parameters (l and m) and the propagation constants of these mode groups are nearly degenerate. The diagrams below Figure B.1 shows the cross-sectional views of the transverse electric field vectors for the first four lowest-order exact modes, Figure B.2. (a) show how the degenerate LP_{11} modes are produced and the Figure B.2. (b) shows the four degenerate-LP_{11} modes.

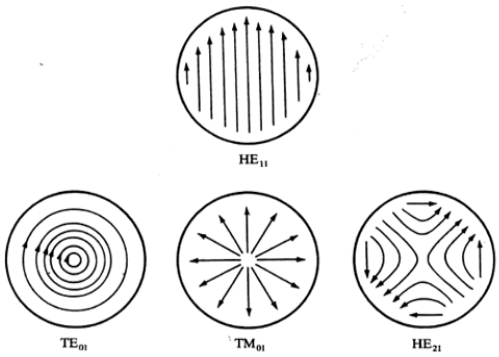

Figure B.1. Cross sectional views of the transverse electric field vectors of the first four lowest-order exact modes (Source: Keiser, 2000).

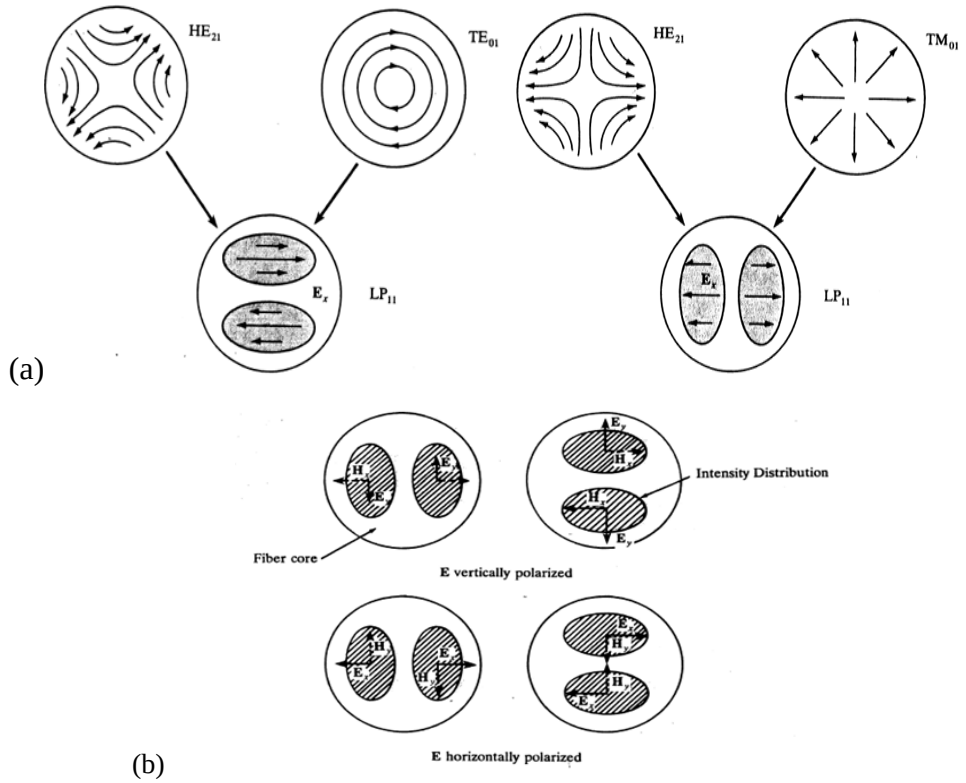

Figure B.2. (a) The degenerate LP_{11} modes, (b) Formation and intensity distributions of LP_{11} modes (Source: Keiser, 2000).

As mentioned before, LP modes are approximate modes (not exact-modes) of step index fibers. The eigenvalues are slightly different in the exact-characteristic equations. LP modes are due to the superposition of TM, TE, HE or EH modes (Okamoto, 2006). Table B.3 shows the comparison of the linearly polarized modes with the exact modes, and shows which linearly polarized modes are obtained from the superposition of which transverse and hybrid modes.

Table B.3. Composition of the lower-order LP modes and their cut-off conditions (Keiser, 2000; Okamoto, 2006).

LP-mode designation	$V_{cut-off}$	**Traditional-mode designation and number of modes**	**Number of degenerate modes**
LP_{01}	*0*	$HE_{11} \times 2$	2
LP_{11}	*2.405*	TE_{01}, TM_{01}, $HE_{21} \times 2$	4
LP_{21}	*3.832*	$EH_{11} \times 2$, $HE_{31} \times 2$	4

(cont. on next page)

Table B.3. (cont.)

LP-mode designation	$V_{cut-off}$	**Traditional-mode designation and number of modes**	**Number of degenerate modes**
LP_{02}	*3.832*	$HE_{12} \times 2$	2
LP_{31}	*5.163*	$EH_{21} \times 2$, $HE_{41} \times 2$	4
LP_{12}	*5.520*	TE_{02}, TM_{02}, $HE_{22} \times 2$	4
LP_{41}	*6.380*	$EH_{31} \times 2$, $HE_{51} \times 2$	4
LP_{22}	*7.016*	$EH_{12} \times 2$, $HE_{32} \times 2$	4
LP_{03}	*7.016*	$HE_{13} \times 2$	2

The total number of modes is same in both theories. The lowest order mode (fundamental mode) which is never cut-off is represented by LP_{01}, and it corresponds to the HE_{11} mode of the exact solutions from the previous section. LP_{01} has two degenerate modes (LP_{x01} and LP_{y01}), and these degenerate modes have same propagation constant (β_{01}) (Yariv and Yeh, 2007).

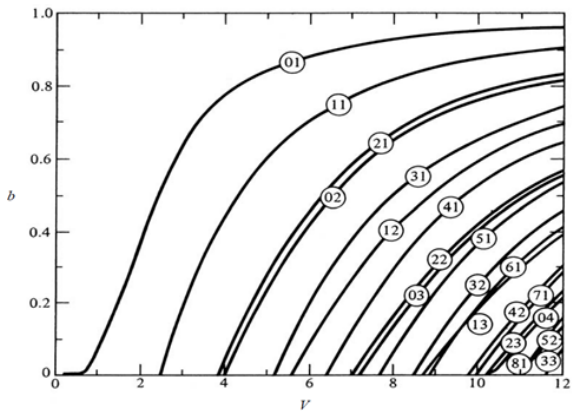

Figure B.3. Normalized propagation constant as function of V for LP_{lm} modes.

Figure B.3 shows the normalized propagation constants of several LP_{lm} modes as a function of the normalized frequency V. For instance; for $V < 2.405$, there is only one mode (LP_{01}) (single mode fiber) and for $V = 6$, there are six modes: LP_{01}, LP_{02}, LP_{11}, LP_{12}, LP_{21} and LP_{31}.